Protein Engineering of Novel Porphyrin/Quinone-Binding Proteins for Light-Induced Electron Transfer

Sam Hay

A thesis submitted for the degree of
Doctor of Philosophy of
The Australian National University

Photobioenergetics,
Research School of Biological Sciences.

February, 2005

This thesis represents research undertaken in the Photobioenergetics Group, Research School of Biological Sciences, The Australian National University, Canberra. This work was completed between February 2001 and August 2004 while I was the recipient of an Australian National University Graduate School Scholarship.

Except where otherwise acknowledged, the work presented in this thesis is my own, and was performed under the supervision of Dr Tom Wydrzynski.

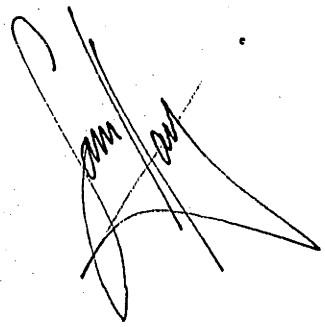

Sam Hay, August 2004

This work has/will be published in the following manuscripts.

Razeghifard, M.R., Hay, S. & Wydrzynski, T. (2001). *De novo* design and synthesis of polypeptides based on photosystem II (S38-011). in *Proceedings 12th International Congress on Photosyntheis*, Critchley, C. & Osmond, C.B. eds., CSIRO Publishing, Melbourne, Australia

Sam Hay, Brett B. Wallace, Trevor A. Smith, Kenneth P. Ghiggino & Tom Wydrzynski (2004) Protein engineering of cyt b_{562} for quinone binding and light-induced electron transfer. *Proc. Natl. Acad. Sci. USA* **101,** 17675–17680

Sam Hay and Tom Wydrzynski (2005) Conversion of the *E. coli* Cytochrome b_{562} to an Archetype Cytochrome *b*: A mutant with *bis*-Histidine Ligation of Heme Iron. *Biochemistry* **44,** 431–439

Hay, S. & Wydrzynski, T. Conversion of Cytochrome b_{562} into a Photoactive Quinone-Binding Protein. in *Proceedings of the 13th International Congress on Photosynthesis*, van der Est, A. & Bruce, D. eds., *in press*

Sam Hay, Brett B. Wallace, Karin A. Ahrling & Tom Wydrzynski, Light-induced electron transfer between a bound zinc-prophyrin and quinone in an engineered cytochrome. *in preparation*

Brett B. Wallace, Sam Hay, Trevor A. Smith, Kenneth P. Ghiggino & Tom Wydrzynski, Engineering of *E. coli* cyt b_{562} for intramolecular electron transfer: Investigation of single-site mutants. *in preparation*

Everything should be made as simple as possible, but not simpler.

Albert Einstein

Contents

Acknowledgements xi

Abstract xiii

List of Tables xv

List of Figures xvii

List of Abbreviations xxi

1 Introduction 1

1.1 Photosynthetic Reaction Centres 2

1.2 Protein Engineering and Protein Design 7

1.3 Protein Electron Transfer 10

1.4 Electron Transfer Theory 16

2 Materials and Methods 27

2.1 Cloning and Mutagenesis of the *E. coli* Cytochrome b_{562} 27

2.2 Cloning and Mutagenesis of a *de novo*-Designed Peptide 32

2.3 Porphyrin Binding and K_d Analysis 33

2.4 Quinone Binding 34

2.5 Experimental 35

3 Porphyrin Binding 41

3.1 Introduction 41

3.2 *Bis*-His vs. His/Met Ligation 49

3.3 Chlorin-Binding 71

3.4 3hlx: A Radical Cytochrome b_{562} Mutant 79

3.5 Summary 83

4 Quinone binding 85

4.1 Quinone Chemistry 85

4.2 A Novel Quinone-Binding Protein 89
4.3 The L30 Mutants 99
4.4 Quinone EPR 106
4.5 Summary 110

5 Electron Transfer **111**
5.1 Singlet Electron Transfer: Mimicking a Reaction Centre 111
5.2 Triplet Electron Transfer: A Long-Lived Charge Separated State 122
5.3 Summary and Future Work 127

6 Conclusions and Future Work **129**

References **133**

Acknowledgements

I would most like to thank Patty. I promise I will not do this again.

I should also thank (or blame) my parents for encouraging me to ask questions. I still don't know a lot of the answers, but I have a lot more questions.

Special thanks to: Brett, for crazy ideas that occasionally worked, dumbing down the the physics, and removing at least 1000 instances of "this" from this thesis; Karin, for help with EPR, Swedish and being always willing to help out; Reza, for convincing me that room-temp EPR might have some use, and general protein chemistry matters; Javier, for help with potentiometry; Fred for happily helping out with anything and everything; Abby for 101 different things, and being very understanding; and everyone else who has helped out in many little ways.

To team PBE in all its mad glory, cheers. In particular, to Garth and the associated Kiwi connection for helping us settle in, and Joel for keeping the wheels on.

Finally, I wish to thank Tom. Thanks for being patient and letting me do my own thing. A lot of people might have panicked under the situation but you showed a lot of poise. Cheers, it's been fun.

Abstract

The primary photosynthetic event in green algae, plants and some photosynthetic bacteria involves a one-electron transfer from a light-activated chlorin (porphyrin) complex to a bound quinone molecule. This thesis describes a protein engineering approach toward mimicking this reaction. Porphyrin and chlorin binding to both synthetic, *de novo*-designed four-helix-bundle peptides, and mutants of the naturally-occuring *E. coli* cyt b_{562} was examined. The role of methionine vs. histidine as the sixth heme axial ligand was studied in both systems by optical spectroscopy, EPR, and redox potentiometry. The binding of 5-coordinate chlorophyll analogues to both synthetic peptides and various cyt b_{562} mutants showed that a minimal binding site for such a porphyrin is a histidine residue at pH $\geq$ 6.0. The importance of a defined binding pocket on binding energies and solvent sequestration is demonstrated with the cytochrome mutants. Several attempts to create a protein-bound excitonically-coupled porphyrin dimer are also discussed.

A novel quinone-binding protein was then developed which is capable of undergoing light-induced electron transfer. Cytochrome b_{562} was modified to covalently bind a benzoquinone and to our knowledge is the first report of a designed quinone-binding protein. The unique quinone-binding site was created by placing a cysteine within the hydrophobic interior of the cytochrome. Various quinones, such as *para*-benzoquinone and coenzyme Q_0, were shown to covalently attach to the protein through a cysteine sulphur addition reaction to the quinone ring. The protein can simultaneously bind a porphyrin or chlorin and the cysteine placement was designed to place the bound quinone about 10 Å from the edge of the bound porphyrin. Fluorescence measurements confirmed that the bound hydroquinone is incorporated toward the protein's hydrophobic interior and is partially solvent-shielded. The bound quinones remain redox-active and the semiquinone can be generated by a 1-electron reduction at high pH. By using different quinones this midpoint can be tuned by ~500 mV. Several protein mutants were made which modulate the redox properties of the bound quinone through specific interactions with the protein. When the heme binding site of the quinone-bound cytochrome is reconstituted with zinc-porphyrin or zinc-chlorin,

light-induced electron transfer from the porphyrin/chlorin to the bound quinone (but not hydroquinone) is observed. The electron transfer reaction was characterised by transient EPR and fast optical techniques. Triplet electron transfer predominates in the zinc-protoporphyrin/protein/quinone system with a rate of $\sim 1.7 \times 10^3\ s^{-1}$. Conversely, electron transfer in the chlorin/protein/quinone complexes occurs from a singlet state with the rate in the order of $10^8\ s^{-1}$. We consider the chlorin system a simple and functional model of a quinone-type reaction centre.

List of Tables

1.1 Effect of the intervening medium on k_{ET}. 22

3.1 Binding energies of porphyrin ligation by imidazole 46
3.2 Absorbance and redox properties of heme-bound peptides 50
3.3 Heme binding constants 53
3.4 Thermal denaturation parameters 56
3.5 EPR g tensors of hemin-reconstituted H23M42 and related peptides . . 61
3.6 Porphyrin and chlorin binding to monomeric *de novo* peptides 73
3.7 Energetics of dimerisation of the *de novo* peptides 76
3.8 Protein-bound Zn-Ce_6 absorbance 79

4.1 Physical properties of wildtype, H63N and I17C cytochrome b_{562}. . . . 91
4.2 Protein-bound hydroquinone fluorescence 93
4.3 Guanidine denaturaton of ferri-I17C and ferri-I17C-*p*BQ 97
4.4 Redox properties of the quinones 100
4.5 Selected properties of the L30 proteins. 104

5.1 Electron transfer properties of some Zn-Ce_6-I17C-quinone and Zn-Ce_6-L30-quinone complexes 116
5.2 Reported oxidation potentials of Zn-substituted hemoproteins 123
5.3 Electron transfer in ZnPP-I17C-quinone complexes 127

List of Figures

1.1 Electron transport schemes of the four different reaction centres 2

1.2 The structures of photosystems I and II 3

1.3 The reaction centre from purple bacteria 4

1.4 The Q_A binding site in photosystem II and the bacterial reaction centre . 7

1.5 A helical wheel representation of an amphipathic α-helix 8

1.6 Histidine-ruthenium complexes 11

1.7 A simplified zinc porphyrin/heme triplet electron transfer reaction scheme 13

1.8 A porphyrin-quinone diad 15

1.9 A Jablonski diagram illustrating the different energy levels and types of transitions that can occur in a porphyrin system 17

1.10 A theoretical Marcus curve 24

2.1 SDS PAGE of cytochrome b_{562} purification 32

3.1 The various porphyrins used in this work 43

3.2 Binding isotherms of imidazole ligation to some porphyrins 46

3.3 Molecular models of the proteins used in this work 46

3.4 The cytochrome b_{562} variants used in this work 47

3.5 Molecular model of the M7H mutant of cytochrome b_{562} 51

3.6 Absorbance spectra of oxidised and reduced H63N and M7H 52

3.7 K_d determination in M7H 54

3.8 Circular dichroism spectra of M7H 55

3.9 Denaturation of M7H 57

3.10 EPR spectra of ferri-M7H and ferri-H63N 60

3.11 Redox titration curves for *bis*-imidazole heme, and M7H and H63N . . 63

3.12 Difference absorbance spectra of the $[H23M42]_2$-Fe(III)-heme charge-transfer band 67

3.13 Redox titration curves of $[H23H42\text{-heme}]_2$ and $[H23M42\text{-heme}]_2$ . . . 68

3.14 Fluorescence excitation, emission and polarisation spectra of H23H42 . 70

3.15 Binding of Zn-Ce_6 to *de novo* peptides measured by tryptophan quenching 71
3.16 Concentration-dependent change in polarisation of H23M42 75
3.17 Absorbance spectra of Zn-Ce_6 in solution, ligated with imidazole and bound to cytochrome b_{562} 78
3.18 Molecular modelling of dimerised porphyrin-bound His3hlx 80
3.19 Absorbance spectra of the crude supernatant of His3hlx over/expressing *E. coli* cells 81
3.20 SDS-PAGE and size exclusion chromatography of His3hlx 82
3.21 Reconstitution of His3hlx with ZnPP 83

4.1 The structures of some common biological quinones 86
4.2 The reaction scheme of CoQ_0 with cysteine 89
4.3 Molecular model of quinone-bound cytochrome b_{562} 90
4.4 Absorbance spectra of CoQ_0 and I17C-bound (reduced) CoQ_0 92
4.5 Fluorescence spectra of reduced I17C-bound *p*BQ 94
4.6 Guanidine denaturation of I17C 96
4.7 Redox titration curves of I17C-bound CoQ_0 and CoQ_0 in solution . . . 99
4.8 Molecular models of the L30-quinone complexes 101
4.9 Guanidine denaturation of the L30 ferri-proteins 102
4.10 Stern-Volmer plot of potassium iodide quenching of protein-bound hydroquinone fluorescence 103
4.11 Redox titration curves of the L30-CoQ_0 complexes 104
4.12 Absorbance spectra of neutral and anionic semiquinone radicals 106
4.13 Generation of the *p*BQ semiquinone by raising the pH 107
4.14 Room temperature EPR spectra of I17C-bound semi-*p*BQ 108
4.15 Room temperature EPR of I17C-bound CoQ_0 109

5.1 Absorbance and fluorescence spectra of Zn-Ce_6-I17C-CoQ_0 112
5.2 Room temperature light-minus-dark EPR spectra of Zn-Ce_6-I17C -CoQ_0 113
5.3 Zn-Ce_6fluorescence decay curves 115
5.4 Energy levels of light-induced ET in Zn-Ce_6-I17C-quinone 117

5.5 Fluorescence decay curves of Zn-Ce_6-L30-CoQ_0 118
5.6 The relationship between k_{ET} and E(Q/Q^{2-}) in Zn-Ce_6-protein-quinone complexes 120
5.7 Electronic coupling in the Zn-Ce_6-I17C-quinone complexes 121
5.8 Absorbance, fluorescence and phosphorescence spectra of I17C-bound ZnPP 123
5.9 Energy levels of light-induced triplet-ET in ZnPP-I17C-quinone complexes 124
5.10 Room temperature X-band EPR spectra of ZnPP-I17C-*p*BQ 125
5.11 Time-resolved EPR of ZnPP-I17C-*p*BQ 126

List of Abbreviations and Physical Constants

A, acceptor

Abs, absorbance

(B)Chl, (bacterio)chlorophyll

(B)Pheo, (bacterio)pheophytin

BRC, bacterial reaction centre

CD, circular dichroism

CoQ_0, coenzyme Q_0 (2,3-dimethoxy-5-methyl-1,4-benzoquinone)

CT, charge transfer

CS, charge separation

Cys, cysteine

cyt, cytochrome

D, donor

DCBQ, dichlorobenzoquinone

DMBQ, dimethylbenzoquinone

$E_{0,0}$, lowest singlet excited state energy

E, potential

E_F, redox potential of the folded protein

E_m, midpoint potential

EPR, electron paramagnetic resonance

eqn, equation

ET, electron transfer

E_T, lowest triplet excited state energy

EtOH, ethanol

E_U, redox potential of the unfolded (denatured) protein

F/flr, fluorescence

$g_{x/y/z}$, x/y/z g tensor

GS(H), glutathionine (reduced)

h, Planck's constanst (6.626×10^{-34} J s)

H_{AB} , electronic coupling (eqn 1.14)

heme, iron(II or III)-protoporhyrin IX

His, histidine

HS, high spin

Ile, isoleucine

Im, imidazole

Gly, glycine

k_{ET}, rate of electron transfer

k_B, Boltzman constant (1.38066 x 10^{-23} J K^{-1}, 8.617385 x 10^{-5} eV K^{-1})

K_d, dissociation constant (eqn 2.1)

k_f, rate of fluorescence

k_{IC}, rate of internal conversion

k_{ISC}, rate of intersystem crossing

k_P, rate of phosphorescence

LHC, light harvesting complex

LS, low spin

m, cooperativity of the unfolding transition (eqn 2.2)

MEK, methyl ethyl ketone

Met, methionine

mutant, in this work describes a protein of differing amino acid sequence to the originally cloned (wt) sequence

n, stoichiometry, or the number of electrons transferred in a Nernst reaction

nd, not determined

*p*BQ, *para*-benzoquinone

P, generic light-activated molecule, or the primary donor of the BRC

PCR, polymerase chain reaction

P_i, phosphate buffer

PS I/II, photosystem I/II

P_{680} , the primary donor of PS II

P_{700} , the primary donor of PS I

Q, quinone

R, distance (usually in Å) or the ideal gas constant (8.3145 K mol J^{-1})

SDS PAGE, sodium dodecyl sulfate polyacrylamide gel electrophoresis

SHE, standard hydrogen electrode

T, temperature

T_M, melting temperature (eqn 2.3)

TREPR, time-resolved EPR

Tyr, tyrosine

ubiQ, ubiquinone

wt, wildtype (here referring to both a bacterial strain or a peptide or protein, similarly to the term mutant)

Zn-Ce_6, zinc-chlorin e_6

ZnP, zinc-porphyrin

ZnPP, zinc-protoporphyrin IX

β , exponential coupling coefficient (eqn 1.17)

ΔC_P , partial heat capacity change upon unfolding (eqn 2.3)

ΔE_f, difference in redox potential between the folded and unfolded protein

ΔG, free energy

$\Delta\Delta G$, change or difference in free energy

ΔG_d, free energy of dimer dissociation (eqn 3.9)

ΔG^{H_2O}, free energy of unfolding in the absence of denaturant (eqn 2.2)

ΔH_{vH}, van't Hoff enthalpy change (eqn 2.3)

ε, absorption coefficient (units of $M^{-1}cm^{-1}$)

ε_0 , permittivity of free space (8.854×10^{-12} $C^2J^{-1}m^{-1}$)

λ, Marcus reorganisation energy (eqn 1.15), or wavelength

τ, lifetime

Φ, efficiency

CHAPTER 1

Introduction

All of the energy needs of plants and photoautotrophic bacteria are met by the light reactions of photosynthesis. The primary photochemistry involves the absorption of visible photons and the subsequent conversion of the absorbed energy into chemical potential energy by the formation of a charge-separated state. This photochemistry takes place in membrane-bound protein complexes called reaction centres (RCs). The best understood of these systems are the bacterial reaction centres (BRCs) from purple non-sulfur bacteria. The primary photochemistry that occurs in the BRC is also common to the RC in photosystem II (PS II) of cyanobacteria and higher plants (reviewed in (Allen & Williams, 1998; Diner & Rappaport, 2002; Okamura *et al.*, 2000)). The photochemical reactions in the RCs occur through the transfer of an electron from a light-excited (bacterio)chlorophyll ((B)Chl) through the protein, via a (bacterio)pheophytin ((B)Pheo), to a bound quinone molecule. The cofactors are $\sim$10 Å apart so that the electron transfer (ET) reaction is non-adiabatic, occurring through a quantum tunnelling mechanism (DeVault *et al.*, 1967; Marcus & Sutin, 1985). Synthetic chemists have designed and built small organic models to mimic these ET reactions. These models typically consist of a covalently-linked, light-activated electron donor, and an electron acceptor. This approach has been incredibly successful at mimicking both vectorial ET[1] and a long-lived charge separated state, the hallmarks of biological ET (Ho *et al.*, 1980; Kurreck & Huber, 1995; Gust *et al.*, 1993, 2001).

The recently-developed techniques of protein engineering and *de novo* protein design now allow a constructive approach to study ET reactions in proteins, as proof-of-principle and also to experimentally verify theory. The aim of the present work was to mimic aspects of the primary photochemistry of photosynthetic reaction centres using simple modified proteins. This work takes the concept of the organic diad a step closer to the natural systems by binding the porphyrin donor and quinone acceptor within a small well-defined peptide allowing a new method of studying ET reactions. It takes inspiration and methodologies from a fairly broad and sometimes disparate body of research. This chapter attempts to review the pertinent literature.

[1]Vectorial ET is described in Section 1.4

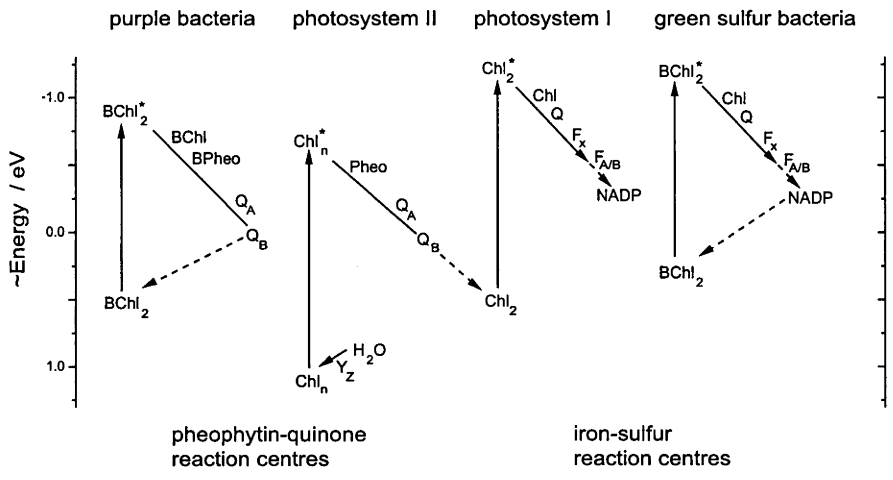

Figure 1.1: Electron transport schemes of the four different reaction centres. Adapted from Allen & Williams (1998)

1.1 Photosynthetic Reaction Centres

The photosynthetic RCs are conserved in all photosynthetic organisms, and are of two types (Figure 1.1). One type of RC is shared by the purple bacteria and is similar to PS II of cyanobacteria and higher plants. These are known as pheophytin/quinone-type RCs. The other type of RC is known as an iron-sulfur-type RC. This type of RC is found in the green sulfur bacteria and is similar to photosystem I (PS I) of cyanobacteria and higher plants.

Recently an atomic resolution (2.5 Å) structure of the cyanobacterial PS I has emerged (Jordan *et al.*, 2001) and this is shown in Figure 1.2. This complex is probably the largest membrane protein to have yet been crystallised. It is a trimer, with each monomer comprising 12 proteins, 96 Chl molecules, iron and calcium ions and over 200 water molecules. The structure of the RC from green sulfur bacteria has not been determined but homology modelling with PS I has been completed by Heathcote *et al.* (2003) and shows considerable homology.

The work in this thesis is concerned with mimicking the pheophytin-quinone-type RC. There are many X-ray crystal structures of RCs from purple bacteria and recently from PS II from cyanobacteria. The structure and function of these RCs is discussed below.

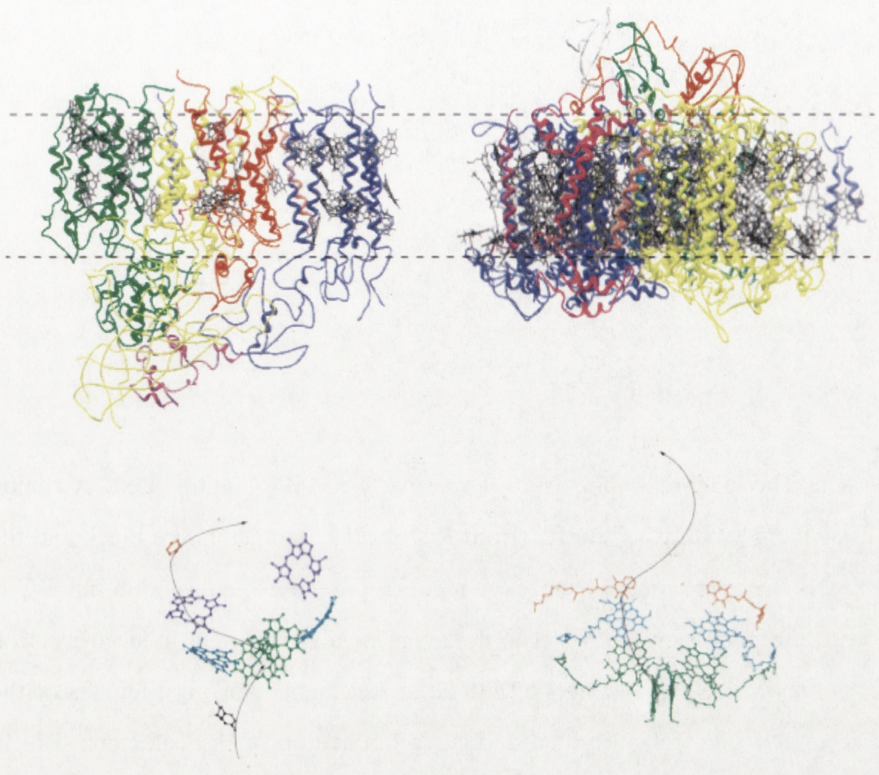

Figure 1.2: The structures of PS I (right) and II (left) (1JBO.pdb and 1IZL.pdb, respectively). Photosystem II is not scaled relative to PS I, but the dotted lines represent the approximate region of lipid membrane. The respective inner cofactors involved in electron transport with arrows showing the electron transfer pathway are shown below.

The Bacterial Reaction Centre

The first X-ray crystal structure of an integral membrane protein was the that of the RC from *Rhodopseudomonas viridis* (Deisenhofer *et al.*, 1985). This was quickly followed by the structure of the *Rhodobacter sphaeroides* RC (Allen *et al.*, 1986). Both *Rp. viridis* and *R. sphaeroides* are purple, non-sulfur photosynthetic bacteria, and represent the pheophytin-quinone-type RC.

There is little inter-species difference between the major structural elements of the RC which consists of two membrane-spanning proteins (denoted L and M) with five transmembrane α-helices each, and a largely cytoplasmic protein (denoted H) with a single transmembrane α-helix (reviewed in Allen *et al.* (1986); Parson (1996); Allen

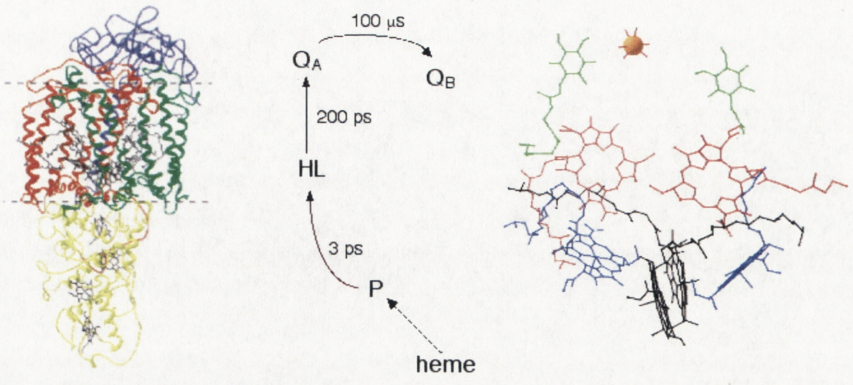

Figure 1.3: The reaction centre from purple bacteria (4PRC.pdb). Left, A ribbon diagram of the 4 proteins of the RC from *Rp. viridis*. Cofactors are black and the dotted line is the approximate membrane region. Contrary to convention this RC is drawn with the periplasm below. The cofactors involved in light-induced electron transfer are shown centre and right. Midldle, a schematic showing lifetimes of the charge separated states and Right, the relative orientation of the cofactors: Black, special pair (P); Blue, BChl; Red, BPheo; Green, ubiquinone; Orange, non-heme iron. See the text for details.

& Williams (1998)). The structure of the *Rp. viridis* RC is shown in Figure 1.3. The L and M proteins have an approximate two-fold symmetry. The function of the H subunit is not well understood and it's removal from purified BRC preparations does not affect their activity. In *Chloroflexus aurantiacus* the H subunit is missing. One significant difference does exist between *Rp. viridis* and *R. sphaeroides* however. The former contains an additional (fourth) protein, a soluble tetra-heme *c*-type cyt (cyt) located on the periplasmic side of the membrane. This is an interesting protein in its own right as it acts as a molecular wire (see e.g. Chen *et al.* (2000)). Electron transfer is thought to occur sequentially through the four heme molecules which are oriented roughly linearly.

Common to the the BRCs is a suite of cofactors non-covalently bound to the L and M subunits in a pseudo-symmetrical manner. The route of ET through these cofactors is asymmetric and is shown in Figure 1.3. These cofactors are 4 BChls, 2 bacteriopheophyrins (BPheo), 2 quinones, where the type is species-dependent, a non-heme

iron and a carotenoid. The primary donor (P) is a dimer of excitonically-coupled BChls which are situated near the periplasm at the interface between the L and M proteins with one-each BChl bound to a conserved histidine on L and M. Upon excitation an electron is rapidly (within ~3 ps) transfered to one of the BPheo molecules (denoted HL) located about midway across the membrane. This electron is probably transfered via a BChl situated between P and HL but observation of this discrete intermediate is only tentative. From HL, the electron is transfered in 200 ps to a quinone (Q_A) situated near the cytoplasm. A second quinone (Q_B) is then reduced by $Q_A^{-\cdot}$ in 100 μs. This is summarised in Figure 1.1 and Figure 1.3 and reviewed by Parson (1996). Subsequently, $P^{+\cdot}$ is re-reduced by ET from a heme in either the cyt subunit in *Rp. viridis* or from soluble cyt c_2 in *R. sphaeroides*.

The relative ease of the purification of these RCs and their stability coupled with protocols for the site-directed mutagenesis in *R. sphaeroides* has allowed a lot of structure-function information to accumulate (reviewed in Moser *et al.* (1995); Allen & Williams (1995); Parson (1996); Okamura *et al.* (2000)). Because of this level of detail, the bacterial RC has been called "the hydrogen atom of electron transfer". This is discussed further with regard to the ET reactions later in Section 1.3.

Photosystem II

Photosystem II is the large membrane pigment/protein complex responsible for splitting water into molecular oxygen during oxygenic photosynthesis. The structure of cyanobacterial PS II has been recently reported (Zouni *et al.*, 2001; Kamiya & Shen, 2003; Ferreira *et al.*, 2004) and is shown in Figure 1.2. Unfortunately none of the structures have achieved atomic resolution and the best to date is about 3.5 Å (Ferreira *et al.*, 2004).

At the heart of PS II is P_{680}, a photo-reactive cluster of up to six Chl molecules[2]. Among this cluster is a central pair of weakly excitonically-coupled Chl *a* molecules which are ligated to adjacent histidines on the D1 and D2 proteins of the PS II reaction centre. Upon illumination, P_{680} becomes excited and transfers an electron to a quinone

[2]the exact nature of P_{680} is still uncertain and could consist of 1-6 individual Chls

cofactor (Q_A) via a bound pheophytin molecule. Subsequently an electron from the water-oxidising site is transferred via a redox-active tyrosine residue (Y_Z) to fill the electron hole left on the oxidised P_{680}, $P_{680}^{+\cdot}$ (reviewed in (Ort & Yocum, 1996)). Interestingly, $P_{680}/P_{680}^{+\cdot}$ is the strongest oxidant in biology with an oxidation potential of >+1.1 V (Rappaport *et al.*, 2002). This oxidation potential is much higher than that of P^+ in the BCR (+0.5 V, (Lin *et al.*, 1994)) and in solution, Chl *a* has a considerably lower redox potential ($\sim$ 0.8 V, reviewed in Scheer (1991)) which is insufficient to split water. It is therefore the interaction of the protein environment within PS II on the bound Chls that sufficiently increases the redox potential of P_{680} and allows water oxidation to occur.

A General Model of a Reaction Centre

The acceptor side of PS II and the BRC function very similarly, and the cofactors and route of ET are conserved. The nature of the primary donor is a little different, but both have a central dimer of (B)Chl. The donor side of the BRC is a heme while in PS II it is a manganese complex. In both the BRC and PS II the primary quinone binding site (Q_A) is remarkably similar (see Figure 1.4) despite the fact that chemically different quinones are bound (menaquinone or ubiquinone in the BRC, plastoquinone in PS II).

Conceptually, a minimalistic model of a pheophytin-quinone reaction centre would comprise a (B)Chl dimer, a pheophytin, 2 quinones linked via a non-heme iron, and an un-specified electron donor. The cofactor separation would all be about 10 Å, and the cofactors would be bound to a membrane-spanning complex. This complex would be capable of vectorial ET upon illumination. Some of these features are explored in this thesis. Work toward creating a peptide capable of binding a (B)Chl dimer is described in Chapter 3. In Chapter 4 the introduction of a novel quinone binding site is described. The bound quinone is shown to act as an electron acceptor in ET reactions (Chapter 5). These proteins were created by modifying existing proteins (protein engineering) or utilising synthetic (*de novo*-designed) peptides.

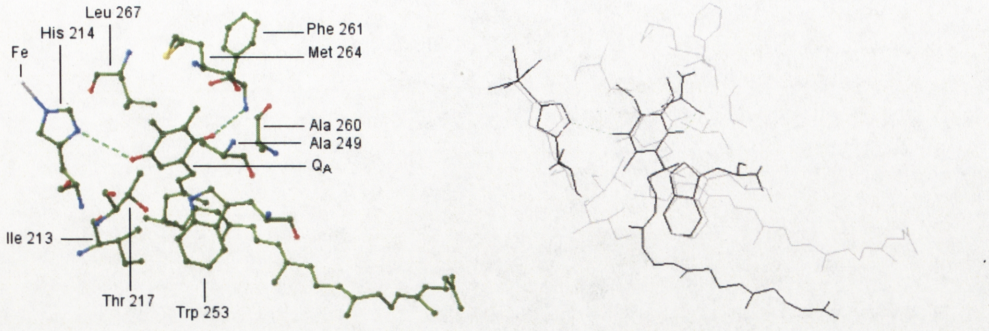

Figure 1.4: Left, The Q_A binding site in PS II taken from the structure of Ferreira *et al.* (2004) (1S5L.pdb). Only the residues surrounding the quinone head group are shown. These are are all located on the D2 protein and are labelled for reference. Fe is a non-heme iron and broken green lines are putative hydrogen bonds. Right, A comparison of the Q_A binding site in PS II (grey) and the *R. sphaeroides* RC (1AIJ.pdb, black). The structures are aligned by the homologous histidine and tryptophan residues and only selected residues from the bacterial site are shown.

1.2 Protein Engineering and Protein Design

Protein engineering can be thought of as the modification or creation of a protein with novel or enhanced functions. There are essentially two approaches to protein engineering, directed evolution and rational design.

Directed evolution takes a Darwinist approach to the problem. Typically a gene of interest is randomly mutated and the mutants are then expressed and screened, often *in vivo*, for a desired property. Any likely candidates are isolated and subjected to further rounds of mutagenesis and selection until a protein with the desired property is found (reviewed in Arnold & Volkov (1999); Saven (2002)). One early success of directed evolution was the modification of an enzyme to carry out the hydrolysis of a para-nitrobenzyl ester of an antibiotic in organic solvents (Moore & Arnold, 1996). More recently from the same group, a protein with an unnatural H_2O_2-dependent hydroxylation reaction was obtained from an initial library of ~200 000 random mutants. This required a novel screening method involving the co-expression of another enzyme and

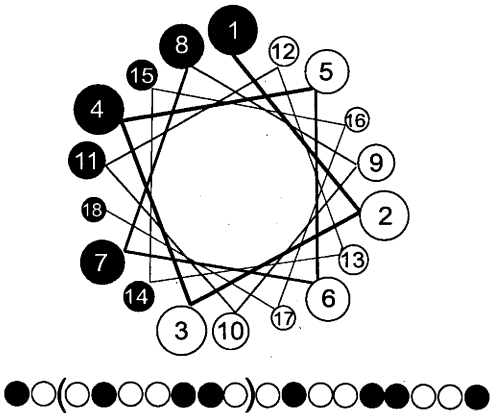

Figure 1.5: A helical wheel representation of an amphipathic α-helix showing the patterning of polar (white) and non-polar (black) residues. Underneath is a schematic showing the sequence of this pattern and a heptad repeat in parenthesis.

highlights perhaps the biggest problem with directed evolution, the screening method. The method will only work if the desired properties of the engineered protein can be readily screened, for instance by ligand binding, catalysis or with the aid of phage display (reviewed in (Hoess, 2001). On the other hand, directed evolution offers the advantage of not requiring precise structural and mechanistic information on the protein being modified. It also allows the sampling of a relatively large amount of sequence space (10^6-10^{12} sequences).

The work in this thesis takes another approach - protein design. Protein design is a more guided and rational approach based on rules gleaned from the principles of protein folding. This may involve the modification of an existing protein or the creation of a totally new one. Examples of the former include: (*i*) the conversion of a cyt from a *b*-type to *c*-type (Barker *et al.*, 1993); (*ii*) the introduction of a redox-active tyrosine into the BRC (Kalman *et al.*, 1999); (*iii*) the addition of disulfide bridges to stabilise lysozyme (Ueda *et al.*, 2000); (*iv*) the incorporation of non-natural amino acids (by solid-phase peptide synthesis) that predictably alter properties of protein-bound cofactors (Low *et al.*, 2001; Privett *et al.*, 2002); (*v*) covalent linkage of the peptides to non-natural "templates" (Rau *et al.*, 1999); and (*vi*) covalently modifying the protein with e.g. ruthenium, or replacing existing cofactors (see Section 1.3).

The design of novel proteins, known as *de novo* design, pushes the limits of our understanding of the protein structure/function relationship. Early *de novo*-design efforts, largely by DeGrado and coworkers, concentrated on self-aggregating amphipathic α-helices (reviewed in Hill *et al.* (2000); Baltzer *et al.* (2001)). Basically, an alpha helix has 3.6 residues per turn, thus a 7-residue (heptad) sequence will cover two full turns. By patterning hydrophobic and hydrophilic residues within a heptad repeat, the folded helix will have all the hydrophobic residues on one side (Figure 1.5). This allows dimerisation (driven by hydrophobic sequestration) of these peptides in to e.g. three or four-helix bundles. Cofactors can then be bound within the hydrophobic interior of these peptide aggregates and this has been an active area of research. Dutton and coworkers designed heme-binding peptides (Robertson *et al.* (1994), reviewed in Gibney & Dutton (2001); Lombardi *et al.* (2001), described in Chapter 3), while Degrado and coworkers have bound other metal centres (reviewed in DeGrado *et al.* (1999)). In similar work Gibney *et al.* (1996) introduced an iron-sulfur cluster into a loop region linking two α-helicies in a *de novo*-designed peptide. More recently, a novel protein fold was designed and experimentally validated by Kuhlman *et al.* (2003), and two reports of catalytically-active *de novo*-designed enzymes have appeared (Dwyer *et al.*, 2004; Kaplan & DeGrado, 2004).

Unfortunately the rational design process, both in terms of protein modification and *de novo*-design, is a relatively slow process and generally requires an iterative approach. Each design must be biophysically characterised before the next change is implemented (see e.g. Gibney *et al.* (1999). This is not as bad as it seems as usefull data are generated at each step, and there are many things which can be screened that would be impossible by a directed evolution approach. Using a combination of the rational and directed evolution approaches, Hecht and coworkers have developed a combinatorial technique where the pattern of polar and non-polar residues is fixed while the identity of the residues is not (Kamtekar *et al.*, 1993). From these libraries, stable native-like proteins have been identified, some of which can bind heme (Rojas *et al.* (1997), reviewed in Hecht *et al.* (2004)). In related work, *de novo*-designed peptides have been screened by phage display (reviewed in Hoess (2001); Saven (2002)). Both of these methods allow the possibility of expediting the design process.

Cytochrome b_{562}

Much of this thesis involves the engineering of the *E. coli* cyt b_{562}, a small, soluble four-helix-bundle protein with a single *b*-type heme cofactor originally described by Itagaki & Hagar (1966). This protein is found in the periplasm of *E. coli* and, while its postulated role is in electron transfer, no physiological partners nor biological function have been assigned. Cytochrome b_{562} is enigmatic as it is the only soluble cyt without a covalently attached heme and one of only two known *b*-type cyts with methionine/histidine (Met/His) heme iron ligation (the other protein being the fungal extracellular flavocyt cellobiose dehydrogenase (rCDH) (Rotsaert *et al.*, 2003)). Cytochrome b_{562} has been well characterised both structurally (Hamada *et al.*, 1995; Arnesano *et al.*, 1999) and biophysically (see for example Moore *et al.* (1985); Barker *et al.* (1996); Robinson *et al.* (1997); Springs *et al.* (2002)). This makes cyt b_{562} a good candidate for the study of protein-porphyrin binding interactions.

Upon binding to a protein, heme forms axial ligands with one or two protein side chains. The amino acid side chains of histidine, methionine, lysine, asparagine, tyrosine, proline and cysteine are able to act as such ligands forming nitrogen-, sulfur- or oxygen-iron bonds. The amino terminus has also been shown to act as a ligand. This bonding has a major role in regulating the properties of the ligated heme as well as potentially playing a significant role in the stabilisation of the heme-protein complex. In the cyts *bis*-histidine (*bis*-His) and Met/His ligation are much more common than the other forms of ligation where *bis*-His ligation predominates in the *b*-type cyt and Met/His ligation is generally found in the *c*-type cyts. The *E. coli* cyt b_{562} has atypical Met/His ligation. However, I have created a mutant with *bis*-His heme ligations, which is described in Chapter 3.

1.3 Protein Electron Transfer

There have been several approaches to study light-induced protein ET reactions. These involve using: (*i*) ruthenium-, or more recently rhenium-, modified proteins; (*ii*) modification of proteins with flavin; (*iii*) metal-substituted (i.e. Zn) hemoproteins such as cyt *c* and hemoglobin; (*iv*) mutants of the photosynthetic reaction centres, principally

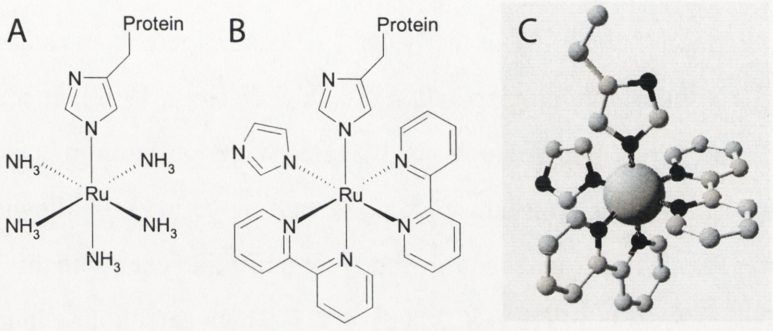

Figure 1.6: Histidine-ruthenium complexes. A, Rua_5His, and B, $Ru(bpy)_2(Im)(His)$. A molecular model of $Ru(bpy)_2(Im)(His)$ is shown in C. See text for details.

the BRC; and (v) using small organic molecules consisting of one or more covalently linked donor and acceptor groups. These will each be described in turn.

Rhuthenium Modification

The method of using ruthenium (Ru)-modified proteins to study ET was pionerred by Harry Gray and coworkers in the early 1980's (Winkler *et al.* (1982); Nocera *et al.* (1984), reviewed in Winkler & Gray (1992); Bjerrum *et al.* (1995)). Cytochrome *c* was modified by coordination of pentaaamineruthenium (Rua_5, Figure1.6) to hisitidine 33 on the surface of the protein (Yocom *et al.*, 1982). Photoinduced ET from Ru^{2+} to Fe(III) was observed with a slow k_{ET} of 30 s^{-1}. The driving force[3] (ΔG^0) of the Ru-modified Fe(III)-cyt *c* reaction was only -0.18 eV, explaining in part the slow k_{ET}. Several approaches were taken to increase ΔG^0, including substituting Fe for Zn in the cyt (Meade *et al.*, 1989), and using alternate ligands to the Ru (other than amine) such as bipyridine (bpy) (Chang *et al.*, 1991). The structures of the Rua5 and $Ru(bpy)_2$(imidazole) complexes are shown in Figure 1.6. The use of bpy ligands was quite successful and $-\Delta G^0$ values $>$ 1 eV have been achieved (reviewed by Winkler & Gray (1992); Bjerrum

[3]The driving force, ΔG^0, is described in Section 1.4.

et al. (1995)). Additionally, by replacing the amine ligands with bpy, the reorganisation energy associated with solvent rearangement around the Ru complex was reduced by about half (Winkler & Gray, 1992). Ru can also be bound to lysine residues via an amide linkage (Durham *et al.*, 1989). There is a problem with this method however, as due to the conformational flexibility in the lysine side chain, there is an estimated 4-8 Å uncertainty in the donor/acceptor separation (Winkler & Gray, 1992). In a series of experiments Rua_5-modified myoglobin was substituted with 6 different metals and the ET reactions characterised. This produced a significant range in ΔG^0 allowing quite accurate estimates for the electronic coupling and reorganisation energy in this system[4] (reviewed in Winkler & Gray (1992). In other work, ET between photo-generated Ru and heme in *de novo*-designed peptides has been reported by Rau *et al.* (1999) and Cristian *et al.* (2003).

More recently, proteins modified with rhenium(I) (Re) have been used in ET experiments (Di Bilio *et al.* (2001), reviewed in Miller *et al.* (2004)). Re-modified azurin exhibits light-induced ET from the Cu^+, via a tyrosine, to Re^{2+}. The Re^{2+}, generated by light-induced ET to a sacrificial electron acceptor[5] in solution, is sufficiently oxidising ($\sim$ +2 V) to generate a tyrosine radical. Thus, the use of Re-modified proteins now allows the study of very-high driving force ET reactions.

Flavin Modification

In a similar methodology to Ru-modification, flavin molecules have been used to study protein ET. Upon excitation, flavin can form a semiquinone species by abstracting an electron from a donor, such as EDTA, in solution. The semiquinone is capable of reducing Fe(III)-heme through an ET reaction (Ahmad *et al.*, 1981). Flavin derivatives can be covalently bound to a cysteine on the surface of a protein through a disulphide bond, and this was demonstated in cyt *c* by Twitchett *et al.* (1997). The authors showed ET between the bound flavin and heme and determined a reorganisation energy of 1.2 eV. Sharp (1998) covalently bound a flavin with the interior of a *de novo*-designed heme-binding maquette and also showed ET from the photogenerated semiquione to

[4]Electronic coupling, H_{AB}, and reorganisation energy, λ, are defined in Section 1.4.

[5]A sacrificial electron acceptor becomes irreversibly reduced

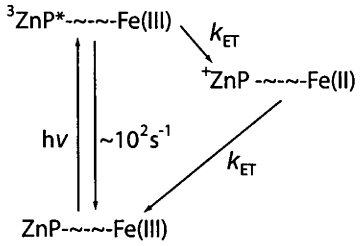

Figure 1.7: A simplified zinc porphyrin/heme triplet electron transfer reaction scheme.

heme.

Metal Substitution

Unlike (B)Chl, zinc porphyrin (ZnP) readily forms a triplet state upon excitation with near-unity efficiency (Sudha *et al.*, 1984). This triplet state (^{3}ZnP*) is long-lived ($\sim$ 14 ms) (Zemel & Hoffman, 1981; Sudha *et al.*, 1984) and is a strong reductant, forming the ZnP cation upon ET. As the triplet lifetime is long, relatively slow ET reactions, such as those between proteins, can be studied with this technique. The ET reaction from ZnP to heme is shown in Figure 1.7.

Independently, Hoffman (McGourty *et al.*, 1983; Peterson-Kennedy *et al.*, 1984; McGourty *et al.*, 1987) and McLendon (Simolo *et al.*, 1984; McLendon *et al.*, 1985) used an electronically excited ZnP or a free-base porphyrin (H_2P) (Cheung *et al.*, 1986) as an electron donor in long-range protein ET. Both groups made use of existing hemoproteins and substituted heme for ZnP. Hoffman and coworkers showed ET over about 20 Å in a Fe/Zn hemoglobin hybrid with k_{ET} of $\sim$ 100 s^{-1} (McGourty *et al.*, 1983, 1987). Electron transfer from ^{3}Zn*-cyt *c* peroxidase to yeast and horse-heart cyt *c* (Fe(III)) was also measured (Ho *et al.*, 1985). Triplet energy transfer was also demonstrated from zinc-substituted proteins (Zemel & Hoffman, 1981).

Meanwhile, McLendon and coworkers measured the rate of inter-protein ET in several protein-protein complexes such as between Zn-hemoglobin and Fe(III)-cyt b_5 (Simolo *et al.*, 1984) and Zn-cyt *c* and cyt b_5 (McLendon *et al.*, 1985), which has also been characterised by Qin & Kostic (1994). These ET reactions were quite slow 10^3

- 10^5 s^{-1} despite donor/acceptor distances of around 8-10 Å. Interprotein ET between Fe(II)-cyt *c* peroxidase and Fe(III)-cyt *c* was measured at about this time by Cheung *et al.* (1986) by a rapid-mixing technique and allowed the measurement of the physiological ET reaction. This suggested that the reorganisation energy associated with these intraprotein ET reactions was about 1 eV. Those data are collated and briefly reviewed in Mayo *et al.* (1986). In other work, Magner & McLendon (1989) measured the oxidation potential Zn-cyt to be about +0.8 V and showed that metal-substitution increased the cyt *c* redox potential by 0.64 V. More recently ET has been reported in other metal-substituted proteins such as ZnP-substituted nitrite reductase (Bellelli *et al.*, 1996) and cyt P450cam (Furukawa *et al.*, 2000).

Electron Transfer in Photosynthetic Reaction Centres

A series of PS I RC mutants has been created with altered P_{700} Chl ligands (Krabben *et al.*, 2000). These mutations increase the oxidation potential of P_{700} by up to 140 mV. In the BRC, site-directed mutagensis around the BChl (Lin *et al.*, 1994; Mattioli *et al.*, 1995; Huppman *et al.*, 2002) and quinone (Takahashi *et al.*, 2001), and extraction and replacement of the quinones with alternate acceptors (Gunner *et al.*, 1986; Warncke & Dutton, 1993; Warncke *et al.*, 1994) have led to an extensive understanding of the ET reactions. The distance dependence on k_{ET} in 8 ET reactions within the BRC has been analysed by Moser & Dutton (1992) allowing the calculation of a general value for the electronic coupling. This is described further in Section 1.4. The effect of the driving force on ET has been thoroughly established and the various reorganisation energies characterised (reviewed in e.g. Moser *et al.* (1995); Parson (1996)).

In a series of experiments, Allen, Williams and coworkers have demonstrated the utility of tuning specific protein-BChl interactions. In the *Rhodobacter sphaeroide* RC, the oxidation potential of the special pair was tuned by the introduction of up to four hydrogen bonds with the BChl special pair. The introduction of four H-bonds was able to increase the oxidation potential of P in a stepwise fashion by 355 mV (Lin *et al.* (1994); Mattioli *et al.* (1995), reviewed in Allen & Williams (1995)). By introducing ionizable residues around the BChl special pair the P/P^+ oxidation potential was also increased (Johnson & Parson, 2002). Remarkably, the oxidation potential of the

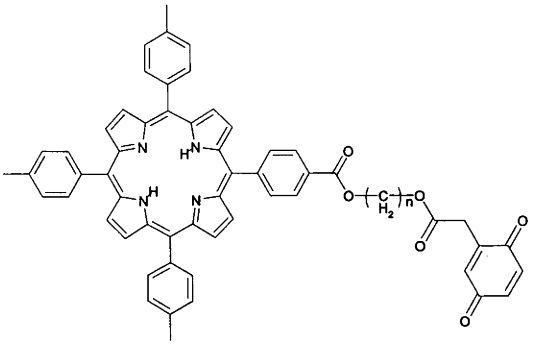

Figure 1.8: A porphyrin-quinone diad described in (Ho *et al.*, 1980)

quadruple H-bond mutant is sufficient to oxidise an introduced tyrosine (Kalman *et al.*, 1999) and to oxidase exogenous manganese (Kalman *et al.*, 2003).

Donor-Acceptor Molecules

Organic molecules comprising a covalently linked electron donor and acceptor have been used for many years in the study of photo-induced charge separation. Some notable early work, taking inspiration from the photosynthetic reaction centre, used molecules consisting of an amide-linked free-base porphyrin and benzoquinone (Figure 1.8). These molecules showed quinone-induced quenching of the porphyrin fluorescence and porphyrin cation radical generation upon excitation (Ho *et al.*, 1980), consistent with the formation of a charge separated state. Many different designs of donor-acceptor molecules have been described and these have been reviewed by Wasielewski (1992); Kurreck & Huber (1995); Gust *et al.* (1993, 2001). These include molecules where the quinone acceptors have been replaced with fullerene (C_{60}) (Gust *et al.*, 2001) and more complex molecules such as pentads (Gust *et al.*, 1993).

One demonstration of these molecules was described by Steinberg-Yfrach *et al.* (1998) (reviewed by Gust *et al.* (1993)). The authors created a "triad" molecule consisting of a carotenoid, porphyrin and quinone. Upon excitation the porphyrin donates an electron to the quinone and the hole left on the porphyrin is filled from the carotenoid π system. This gives the molecule a charge separated state with a lifetime sufficiently long-lived to allow ET from the semiquinone to another quinone in solution. This reaction was proton-coupled and when the triad was oriented in an artificial membrane

with the quinone acceptor, light-induced proton pumping was observed. This generated a proton motive force sufficient to generate ATP with an ATP synthase complex.

These donor-acceptor molecules offer several advantages over protein systems when studying ET reactions. A covalently-linked donor and acceptor are more strongly electronically coupled than if they are (non-covalently) protein-bound. However, the measured k_{ET} values are typically non-physiological as a result (discussed further in Section 1.4). The molecular structure of these model compounds can be accurately determined by molecular modelling as can the electronic structure. This allows very precise interpretation of the measured properties of these systems and a very rational approach to design specific properties. As more protein structures are solved and computing power is increased this will likely become more of a reality in the protein ET field.

1.4 Electron Transfer Theory

Upon absorption of a sufficiently energetic photon, a light-activated molecule (P), such as (B)Chl or ZnP, is transformed to an electronically excited state (P*). This species is generally a highly-energetic and thus unstable species, which is relatively short lived. P* is deactivated by either radiative or non-radiative transitions back to the ground state and these mechanisms are shown in Figure 1.9. Each of these decay processes is characterised by a unimolecular rate constant (k_i) and each excited state characterised by a lifetime (τ) which is described by:

$$\tau = \frac{1}{\sum k_i}. \tag{1.1}$$

In some circumstances, the excited state lifetimes are sufficiently long-lived to allow a bimolecular reaction with another (generally ground state) molecular (Q). Commonly this process is either energy transfer or electron transfer (ET), and in the case of a reaction with Q, the excited state lifetime of P is shortened:

$$\tau_Q = \frac{1}{\sum k_i + k_{ET}}\ , \tag{1.2}$$

where k_{ET} describes the rate of energy transfer or ET. This is immensely helpful to the experimentalist as it allows a method of measuring ET reactions. Essentially, the

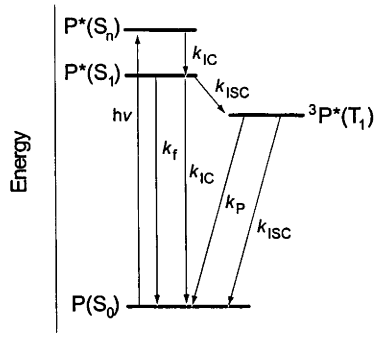

Figure 1.9: A Jablonski diagram illustrating the different energy levels and types of transitions that can occur in e.g. a porphyrin system. S_0 is the singlet ground state while S_n and S_1 are any and the lowest excited singlet states and T_1 is the lowest excited triplet state. The transitions are fluorescence (k_f) and phosphorescence (k_P), which are radiative, and internal conversion (k_{IC}) and intersystem crossing (k_{ISC}), which are non-radiative.

lifetime of P* is measured, typically by fluorescence decay, both in the presence (τ_Q) and absence (τ_0) of an acceptor. k_{ET} is then obtained by:

$$k_{ET} = \tau_Q^{-1} - \tau_0^{-1}. \tag{1.3}$$

Eqn 1.3 is used in Chapter 5. These values can be used to calculate the efficiency (Φ) of the reaction:

$$\Phi = 1 - \frac{\tau_Q}{\tau_0}. \tag{1.4}$$

It follows that, for practical reasons, an energy or ET reaction is only observed when the excited state has a lifetime longer than about 1 ns. This is typically the case for (B)Chls and explains the advantages of using ZnP, which has a 14 ms triplet lifetime.

We shall now briefly look at the differences between energy transfer and ET. Both mechanisms are important in biology. The solar energy collected in the light harvesting complexes, which surround the photosynthetic RCs, is transfered to the reaction centre in a series of energy transfer reactions, but once in the RC this energy drives ET reactions. Photosynthetic energy transfer has been reviewed by (Gobets & van Grondelle, 2001; Cogdell *et al.*, 2003), while biological ET has been the focus of many excellent reviews (Marcus & Sutin, 1985; Winkler & Gray, 1992; Winkler *et al.*, 1999; Moser

et al., 1995; Larsson, 1998) and books such as (Bolton & Mataga, 1991; Bendall, 1996). In the case of an energy transfer reaction, P* deactivates by transfer of energy to a suitable quencher. This returns P to the the ground state, while inturn exciting Q. This reaction is described by:

$$P^* + Q \rightarrow P + Q^*. \tag{1.5}$$

Q* then returns to the ground state either by an additional energy transfer reaction or by other deactivation. Due to conservation, energy transfer is a down-hill process and can generally be described by either Dexter or Förster excitation transfer[6].

Deactivation of P* through ET occurs a little differently than by energy transfer reactions. P* is returned to the ground state via a radical state (such as $P^{+\cdot}$). An example of this is:

$$P^* + Q \rightarrow P^{+\cdot} + Q^{-\cdot}, \quad k_{ET}, \tag{1.9}$$

$$P^{+\cdot} + Q^{-\cdot} \rightarrow P + Q, \quad k_{CR}. \tag{1.10}$$

[6]Dexter excitation transfer, which is also known as electron exchange excitation transfer, occurs by an electron exchange mechanism and requires an overlap of the orbitals between P* and Q. Thus, this mechanism requires that P and Q be both spatially close and strongly-coupled. The rate is described by:

$$k \propto [h/(2\pi)]P^2 J \exp[-2r/L] \tag{1.6}$$

where L and P are constants, r is the distance between the donor and acceptor and J is the spectral overlap integral. J describes the degree of overlap between the fluorescence emission spectrum of P and the absorbance spectrum of Q. J is calculated by:

$$J = \frac{\int F(\lambda)\epsilon(\lambda)\lambda^4 d\lambda}{\int F(\lambda) d\lambda}, \tag{1.7}$$

where $F(\lambda)$ is the fluorescence intensity of D and $\epsilon(\lambda)$ is the absorption coefficient of D, both at a given wavelength, λ in units of cm^{-1}.

Förster excitation transfer, which is also known as dipole-dipole excitation transfer, is a long-range tranfer mechanism involving an interaction between the transition dipole moments of P and Q. The rate is described by:

$$k = \frac{\kappa^2 J 8.8x10^{23} mol}{n^4 \tau_0 r^6} \tag{1.8}$$

where κ is an orientation factor, n the refractive index of the medium, τ_0, r and J are as described previously. Fluorescence resonance energy transfer (FRET) is a phenomenon described by a Förster mechanism and this is used in the following chapters.

Eqn 1.10 is a consequence of the instability of the charge separated state and k_{CR} describes the rate of the charge recombination reaction which is also known as the back-reaction.

In the ET reactions discussed in this work, P and Q are termed electron donors and acceptors, respectively. A good example of this is when eqn 1.9 describes the light-induced ET event in the primary photochemsity of a photosynthetic RC where P is (B)Chl and Q is a (B)Pheo. In photosynthesis however, eqn 1.10 is non-productive and in a functional RC the charges are not allowed to recombine. Preventing charge recombination is not trivial as the charge separated state is energetically unstable due to Coulombic attraction between the cation and anion radicals. Additionally the radicals can be very unstable and may deactivate through chemical reactions with the solvent, protein or oxygen. These issues aside, in order to prevent charge recombination, either the charges must be further separated or the charges otherwise neutralised. Coulomb's law states that the attraction will decrease exponentially with distance[7] and while the best method of stabilising the charge separated state is to physically move P and Q further apart it is generally not feasible when they are protein-bound. Another option is to allow the charges to move further apart through additional ET reactions with other redox active components (cofactors). This is often termed linear ET and occurs in a functional RC by:

$$P^{+\cdot}Q^{-\cdot} + A \rightleftharpoons P^{+\cdot}Q + A^{-\cdot}, \qquad k_{ET_2}, \tag{1.12}$$

$$P^{+\cdot}Q + D \rightleftharpoons PQ + D^{+\cdot}, \qquad k_{ET_3}, \tag{1.13}$$

where D and A are an additional electron donor and acceptor, respectively. In the case of the BRC, A is the primary quinone, Q_A and D a heme. This mechansim too returns P to the ground state but also converts the absorbed energy of the photon into a fairly stable chemical potential. In order for the reactions in eqn's 1.12 and 1.13 to occur $k_{ET_2} > k_{CR}$ and $k_{ET_3} > k_{-ET_2}$. More generally, the ET reactions must be

[7]Coulomb's law states:

$$F = \frac{q_1 q_2}{4\pi\varepsilon_0 R^2} \tag{1.11}$$

where q_1 and q_2 are the net charges of the two molecules, R is the separation of the molecules and ε_0 is the permittivity of space (8.854 x 10^{-12} $C^2J^{-1}m^{-1}$).

optimised to occur at a maximal rate yet have a minimal rate of charge recombination (e.g. $k_{ET_2} \gg k_{-ET_2}$ and $k_{ET} \gg k_{CR}$).

Long-range ET is a quantum mechanical phenomenon where the donated electron is either located on D or A, instantaneously tunnelling from one to the other. In this case k_{ET} is relatively insensitive to changes in temperature, which allowed DeVault & Chance (1966) to identify tunnelling as a likely ET mechanism in proteins. k_{ET} can be calculated according to Fermi's golden rule:

$$k_{ET} = \frac{2\pi}{\hbar} H_{AB}^2 FC, \tag{1.14}$$

where H_{AB} is the electronic coupling between the donor (D) and acceptor (A). The FC term describes the Franck-Condon weighted density of states, which was interpreted by Marcus (1956) (reviewed in Marcus & Sutin (1985)) in terms of simple harmonic oscillators[8]. This allows the calculation of k_{ET} by:

$$k_{ET} = \sqrt{\frac{4\pi^3}{h^2 \lambda k_B T}} H_{AB}^2 \exp\left(-\frac{\Delta G^{\neq}}{k_B T}\right), \tag{1.15}$$

where h is Planks constant, k_B is the Boltzmann constant, λ is the reorganisation energy and $\Delta G^{\neq}$ is the activation energy which is related to the reaction driving force (ΔG^0) by:

$$\Delta G^{\neq} = \frac{(\Delta G^0 + \lambda)^2}{4\lambda}. \tag{1.16}$$

The three terms, H_{AB}, λ and ΔG^0 will be described in turn. The ability to modulate k_{ET} in a protein by altering each of these properties will be specifically discussed below.

Electronic Coupling

The electronic coupling matrix elements, H_{AB}, describes the overlap of the wave functions of the donor and acceptor. In a protein this can be described most simply[9] in terms of an electron tunelling (quantum mechanically) from one narrow potential well through a uniform insulating barrier of height V to another well of equal depth (Hopfield, 1974). In this case the coupling has an exponential distance (R) dependence

[8]It should be mentioned that some of the assumptions made in Marcus theory do not describe very-fast (fs) ET reactions very well.

[9]Unfortunately however, often the most simple quantum mechanical explanations are not very simple.

described by:

$$H_{AB}^2 \propto \exp(-2R\sqrt{2mV}/\hbar) = \exp(-\beta R) \tag{1.17}$$

where m is the mass of the electron and β is an exponential coefficient (Gamow, 1928). The maximal rate of ET (when -$\Delta G^0 = \lambda$) is approximately related to β by:

$$k_{ET} \sim 10^{13}\exp[-\beta(R - R_0)], \tag{1.18}$$

where R is the edge-to-edge separation of D and A, and R_0 is about 3.6 Å[10]. Some typical β values are given in Table 1.4. Moser & Dutton (1992) showed that the eight characterised ET reactions in the BRC have a k_{ET} vs. R dependence with β = 1.4, the same β value found in organic solvents. This led the authors to suggest an empirical description of protein ET, known as Dutton's ruler:

$$\log k_{ET} = 15 - 0.6R - 3.1(\Delta G + \lambda)^2/\lambda, \tag{1.19}$$

which seems to be accurate to about an order of magnitude. In the molecular diads discussed later in Section 1.8, D and A are covalently attached. β and therefore the electronic coupling is typically much stronger in these diads than in the proteins they are mimicking. Thus, when trying to mimic the photochemistry within an RC, there is good reason to place a protein between D and A. This would be typically achieved by binding these cofactors to the protein.

In the superexchange model (McConnell, 1961), which has been identified as the major mechanism for long-range ET in proteins (Onuchic *et al.*, 1992), molecular orbitals on the intervening protein residues act as virtual intermediates which together constitute the ET pathway. D and A are coupled via these virtual intermediates. An approximate value of the superexchange coupling matrix element can be obtained using perturbation theory:

$$H_{AB} = \sum_{ij} V_{ai} G_{ij} V_{jd} \tag{1.20}$$

where V_{ai} and V_{jd} are the couplings of the donor and acceptor electronic states to the bridge states, i, j, and G_{ij} is the electronic Green's function of the bridge (Cheung *et al.*,

[10] R_0 is twice the average van der Waals radius of the constituents of D and A (typically a value for carbon is used (~ 1.8 Å))

Table 1.1: Effect of the intervening medium on k_{ET}.

Medium	β ($Å^{-1}$)	V (eV)	k_{ET} at 10 Å (s^{-1})
Through-space			
vacuum	2.8	7.5	10^5
solvent	1.4	1.9	10^9
protein	1.4	1.9	10^9
Through-bond			
covalent	0.7	0.5	10^{11}
conjugated	0	0	10^{13}

The β values are from Moser & Dutton (1992), V is the barrier height, calculated from eqn 1.17 by the method of Larsson (1998), and k_{ET} was calculated from eqn 1.18.

1999). It is not trivial to calculate eqn 1.20 in large systems such as protein, as the electronic structure of the protein is required. In cyt b_{562}, a relative small single-heme protein of 106 amino acids (described in Section 1.2 and Chapter 3), there are more than 1700 atoms. The electronic structure of cyt b_{562} can be calculated using the extended Hückel method. More accurate calculations using semi-empirical or *ab-initio* methods are currently computationally very expensive on proteins of this size. Obviously for larger proteins this is even more of a problem. Beratan *et al.* (1987) (reviewed in Beratan & Onuchic (1996)) have developed another method to estimate H_{AB} based on a β-weighted average of all the possible through-bond and through-space paths the electron can take during the tunnelling reaction. The Beratan method is called the pathways model and its attraction is that is not particularly computationally difficult. This method is used in Chapter 5. Due to the exponential distance dependence on k_{ET}, typically ET in a protein occurs in a roughly straight line from D to A. Therefore it is generally only those residues directly between D and A that must be directly considered as bridge states. It should then be possible to modulate the electronic coupling, and thus k_{ET}, by alteration of these amino acid residues. There is some experimental evidence that this is possible (Huppman *et al.*, 2002) but the authors could not distinguish the

contribution from altered coupling and that from changes in ΔG^0.

Reorganisation Energy

The reorganisation energy, λ, was first described by Marcus (reviewed in Marcus & Sutin (1985)). λ is defined as the energy required to distort the equilibrium geometry of the reactant (D and A) and environment (protein and immediate solvent) to an equilibrium geometry of the product and its environment, without allowing the transfer of the electron. The charge distribution can be quite different in the charge-separated state which must be accommodated through alteration of the local dielectric through structural rearrangements. This can be fairly far-reaching and when one or both D and A are solvent-exposed then λ can get large ($>$ 1 eV). As solvent-reorganisation can have such a major influence on λ, when both D and A are well buried withing a protein away from the solvent then λ can be small ($<$ 0.4 eV). The contribution from bond deformation with the donor and acceptor molecules can also have a significant effect on λ. If D and A have i and j many bonds, respectively, which undergo rearrangement upon ET, their effect on λ can be estimated from:

$$\lambda = \tfrac{1}{2} \sum (k_{D_i} \Delta r_{D_i}^2 + k_{A_j} \Delta r_{A_j}^2) \tag{1.21}$$

where k is the force constant of the bonds within A or B, and Δr it the change in these bond lengths. The consequence of eqn 1.21 has a considerable effect on porphyrin/protein electron transfer reactions. For cyts, the oxidation state changes occur in the central iron atoms of bound heme molecules. The four Fe-N bonds show a significant change in bond length (Δr), in the order of 0.1 Å each. This results in a relatively large λ value for Fe(II)$\leftrightarrow$Fe(III) redox reactions. The converse of this is the case with regard to Chl. The excited state of Chl* is shared over the many bonds within the conjugation pathway of the porphyrin. The bond deformation (Δr) is very small and thus λ is small. To determine the contribution the environment reorganisation has on λ in a protein, the electrostatic potential of the protein must be calculated. This is possible by continuum electrostatics calculations based on the solution the Poisson-Boltzmann equation (see e.g. Sharp (1998)), described briefly in Chapter 5.

Tuning an ET reaction by rationally manipulating λ is a daunting task. One ad-

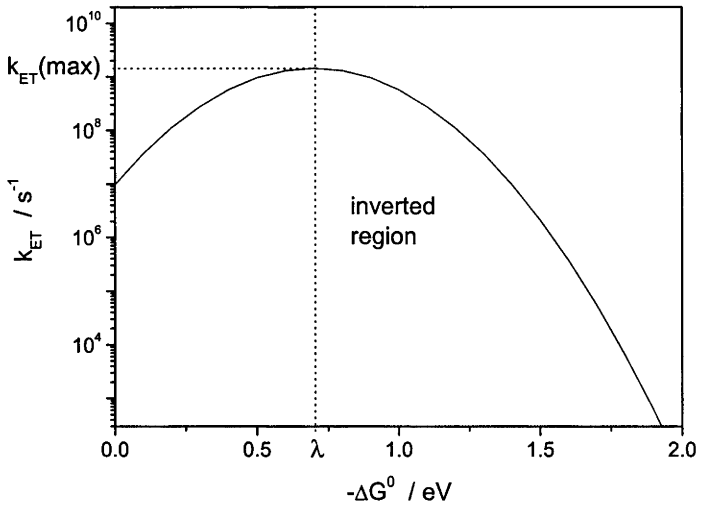

Figure 1.10: A theoretical Marcus curve (Dutton's ruler (Moser & Dutton, 1996), eqn 1.19) where $\lambda = 0.7$ eV and the cofactor separation = 10 Å.

vantage of using a special pair of (B)Chl in an RC is that the electron hole on P^+ is shared over two (B)Chl molecules. Thus, according to eqn 1.21 the reorganisation energy associated with P/P^+ would be expected to be smaller than that associated with $(B)Chl/(B)Chl^+$. From a protein engineering perspective, it is possible to alter the proteins local dielectric by introducing e.g. charged residues. It may also be possible to alter the solvent-exposure of the donor and/or acceptor and thus the solvent reorganisation energy. These methods will all potentially also alter ΔG^0 and H_{AB} and thus manipulation of k_{ET} by tuning λ is not the method of choice.

Driving Force

Aside from changing the cofactor distance, altering the driving force is probably the most tangible method of tuning ET reactions in a protein. It should be noted that eqn 1.16 describes a Gaussian and as $-\Delta G^0$ is increased, k_{ET} becomes maximal then slows when $-\Delta G^0 > \lambda$. This is a rather counter-intuitive effect that has been experimentally well-documented (Marcus & Sutin, 1985). The region where $-\Delta G^0 > \lambda$ is called the inverted region. The inverted region is shown in Figure 1.10.

The value of ΔG^0 for light-induced ET can be calculated by a method developed by Rehm & Weller (1970):

$$\Delta G^0_{ET}(eV) = \Delta E - E_{0,0} - e^2/4\pi\varepsilon_0\varepsilon_S R \tag{1.22}$$

$$\Delta E = E^0(D^{+\cdot}/D) - E^0(A/A^{-\cdot}) \tag{1.23}$$

where $E^0(D^{+\cdot}/D)$ and $E^0(A/A^{-\cdot})$ are the experimentally determined standard electrode potential of the donor and acceptor radicals, respectively, vs. the same reference electrode (e.g. the standard hydrogen electrode, SHE), e is the elementary charge, ε_0 is the permittivity of free space, ε_S is the static dielectric constant, R is the centre-to-centre distance between the ions and $E_{0,0}$[11] is the energy of the lowest excited state of the donor (zero, zero transient energy). The Coulombic term ($e^2/4\pi\varepsilon_0\varepsilon R$) arises due to the Coulombic attraction betwen the donor and acceptor in the charge separated state ($D^{+\cdot}$ and $A^{-\cdot}$). In water ($\varepsilon_S \sim 80$) this term approaches 0 and is often ignored. This approach may not be valid for the case of protein-bound cofactors where the dielectric of the protein in places may be as low as ~ 4 (discussed in Johnson & Parson (2002)). However, due to charge screening within the protein the effective charges may also be reduced and this Coulombic term becomes rather uncertain. On the other hand, $E_{0,0}$ can be experimentally determined from the average donor absorbance (Q_Y for a porphyrin) and fluorescence maxima (Marcus & Sutin, 1985; Sutin, 1982). The penalty the RC primary donor pays in having a lower energy than the other (B)Chl is that it also has a $E_{0,0}$ value.

By varying the spectral properties of the donor ($E_{0,0}$), the midpoint potential of either the donor or acceptor (ΔE), or the dielectric of the protein we can modulate ΔG^0 and thus k_{ET}. In practical terms, if the protein local dielectric is altered around either D or A there will be a change in ΔE also. Likewise, by perturbing the spectral properties of D, and thus $E_{0,0}$, it is likely one will also change ΔE. As both $E_{0,0}$ and ΔE can be measured, it is possible to determine the relative contributions.

In a light-induced ET reaction, the subsequent charge recombination has a driving force:

$$-\Delta G^0_{CR} = E_{0,0} + \Delta G^0_{ET}. \tag{1.24}$$

[11] For ground state ET such as for $Q_A^- \rightarrow Q_B$ in PS II and the BRC, $E_{0,0} = 0$

Thus the activation energy ($\Delta G^{\neq}$) which governs the maximal rate of ET is quite different in the forward and back reactions:

$$\Delta G^{\neq}(\text{forward}) = (\Delta G^{0}_{ET} + \lambda)^2/\lambda \tag{1.25}$$

$$\begin{aligned} \Delta G^{\neq}(\text{back}) &= (\Delta G^{0}_{CR} + \lambda)^2/\lambda & (1.26) \\ &= (-(E_{0,0} + \Delta G^{0}_{ET}) + \lambda)^2/\lambda. & (1.27) \end{aligned}$$

Often this $-E_{0,0}$ shift is sufficient to push the back-reaction well into the Marcus inverted-region and thus $k_{ET} \gg k_{CR}$ which allows productive linear ET, such as in eqn 1.12 and 1.13, to occur.

To summarise, long-range protein ET reactions occur by a tunnelling mechanism described by Marcus theory (Marcus & Sutin, 1985). The rate of ET is dependent on the distance between the donor and acceptor, and the intervening medium. If the donor and acceptor are at a fixed distance and orientation, k_{ET} is dependent on the electronic coupling, the driving force, and the reorganisation energy, and to some extent the temperature. The most tangible method of modulating the rate of ET in a protein is probably to alter the cofactor distance or the driving force. The latter approach is used in Chapter 5.

CHAPTER 2

Materials and Methods

2.1 Cloning and Mutagenesis of the *E. coli* Cytochrome b_{562}

Cloning

Genomic DNA was extracted from an overnight culture of *E. coli* BL21 DE3 (Novagen). A CTAB/phenol/chloroform protocol[1] was used to purify genomic DNA. No further steps were required.

The sequence of the gene encoding the *E. coli* strain B-type cyt b_{562} (gene *cybC*) was retrieved from the NCBI sequence data bank. Primers were designed to amplify the gene without the N-terminal periplasmic signalling sequence. The primers had the following sequence:

Forward: GGTATTGAGG GTCGCATGGC TGATCTTGAA GACAATATGGAAACC

Reverse: AGAGGAGAGT TAGAGCCTCA TTAACGATAC TTCTGGTGATAGGCG

They both include a sequence for Ligation Independent Cloning (LIC) into the Novagen vector pET-30 Xa/LIC. The reverse primer adds a second stop codon to ensure the correct termination of ribosomal translation of the recombinant protein. Standard PCR methods were employed but considerable optimisation of the reaction was required. The PCR reaction was supplemented with $MgSO_4$ to a final concentration of 4 mM. The reaction required the addition of 2 units of *pwo*TURBO DNA Polymerase (Stratagene) and the forward primer after a hot start to prevent the formation of primer dimers. Any annealing temperature between 48°C and 58°C was sufficient for amplification of product. In addition to the desired product, despite reaction optimisation, considerable non-specific product was also produced, predominantly at smaller lengths than the desired gene. The amplified gene was gel-purified using a QIAprep kit (QIAGEN).

The gel-purified gene was ligated into pET-30 Xa/LIC (Novagen) using Novagen standard protocols for the LIC system. The ligated plasmid was transformed into NovaBlue (Novagen) using a standard heat-shock protocol (42°C, 30 s). The plasmid was purified from an overnight liquid culture of the transformants with a QIAquick spin

[1]Miniprep of bacterial genomic DNA in Current Protocols in Molecular Biology Online 2002, John Wiley and Sons, Inc.

miniprep kit (QIAGEN). The plasmid was then transformed into BL21 DE3 pLysS (Novagen) for subsequent expression, again using a standard heat-shock protocol. Transformants were screened for expression of a protein of correct size. Likely candidates were DNA sequenced (see below) to confirm their identity. It was necessary to transform the ligated plasmid into NovaBlue first as this strain has better plasmid maintenance and is more competent than BL21.

To confirm the sequence of the cloned *cybC* gene and the subsequent site-directed mutants described below, DNA sequencing was performed. The pET vectors are derived from the pBR322 plasmid which contains the ColE1 origin of replication from pMB1. This origin of replication is tightly controlled, resulting in approximately 25 copies of the plasmid per bacterial cell. This is considered a low copy number plasmid. In order to purify enough plasmid DNA for sequencing a 10 mL liquid culture was grown overnight (typically about 14-16 h) from a glycerol stock obtained from a single colony. The entire 10 mL culture was used in the miniprep. The plasmid was purified using a QIAquick spin miniprep kit (QIAGEN). The procedure was scaled up accordingly to account for the larger culture volume. Membranes from a QIAprep gel extraction kit (QIAGEN) were used in preference to those from the miniprep kit. This typically yielded enough plasmid for sequencing which was performed by the Biomolecular Resource Facility, JCSMR, ANU.

Site-Directed Mutagenesis of *cybC*

Oligonucleotide-mediated site-directed mutagenesis of the *cybC* gene was performed to construct mutants of the recombinant cyt b_{562}. Initially the H63N mutant was created using the following primers:

Forward: GATTTCCGCA ACGGTTTCGA C

Reverse: GTCGAAACCG TTGCGGAAAT C

which were used in concert with the original full-length *cybC* primers, in a 3 step PCR process ((1) Forward + LIC Reverse, (2) Reverse + LIC Forward, (3) product of (1) and (2) as template + LIC Forward and LIC Reverse) ((1) and (2) used the *cybC* pET-30 vector as template). PCR conditions were standard [2] and PCR products were

[2]PCR conditions typically consisted of 30 cycles of 95°C, 60 s/55°C, 60 s/72°C, 60 s

gel-purified. The product of step (3) was treated similarly to the amplified *cybC* gene and ligated into pET-30 Xa/LIC and transformed into NovaBlue then BL21. After an expression screen candidates were sequenced to confirm they had the mutant sequence.

The M7H and I17C mutants were created from the H63N gene (c.f. wild type) and are thus double mutants. These mutants were constructed by the same methods as H63N. PCR protocols were standard and all PCR products were again gel-purified. The primers were as follows:

M7H Forward: CTTGAAGACA ATCATGAAAC CCTCAAC

M7H Reverse: GTTGAGGGTT TCATGATTGT CTTCAAGATC AGCC

I17C Forward: CAATTTAAAA GTGTGCGAAA AAGCGG

I17C Reverse: CCGCTTTTTC GCACACTTTT AAATTGTCGT TGAGGG

As the original LIC primers are prone to primer dimer formation, shorter LIC primers were used. They have the following sequence:

LIC forward: GGTATTGAGG GTCGCATGG

LIC reverse: AGAGGAGAGT TAGAGCCTC

The L30Y and L30H mutants were created from the I17C gene, again by standard methods. The primers are as follows:

L30Y Forward: CGTATACGAAGATGCGCGCCGCAGCC

L30Y Reverse: GCGCGGCATCTTCGTATACGCGTCTTTGACTTGCGCCGC

L30H Forward: CGCACACGAAGATGCGCGCCGCAGCC

L30H Reverse: GCGCACTTCGTGTGCGCGTCTTTGACTTGCGCCGC

3hlx Mutants

The H63N and M7H genes were further mutated to yield a semi-synthetic 3-helix-bundle cyt. The *cybC* gene was amplified from the H63N or M7H pET-30 vectors using the LIC primers. This product was gel-purified and cut with Pst I endonuclease (Roche). The longer 5' fragment was gel purified and amplified with the LIC forward primer and the following 57 nt. primer,

3hlx: AGAGGAGAGT TAGAGCCTCA TTAGCAGCCA CCGCCACCTT CATTTGCCAG CTTCAGC

The PCR product was gel-purified and ligated into pET-30 Xa/LIC and then treated as for H63N and the other mutants of cyt b_{562}.

The 3hlx primer encodes an LIC-compatable sequence and an additional stop codon. The LIC reverse primer is compatible with 3hlx-amplified sequence. The Pst I-cleavage was necessary to remove the 3' end of the gene which has a LIC reverse sequence. The 3hlx primer encodes the sequence Gly Gly Gly Cys preceding the stop codon. The codons encoding this sequence were chosen based on *E. coli* codon bias and then randomised. The 3hlx primer is designed such that these four residues are cloned in frame after Gly 82, which is located in the loop linking helices 3 and 4. Thus the mutation removes helix 4 and replaces it with a flexible poly-glycine loop with a C-terminal cysteine which is designed to form a disulfide bond.

Expression and Purification

Expression

Typically 4 L liquid cultures of cyt-expressing BL21 were grown from which recombinant cyt b_{562} was purified. The media used was generally 2xYT[3] which was autoclaved for 2 successive 30 min periods to fully sterilise the 4 L volume. This was inoculated with a 200 mL overnight culture of BL21 containing the pET-30 Xa/LIC vector encoding cyt b_{562} (or cyt mutant). This culture was inoculated from a glycerol stock of a single clone of transformed BL21. All cultures were grown in the presence of kanamycin A (30 μg.mL^{-1}, Sigma) and chloramphenicol (33 μg.mL^{-1}, Sigma). The culture was aerated with a marine aerator via a filter and large marine pump and grown in a 37°C incubator. Once the culture reached mid-log phase as measured by an OD_{600nm} of $\sim$ 0.5, it was induced with (1 mM final concentration) IPTG (isopropyl thiogalactoside, Sigma). The culture was grown for about 6 h after induction at which point the cells were harvested by centrifugation (5,000 *g* for 10 min in a GS-3 rotor[4] at room temperature). The cells were resuspended in a minimal volume of 50 mM tris (tris(hydroxymethyl)aminomethane), pH 8.0 and frozen at -20°C. Typically the cells were a pink/red colour with a UV/Vis. spectrum attributable to cyt b_{562}.

[3] 2xYT media consists of 16 g tryptone, 10 g yeast extract, 5 g NaCl per litre water

[4] All rotors were Sorvall brand

Purification

Frozen cells were thawed, DNase I (Boehringer Mannheim) added (typically several mg was used) and sonicated for several min The cells were then incubated at 37°C for 30 min with shaking then centrifuged to remove unbroken cells and debris (17,000 rpm, 20 min, SS-34 rotor). The supernatant was loaded onto a 10 cm diameter column (BioRad EconoColumn) containing Fractogel (Novagen) pre-equilibrated with 50 mM tris pH 8.0. The bound protein was washed as follows:

(1) 500 mM NaCl, 50 mM tris pH 8.0

(2) 50 mM imidazole (Sigma), 450 mM NaCl, 50 mM tris pH 8.0

(3) 500 mM imidazole, 50 mM tris pH 8.0

The protein eluted in 500 mM imidazole. As much of the recombinant protein bound heme *in vivo*, it was possible to visually monitor the cyt during purification. The eluted cyt was dialysed against 4 L 100 mM KCl overnight to remove the imidazole. The protein was then concentrated in a Centriprep YM-10 (10,000 molecular weight cut-off, Millipore) filtration unit (typically to a final volume of 10-20 mL) and the buffer adjusted to 20 mM tris, 100 mM NaCl, 5 mM $CaCl_2$, pH 8.0. The cyt was incubated with 30 units of the site-specific protease Factor Xa (Novagen) at 37°C with gentle shaking for 24-48 h. This step was sometimes performed at 4°C for labile mutants. The cleavage was monitored by sodium dodecyl sulfate polyacrylamide gel electrophoresis (SDS-PAGE) (Figure 2.1 a and b). Once cleavage was complete the protein was loaded onto a 5 cm diameter column (BioRad EconoColumn) containing Ni-NTA resin (QIAGEN) pre-equilibrated with 50 mM tris pH 8.0. The flow-through containing the purified cyt was collected and again concentrated in a Centriprep YM-10.

Generally at this stage the protein was considered to be pure, as only one band was visible on an overloaded SDS-PAGE gel stained with Coomassie brilliant blue (Figure 2.1 c). The apparent size of the cyt on the gel was consistent with expectations and N-terminal sequencing confirmed cleavage of the N-term His-tag/linker. If contamination was present the protein was dialysed against 10 mM potassium phosphate (KP_i), pH 7.0. This was loaded onto a DEAE Sepharose (Amersham Pharmacia Biotech) column and eluted with 50 mM NaCl, 10 mM KP_i, pH 7.0. This was sufficient to remove any

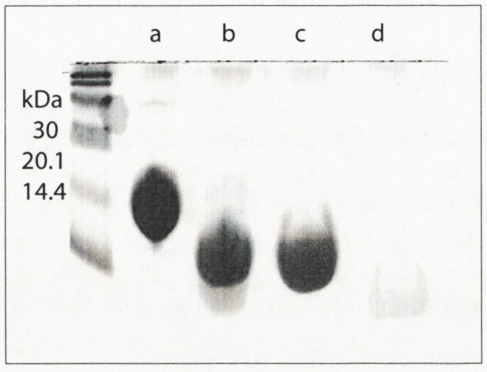

Figure 2.1: SDS PAGE (18% acrylamide) of (a) purified uncut wt-cyt b_{562} protein, (b) Factor Xa-cleaved protein, and purified (c) cyt and (d) N-terminal His tag/linker. The gel is purposefully over-loaded to demonstrate the purity of the sample.

remaining contaminants.

Preparation of Apocyt b_{562}

As much of the cyt contained bound heme, it was necessary to remove this heme before further work could be undertaken. This was achieved using the modified method of Teale (1959) (Ishida *et al.*, 1998). Dropwise 1.0 M HCl was added at 0°C to an aqueous solution of cyt b_{562} until the pH of the solution reached 2.0. An equal volume of methyl ethyl ketone (MEK) (2-butanone) chilled at 0°C was added to this reaction mixture. The mixture was mixed and left to separate. The protoheme fractionated into the MEK and this phase was separated. Additional extractions (typically 3-4) were performed until the organic phase remained colourless and showed no UV/Vis. absorption due to the heme. The aqueous phase, containing the apo-protein was then separated and subjected to repeated dialysis against 100 mM KCl to remove the remaining MEK. The concentration of apo-protein was determined by heme titration (outlined below) or on the basis of absorbance at 277 nm (ε = 3.0 $mM^{-1}cm^{-1}$, Feng & Sligar (1991).

2.2 Cloning and Mutagenesis of a *de novo*-Designed Peptide

Working with Reza Razeghifard I synthesised a gene encoding a 62 residue *de novo*-designed peptide maquette originally designed by Dutton and coworkers (Robertson

et al. (1994); Sharp *et al.* (1998*b*) reviewed in Gibney & Dutton (2001)). This is described in Razeghifard & Wydrzynski (2003). Successive PCR amplification of 5 long contiguous oligonucleotides (primers) was used to create the synthetic gene, which has the sequence: CTG AAA AAG CTG CGC GAG GAA GCG TTA AAA CTT CTG GAA GAA TTT AAG AAA TTG CTG GAA GAA CAT CTG AAA TGG CTA GAA GGT GGC GGC GGT GGC GGG GGC GGT GAG CTC TTA AAA CTG CAC GAA GAA CTG CTT AAA AAG TGC GAG GAA TTA CTG AAA CTG GCC GAG GAA CGT CTC AAG AAA TTG. The sequence of the peptide is given in the following chapter. Mutants were constructed in a similar manner with one or two of the 5 primers modified. The genes were then amplified with LIC-compatable primers and cloned into either pET-30 Xa/LIC or pET 32 Xa/LIC (Novagen) as described for cyt b_{562}. The *de novo* peptides were expressed and purified in a very similar manner to the cyt b_{562} proteins, or with slight modifications as described in Razeghifard & Wydrzynski (2003).

2.3 Porphyrin Binding and K_d Analysis

Apoprotein was reconstituted with freshly prepared hemin chloride, ZnPP, Zn-Ce_6 or other porphyrins by standard literature methods for heme insertion into *de novo*-designed peptides (Gibney & Dutton, 2001; Lombardi *et al.*, 2001) by the slow addition of < 1 μM aliquots of porphyrin (generally in DMSO) to the apoprotein with constant mixing. K_d values for binding were determined by the careful titration of small aliquots of porphyrin into a solution of the apoprotein with the extent of binding monitored by distinctive porphyrin absorbance. Titrations were fit to:

$$\begin{aligned} \Delta\text{Abs} &= \varepsilon_b[\text{bound}] + \varepsilon_s[\text{unbound}] \\ [\text{bound}] &= \tfrac{1}{2}\left(([E_0] + [L] + K_d) - \sqrt{([E_0] + [L] + K_d)^2 - 4([E_0][L])}\right) \\ [\text{unbound}] &= [L] - [\text{bound}] \end{aligned} \tag{2.1}$$

where ΔAbs is the change in absorbance at a wavelength of interest (e.g. Soret maxima) and ε_b and ε_s are the absorption coefficient of protein-bound porphyrin and porphyrin in solution, respectively, at this wavelength, $[E_0]$ is the protein concentration and [L] is the total porphyrin concentration. Typically $[E_0]$ was determined by titration of 200 nM aliquots of hemin or zinc protoporphyrin (ZnPP) into > 2 μM apoprotein

($[E_0] \gg [L] \gg K_d$) and K_d was determined by titration of 10 or 100 nM aliquots of porphyrin into known concentrations of apoprotein at ~10-20x the aliquot concentration.

Hemin chloride and free-base protoporphyrin IX were purchased from Sigma and Ce_6 and ZnPP from Porphyrin Products (Frontier Scientific). All chlorins/porphyrins were used as supplied and only fresh stock solutions in DMSO were used. Hemin concentration was determined by $\varepsilon_{385nm} = 58.4\ mM^{-1}cm^{-1}$ in water. Zn-Ce_6 was obtained by metallation of free-base Ce_6 by a modified method of Razeghifard & Wydrzynski (2003).

Bis-imidazole ligated heme was prepared by the addition of 100 mM imidazole to freshly-prepared stirred hemin in solution weakly buffered to pH 8. The concentration of hemin was kept below ~20 μM to reduce aggregation. The sample was then buffered with 50 mM KP_i and the pH adjusted to 7.0.

2.4 Quinone Binding

Quinones were bound to apo-I17C, apo-L30Y or apo-L30H by adding a 5-fold molar excess of quinone to the protein at pH 7.0, which was allowed to react for 30 min with gentle mixing. Quinones, all obtained from Sigma, were made fresh in ethanol. This was done in the dark. The unbound quinone was then removed by dialysis. Following dialysis there was no detectable unbound quinone as measured by EPR. All bound quinone was in the oxidised state as measured by absorbance and fluorescence. If the I17C protein is gently bubbled with oxygen in 50 mM bicarbonate at pH 9, it quickly becomes cross-linked due to intra-protein disulfide bond formation. This was not observed with the quinone-bound I17C protein, suggesting that labelling occurs with near unit efficiency. As the I17C (and other L30 proteins) become crosslinked during the purification process, the proteins were treated with dithiothreitol and dialysed at pH 5 in 1 mM sodium acetate (to prevent re-reduction) prior to quinone binding. No cross-linked protein was detected by non-reducing SDS-PAGE after this treatment.

2.5 Experimental

Chromatography

Size-exclusion chromatography was typically performed on two Protein Pak 300sw columns (Waters) at 1 mL min^{-1} in 10 mM KP_i, pH 7.0 with detection at 220 nm. The column was calibrated using insulin (5.7 kDa), ribonuclease S (11.5/2.2 kDa), horse heart cyt c (12.3 kDa), lysozyme (14.4 kDa), myoglobin (17 kDa), chymotrypsenogen A (25.7 kDa), pepsin (36 kDa), catalase (60 kDa) and bovine serum albumin (67 kDa).

Optical Spectroscopy

CD spectroscopy was performed on a ISA Jobin Yvon CD 6 spectropolarimeter (Instruments S. A. Inc.) at room temperature using a 0.1 or 1 cm quartz cell for the UV and Soret region, respectively. Absorbance measurements were made on a Varian Cary 300 spectrophotometer or OLIS RSM rapid-scanning spectrophotometer. 1 cm pathlength cuvettes were used unless stated otherwise. Steady-state fluorescence measurements were made on either an SLM 8100 (Spectronic, Rochester, NY) or Spex FluoroMax-3 (Jobin Yvon Horiba).

Fluorescence polarisation measurements were made with an SLM 8100 in the L-format. For the dilution experiments described in Chapter 3.3, each measurement was made with excitation and emission at 280 and 340 nm, respectively and a 5 nm slit width. Ten measurements were averaged at each point and the G-factor continuously measured.

Fluorescence decay kinetics were obtained by the time correlated single photon counting technique as outlined previously (Ghiggino & Smith, 1993; Sisido *et al.*, 2001) with a rhodamine 6G dye laser pumped by a SESAM mode-locked diode pumped solid state laser (Time-Bandwidth, Cheetah X) at ~600 nm and emission at 650 nm. The observed decay curves were analysed by non-linear least squares iterative reconvolution into multicomponent exponential functions by using a repeated reconvolution program (Ghiggino & Smith, 1993).

Denaturation

Guanidine denaturation was performed by incubation of the protein in guanidine for at least one hour at 20°C before measurement. The sample typically also contained 50 mM KP_i, 100 mM KCl, pH 7.0. For the cyts, the degree of denaturation was followed by bound heme Soret absorbance and fit to a two state transition of the form:

$$\text{fraction folded} = 1/[1 + \exp(-(\Delta G^{H_2O} - m[Gdn])/RT)], \tag{2.2}$$

according to the method of Pace (1986).

Thermal denaturation of M7H (Chapter 3) was performed with the aid of a circulating waterbath. The temperature was increased in 2-5° increments and the samples equilibrated for > 5 min before measurement. The extent of unfolding was determined by Soret absorbance for holo-proteins or second derivative UV absorbance for the apo-protein. The data were corrected with first order baselines and ΔH and T_M determined from the derivative of the data. ΔG was calculated from this using the Gibbs-Helmholtz equation:

$$\Delta G = H_{vH}(1 - T/T_M) - \Delta C_P(T_M - T - T\ln(T/T_M)) \tag{2.3}$$

with ΔC_pvalues of 2.3 kJ mol^{-1} for apo-protein and 3.8 kJ mol^{-1} for holo-protein which were determined previously for apo- and holo-wt cyt b_{562}, respectively (Robinson *et al.*, 1998).

Electron Paramagnetic Resonance

Low-Temperature EPR: Heme

EPR measurements of Fe(III)-heme were performed on a Bruker ESP 300E spectrometer at 9.4 GHz. This was done with Karin Ahrling. All measuerments were made at 10 K and 20% glycerol was used as a cryoprotectant in all samples. When necessary g_x values were calculated by the method described in Walker *et al.* (1986) by:

$$g_x^2 + g_y^2 + g_z^2 - g_x g_y - g_x g_z + g_y g_z + 4g_x - 4g_y - 4g_z = 0. \tag{2.4}$$

The ligand field parameters V (rhombic splitting) and Δ (tetragonal splitting) were calculated using the method described in Taylor (1977) from the 3 low-spin g tensors.

These were calculated in units of λ (spin-orbit coupling constant) where:

$$V/\lambda = g_x/(g_z + g_y) + g_y/(g_z - g_x) \quad (2.5)$$

$$\Delta/\lambda = g_x/(g_z + g_y) + g_z/(g_y - g_x) - 1/2V/\lambda \quad (2.6)$$

$$\text{with} \quad g_z > g_y > g_x \quad (2.7)$$

Room Temperature EPR

X-band EPR spectra were acquired at room temperature on a Bruker ESP300E spectrometer equipped with a TM011 cavity. Generally the spectra were aquired at 1-4 mW microwave power with 1.0 G modulation amplitude and 100 KHz modulation frequency. A conversion time of 41 ms, and a time constant of 81.9 ms was generally used with a subsequent sweep time of 42 s. Generally multiple (5-50) scans were averaged. Unless stated otherwise, all samples were made anaerobic by the addition of glucose oxidase, glucose and catalase. When necessary, the samples were excited with saturating 10 μs xenon flashes from an EG&G electrooptic flash lamp. A non-magnetic optical fiber was used to illuminate the sample within the cavity. The sample was typically in a flat cell which allowed better signal-to-noise and light-saturation. There was negligible UV-excitation in this set up. The transient EPR spectra were acquired essentially as described by Razeghifard & Wydrzynski (2003), although the time constant and microwave power were varied. These parameters are given in the figure legends.

Redox Measurements

Chemical Potentiometry

Redox titration data were fit to a single Nernst curve of the form:

$$\text{fraction reduced} = 1/\left[1 + 10^{(\mathrm{E-Em})/(59/\mathrm{n})}\right], \quad (2.8)$$

where E is the solution redox potential in units of mV vs. the standard hydrogen electrode (SHE). The data was typically fit with n as a free variable. In the case of the *de novo*-designed peptides with multiple bound hemes, eqn 2.8 was modified to:

$$\text{fraction reduced} = \left(\mathrm{c}/\left[1 + 10^{(\mathrm{E-Em1})/59}\right] + (1 - \mathrm{c})/\left[1 + 10^{(\mathrm{E-Em2})/59}\right]\right), \quad (2.9)$$

where E_m1 and E_m2 are the two midpoint potentials, and c is the relative population of the heme molecules. c falls between 0 to 1 and in protein fully occupied with 2 heme, c = 0.5.

Heme

Heme redox potentiometry was performed essentially by the method of Dutton (1978) in an anaerobic cell continuously flushed with nitrogen. The mediators (10 μM) used were a mixture of some or all of the following depending on the potential scanned: 1,4-benzoquinone, diamino duroquinone, phenazine methosulphate, phenazine ethosulphate, duroquinone, 1,2-naphthoquinone, 1,4-naphthoquinone, trimethyl hydroquinone, juglone and riboflavin-5′-monophosphate. The titrations were performed in an oxidising direction by the addition of ferricyanide and in the reducing direction with buffered sodium dithionite. The extent of heme reduction was measured by the α band absorbance intensity at about 560 nm. The samples were in 100 mM KCl and buffered with 50 mM sodium acetate, KP_i or tris as required. The solvent potential was measured with a KCl-saturated calomel electrode and a Pt counter electrode which was calibrated against 1:1 ferri/ferrocyanide (+430 mV).

Quinone

The redox potential of the quinones was measured by chemical redox titrations, again essentially as described by Dutton (1978). All samples were rigorously made anaerobic by continuously flushing the sample with nitrogen. These experiments were performed with ~100 μM quinone and 5 μM each mediator. The mediators were some, or all of those mentioned above for heme. As the mediator concentration is quite low, the sample was left to equilibrated for 5-10 min after the addition of ferricyanide or dithionite. The extent of quinone reduction was monitored simultaneously at 300 nm and ~350 nm. Semiquinone absorbance at 425 nm was also monitored but never observed. Measurements were made in 100 mM KCl, 50 mM KP_i, pH 7.0 against a KCl-saturated calomel electrode and a Pt counter electrode. The redox titration data were fit to a single Nernst curve (eqn 2.8) with n as a free variable to determine whether the reacation showed n=1 or n=2 behaviour.

Electrochemistry

Conventional 3-electrode cyclic voltammetry was performed with a 3 mm diameter polished glassy carbon working electrode, Pt counter electrode and Ag/AgCl (sat. KCl) reference (all from Bioanalytical Systems, Inc.). Electrochemistry was performed with a Princeton Applied Research model 263A potentiostat (EG&G Instruments, Inc.) driven by a PC. The samples were continuously flushed with nitrogen and the temperature maintained at 25°C with a circulating water bath.

Molecular Modelling

The various cyt b_{562} mutations were modelled by selective geometry minimisation in a periodic box with the AMBER94 forcefield in HYPERCHEM (6.03 evaluation copy, Hypercube, Inc.). The porphyrins and quinones were similarly modelled with the mm+ force field. The electronic coupling and PATHWAYS calculations in porphyrin-protein-quinone complexes (Chapter 5) were done with HARLEM[5]. Figures were drawn with Swiss-PdbViewer (v3.7).

[5]Kurnikov, I. V. (2000) HARLEM molecular modelling package, v1.0, Department of Chemistry, University of Pittsburgh, Pittsburgh, PA

CHAPTER 3

Porphyrin Binding

This chapter describes the binding of various porphyrin and chlorin molecules[1] to small proteins and peptides. The aim of this work was to generally characterise the binding of 5-coordinate porphyrins to peptides and more specifically, to construct a small and soluble peptide capable of binding an excitonically-coupled dimer of chlorophyll (Chl) analogues, thus mimicking the primary donor of a reaction centre.

3.1 Introduction

The most prevalent cofactor in photosynthesis is (bacterio)chlorophyll ((B)Chl). In the reaction centres (B)Chl is optimised to form a finely-tuned oxidant and allow vectorial ET (Moser *et al.*, 1995; Parson, 1996), yet in the light harvesting antenna (B)Chl is involved in exciton transfer (Gobets & van Grondelle, 2001; Cogdell *et al.*, 2003). The different functions of the (B)Chls in the light harvesting complexes (LHCs) and RCs is controlled by the protein environment, which tunes the local dielectric and provides specific molecular interactions. These molecular interactions include hydrogen bonding, hydrophobic interactions and metal ligation. Through this, the protein is able to fine-tune: (*i*) $E_{0,0}$, (*ii*) E(Chl/Chl$^{+\cdot}$) and thus ΔG^0; (*iii*) λ; (*iv*) the cofactor distance and orientation and (*v*) the electronic coupling through the bridging amino acids; and (*vi*) the spectral properties of (B)Chl which govern light absorption. In essence the protein environment is able to modulate nearly every variable in the ET reaction (see Chapter 1.4).

One approach to study the interactions between the protein and (B)Chl is to study mutants of the RCs, and this has been described in Chapter 1.3. A similar approach involves the reconstitution of RC or LHC proteins with (B)Chl. Much of this work has been performed by Loach and co-workers using BChl-reconstitution of native and mutant/truncated LHC peptides (see for example (Davis *et al.*, 1997; Kehoe *et al.*, 1998; Todd *et al.*, 1998)). Another approach involves the construction of small (B)Chl-binding peptides. These offer several advantages (and a few disadvantages) to the natural systems. Typically the peptides can be modified, without major structural disruption,

[1]Unless explicitly stated, the term porphyrin will be used to describe both porphyrins and chlorins

to test the effect of a local environment change. In addition, molecular modelling of the peptide-(B)Chl complex is much less intimidating (and time-consuming) in these small systems than in a RC or light harvesting complex. This allows a rational approach to the design of these peptides. A problem arises however, as analogues of (B)Chl are needed for such studies. It is both difficult and unnecessary to design a (B)Chl binding pocket that can accommodate the phytyl tail of (B)Chl. In previous studies, (B)Chl analogues have been covalently attached to peptides. A *de novo*-designed peptide, that covalently bound two free-base coproporphyrin molecules that could dimerise forming a "special pair", was described by Rabanal *et al.* (1996). More recently, (Rau *et al.*, 2001) covalently attached Zn-methyl-pyropheophorbide *b* and *d* to the exterior of a *de novo*-designed peptide. With this approach the (B)Chl analogues are solvent-exposed and also lack the protien-metal (Mg) ligation that is common to (B)Chl binding in the natural systems. Several heme-binding proteins such as myoglobin have been reconstituted with (B)Chl analogues (Wright & Boxer, 1981) and these offer a more natural binding environment. Porphyrin binding to a protein usually involves axial ligation and this is most commonly to a His in the case of (B)Chl. The hydrophobic phytyl tail in (B)Chl, and (B)Pheo must also play a major role in binding as (B)Pheo is protein-bound yet is unable to form an axial bond. There have been reports of peptides that bind (B)Chl through His ligation. these include myoglobin (Wright & Boxer, 1981), peptide fragments of natural (B)Chl-binding proteins (Eggink & Hoober, 2000), and few reports of specifically-designed (B)Chl-binding peptides (Dudkowiak *et al.*, 1998, 1999; Kashiwada *et al.*, 1999; Razeghifard & Wydrzynski, 2003). His ligation is also the mode of heme binding and there is a wealth of literature describing *de novo*-designed heme-binding peptide maquettes (reviewed in (Gibney & Dutton, 2001) and mentioned in Chapter 1.2).

The work presented in this chapter describes the binding of heme and other porphyrins and chlorins to a family of *de novo*-designed peptides, to mutants of the *E. coli* cyt b_{562} and finally to a novel semi-synthetic peptide. The role of axial ligation is discussed and the effect of the axial ligand on the properties of heme are explored. Although much of this chapter describes work with heme, many of the observations are also valid for the binding of (B)Chl analogues.

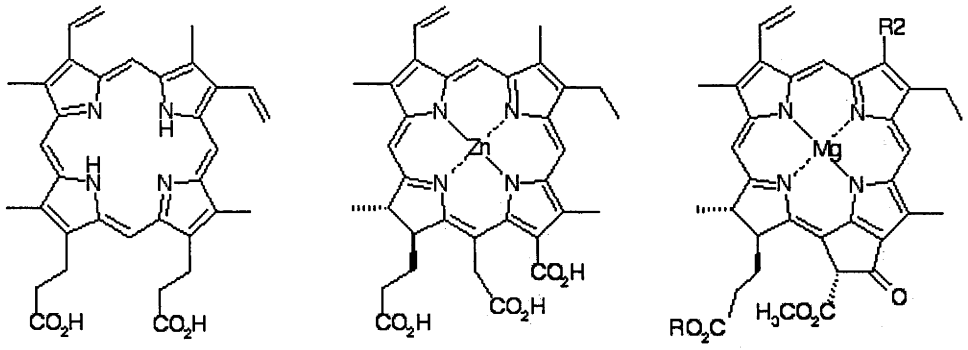

Figure 3.1: The various porphyrins used in this work. Left, free-base protoporphyrin IX (PPIX), which can be metallated with zinc or iron to create zinc-PPIX (ZnPP) and heme, respectively. Centre, zinc-chlorin e6 (Zn-Ce_6). Right, chlorophyl (R = phytyl tail, R2 = methyl (Chl *a*) or formyl (Chl *b*)

The Porphyrins

The porphyrins used in this work were principally iron protoporphyrin IX (heme); zinc-protoporphyrin IX (ZnPP); zinc-chlorin e6 (Zn-Ce_6); and Chl *a* and *b* (Chl*a*, Chl*b*). Some of these porphyrins are shown in Figure 3.1. Upon binding to a protein, heme forms axial ligands with one or two protein side chains. The amino acid side chains of His, methionine (Met), lysine, asparagine, tyrosine, proline and cysteine are able to act as such ligands forming nitrogen-, sulfur- or oxygen-iron bonds. The amino terminus has also been shown to act as a ligand. As is the case of (B)Chl discussed above, this bonding has a major role in regulating the properties of the ligated heme. Additionally, the bonding may be playing a significant role in the stabilisation of the heme-protein complex. In the cyts *bis*-His (*bis*-His) and Met/His ligation are much more common than the other forms of ligation where *bis*-His ligation predominates in the *b*-type cyt and Met/His ligation is generally found in the *c*-type cyts.

There are several key differences between iron- and zinc-metallated porphryins: (*i*) Fe can be either five or six coordinate and thus be ligated by one or two amino acid ligands. Zn is only five coordinate and thus forms only a single bond with the protein. (*ii*) Fe very efficiently quenches the porphyrin excited state. Thus the Fe-porphyrins do not fluoresce and, as the excited state lifetime is extremely short, are unable to act as

light-induced electron donors. (*iii*) Unlike Zn- (and Mg-), Fe-porphyrins can undergo a metal-centred ET reaction with the iron converting between the +2 and +3 oxidation states. Therefore, whilst not involved in light-induced ET, heme proteins are involved in ubiquitous ET reactions. (*iv*) Fe(III)-heme is high spin (S = 5/2) and thus paramagnetic. If upon protein binding the heme becomes 6-coordinate, through *bis*-ligation, the heme becomes low spin (S = 1/2). The HS and LS Fe(III)-heme has considerably different absorbance and EPR properties, which allows a relatively unambiguous assignment of the binding of this porphyrin to a peptide. The Zn- and Mg-porphyrins are not paramagnetic and thus do not offer such an easily-measurable property of peptide binding.

The light-active[2] porphyrins used in this study are Zn-Ce_6, ZnPP and the Chls *a* and *b*. Little work was done with the Chls due to their photo-lability, tendency to aggregate and the complications associated with their large phytyl tail. The porphyrins Zn-Ce_6 and ZnPP are reasonably well behaved in aqueous solution (in terms of solubility and aggregation) and principally donate an electron from the singlet and triplet state, respectively (discussed in Chapter 5). The triplet formation of ZnPP requires most work to be carried out anaerobically to prevent the formation of damaging reactive oxygen species. ZnPP was purchased and used as supplied. Zinc-metallated chlorin e_6 is not commercially available so the metal had to be inserted. This proved to be relatively straightforward and the 1:1 addition of Zn acetate to the chlorin in methanol or alkaline solution resulted in complete metallation after several hours (data not shown, see Razeghifard & Wydrzynski (2003)).

Imidazole Complexes of Zn-Ce_6 and ZnPP

As mentioned earlier, His ligation is important in the protein-binding of (B)Chl. Imidazole is a simple His analogue and was initially used to determine the effect of His ligation on the absorbance properties of Zn-Ce_6 and ZnPP.

The *bis*-imidazole heme complex has been prepared before (Shifman *et al.*, 1998). This is used later in Section 3.11 and the preparation of this complex is described in

[2]In this work a light-active porphyrin is any porphyrin or chlorin, which upon illumination forms an excited state from which energy transfer or ET can occur.

Chapter 2.3. A difficulty arises when working with this complex as it has a tendency to aggregate. This aggregation is minimised by working at pH ~8.5 (Shifman *et al.*, 1998) and at low concentration. An alternative is to work in non-aqueous solvents such as ethanol or methanol. As mentioned above, there are significant absorbance shifts that occur upon formation of the *bis*-imidazole Fe(III)-heme complex as the heme becomes low spin. No such conversion is possible for Zn-Ce_6 or ZnPP but the imidazole complexes were examined to determine whether there were any characteristic absorbance changes associated with ligation.

Imidazole was titrated into 10 μM solutions of Fe(III)-heme, ZnPP and Zn-Ce_6 in methanol. The titrations of heme and ZnPP are shown in Figure 3.2. The absorbance spectra of Zn-Ce_6 and imidazole-ligated Zn-Ce_6 are shown in Figure 3.17. The imidazole complexes of both ZnPP and Zn-Ce_6 are slightly red-shifted relative to the unligated porphyrin. The relative intensity of the ZnPP α and β bands (at about 590 and 550 nm, respectively) have been shown to be diagnostic of zinc-ligation (Hoffman, 1975; Nappa & Valentine, 1978) and this is consistent with the results obtained in this experiment. The data in Figure 3.2 were fit to the following model:

$$\mathrm{P} + \mathrm{nIm} \rightleftharpoons \mathrm{P} - \mathrm{Im_n},\ K_\mathrm{d} = \frac{[\mathrm{P}][\mathrm{Im}]^\mathrm{n}}{[\mathrm{P} - \mathrm{Im_n}]}, \tag{3.1}$$

where P is a porphyrin, n is the number of imidazole (Im) ligands formed (1 or 2) and $\mathrm{P} - \mathrm{Im_n}$ is the imidazole complex of the porphyrin. If the K_d is relatively large (binding is weak) then there will be an excess of ligand relative to porphyrin such that $[\mathrm{Im}] \gg [\mathrm{P}]$ ($[\mathrm{Im_T}]$ is the total imidazole concentration), and as $[\mathrm{Im_T}] = [\mathrm{Im}] + [\mathrm{P} - \mathrm{Im_n}]$ then $[\mathrm{Im_T}] \sim [\mathrm{Im}]$. To further simplify matters we can assume that ligation of the porphyrin by one imidazole does not effect the binding of another imidazole (if $\mathrm{n} > 1$), such that the two binding "sites" are equivalent. Thus, the data in Figure 3.2 can be fit to:

$$y = y_{min} + \Delta y \left(\frac{[\mathrm{Im_T}]^\mathrm{n}}{K_\mathrm{d} + [\mathrm{Im_T}]^\mathrm{n}} \right), \tag{3.2}$$

where y is any change in absorbance or peak position. This is a useful expresson, as one not only obtains the K_d value but also the binding stoichiometry. The K_d and stoichiometry values for the titrations in Figure 3.2 are given in Table 3.1. The data quite clearly show that while Fe(III)-heme forms two His ligands, ZnPP and Zn-Ce_6

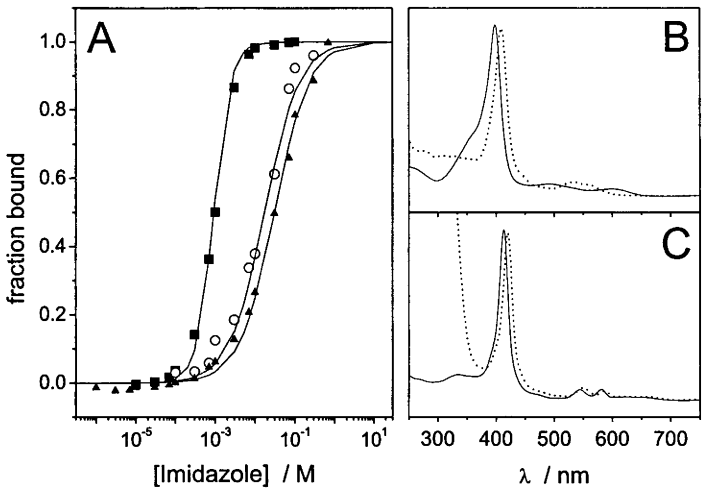

Figure 3.2: (A) Binding isotherms of imidazole ligation to Fe(III)-heme (squares), ZnPP (circles) and Zn-Ce_6 (triangles) in methanol. (B) and (C) Fe(III)-heme and ZnPP, respectively, in the absence (solid line) and presence (dotted line) of excess imidazole.

Table 3.1: Binding energies of porphyrin ligation by imidazole

Porphyrin	K_d (mM)	$\Delta G_{binding}$ (kJ mol^{-1})	n[a]
Fe(III)-heme	0.92[b] $\pm$ 0.06	17 $\pm$ 1	2
ZnPP	17 $\pm$ 2	10 $\pm$ 1	1
Zn-Ce_6	30 $\pm$ 2	8.5 $\pm$ 0.6	1

[a]The stoichiometry of imidazole to porphyrin. [b]Fe(III)-Heme data were fit to eqn 3.2 for 2 ligands and a K_d of 0.85 μM. However, the binding of Fe(III)-heme to one imidazole occurs with $K_{d,1} = \sqrt{K_{d,2}}$ and is thus 0.92 mM.

form only a single ligand each and these (five-coordinate) porphyrins are ligated more weakly than heme. ZnPP has been quite well-characterised and clearly shown to form a single His ligand upon protein binding (see e.g. (Sharp *et al.*, 1998*a*)). The same was expected of Zn-Ce_6 and this was shown to be the case.

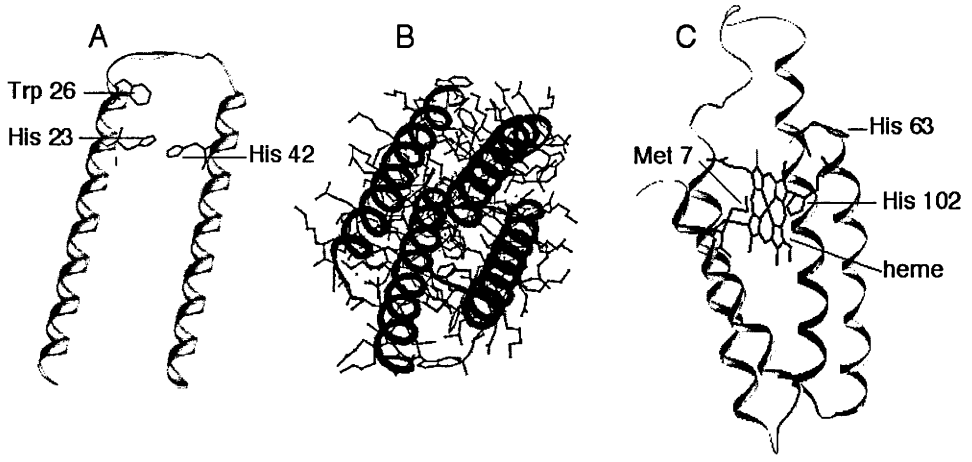

Figure 3.3: The Proteins (not to scale). (A) Molecular model of a monomer of the synthetic peptide H23H42 and (B) X-ray crystal structure of a *de novo*-designed four-helix-bundle (1M3W.pdb) approximately looking down the long-axis of the peptide showing dimerisation. (C) X-ray crystal structure of cyt b_{562} (256b.pdb).

The Proteins

The *de novo*-designed peptides used in this work were designed by Dutton and coworkers as heme-binding maquettes (Robertson *et al.* (1994) reviewed in Gibney & Dutton (2001) and Chapter 1.2). The general structure of these peptides is shown in Figure 3.3. The peptide is designed to form to helix-loop-helix hairpin structure, which dimerises to form a four-helix bundle (Gibney *et al.*, 1997, 1998; Sharp *et al.*, 1998*b*; Huang *et al.*, 2003). The placement of the His is designed to allow the *bis*-ligation of 1 heme molecule per peptide monomer. The peptides used here have the general sequence: ML·KKLREEA·LKLLEEF·KKLLEEX_1·LKWLEGGGGGGGGELLKL·X_2EELLKK·CEELLKL·AEERLKK·L. The heptad repeats (Chapter 1.2) are delineated with dots. They differ from the design of Sharp *et al.* (1998*b*) only in the N-terminal Met which was added as a consequence of expression system we used. Several variants have been made by either myself or Reza Razeghifard and the peptides are named after the position of porphyrin ligands. When X_1 and X_2 are both His, the peptide is H23H42; X_1 and X_2 are both Phe in F23F42; X_1 is His and X_2 is Phe in H23F42; and X_1 is His and

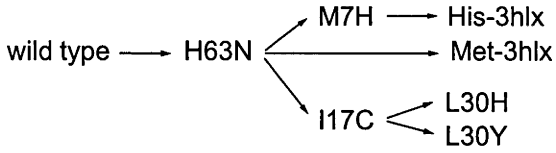

Figure 3.4: The cyt b_{562} variants used in this work

X_2 is Met in H23M42.

The *E. coli* cyt b_{562} is a small, soluble four-helix-bundle protein with a single *b*-type heme cofactor originally described by Itagaki & Hagar (1966) and described in Chapter 1.2. Various mutants[3] of cyt b_{562} were made during the course of this work. Some are double, triple and quadruple mutants. Their relationship to each other are shown in Figure 3.4. The arrows denote a single amino acid mutation except in the case of the 3hlx mutatnts which are explained later in Section 3.4. All of the cyt b_{562} proteins in this work have an N-terminus methionine (M0) as a result of the expression plasmid used. This additional methionine is expected to be > 15 Å from the heme iron and we have seen no evidence for it playing any role in porphyrin-binding. Wildtype[3] cyt b_{562} (wt) has a solvent-exposed His residue at position 63 which we replaced with an asparagine creating the H63N mutant. This is essentially the wt protein in this work. The rationale for the H63N mutation was to prevent the adventitious binding of porphyrins to this solvent-exposed residue upon reconstitution of the apo-protein. Additionally, His 63 has been mutated in cyt b_{562} by other groups (Wittung-Stafshede *et al.*, 1997) without problems. The methionine and H63N mutations did not effect the absorption, redox, or EPR properties of the ferri-protein relative to the wt (see Table 3.2) and had no measurable effect on the chemical stability of the protein (ΔG^{H_2O} ferri-wt = 29, ferri-H63N = 28 kJ mol^{-1}).

Both the synthetic peptide maquettes and cyt b_{562} mutants were overexpressed in *E. coli* using the pET-30 Xa/LIC system. This yielded pure cyt up to about 50 mg pure protein per L of culture (a little less for the maquettes). Typically about 20-30% of the

[3]While traditionally the terms wt and mutant are used to refer to an organism, I will use them to describe individual proteins.

cyt contained bound heme, but this was never observed in the case of the maquettes. It is interesting to note that the cyt was expressed with an N-terminus consisting of a ~4 kDa fused His-tag/linker in place of the usual periplasmic signalling sequence, yet heme was still incorporated into the recombinant protein to a level of over 1 μmol heme per L of culture which resulted in distinctive red/pink coloured *E. coli* after several hours of protein expression. The maquettes were also expressed in *E. coli* but did not bind any heme *in vivo*. This is not purely a result of tight heme binding in cyt b_{562}, as the K_d values of heme binding to the cyts and maquettes are generally fairly similar (Table 3.3). When necessary the heme was removed from the purified cyts by the method of Teale (1959) and reconstitution of the apoproteins with Fe(III)-heme resulted in indistinguishable characteristics relative to those of the endogenous heme-containing cyts.

3.2 *Bis*-His vs. His/Met Ligation

The two experimental systems used in this work, the *de novo*-designed peptides and the "natural" *E. coli* cyt b_{562} both bind heme. However, the maquettes bind heme through *bis*-His ligation while cyt b_{562} binds heme atypically (for a *b*-type cyt) through His/Met ligation. In order to better compare these two systems a maquette with a His/Met motif (H23M42) and cyt b_{562} mutant with *bis*-His ligation (M7H) were constructed. Neither of these peptides have been previously described. The characterisation of these peptides follows, after which the characterisation of Zn-Ce_6 binding to these peptides is discussed.

M7H

Molecular Modelling

Molecular modelling of the M7H mutation suggests that the substitution of the heme-ligation Met at position 7 with His will disrupt the heme binding pocket of the protein. Figure 3.5 A shows a model of the mutant and Figure 3.5 B shows the disruption the M7H mutation is thought to have on the heme binding site. The bulkier His is expected to disrupt the N-terminal α-helix around position 7. Additionally, the C-terminal helix

Table 3.2: Absorbance and redox properties of heme-bound peptides and *bis*-imidazole-ligated heme

Protein	[1]Ligation	Absorbance Maxima (nm)		$^{2}E_{m7}$
		oxidised	reduced	
wt b_{562}	H/M	418, 529, 558[a]	427, 531, 562[a]	+189[d]
H63N	H/M	418, 530, 560	427, 531, 561	+187
M7H	H/H	415, 537, 566	426, 531, 558/561[3]	-73
$(\alpha\text{-}l\text{-}\alpha)_2$	H/H	411, 530, 560[b]	424, 529, 559[b]	-105, -120[c]
H23H42	H/H	412, 530, 560	425, 529, 558	-55,-145
H23M42	H/M	413, 530,560	426, 529, 559	-140
bis-Im-Heme	Im/Im	409, 534, 563	421, 526, 556	-143

[1] Heme ligation by *bis*-His (H/H), His/Met (H/M) or *bis*-imidazole (Im/Im); [2] The midpoint potentials were measure in mV vs. the SHE at pH 7, except for [c], which was measured at pH 8; [3] The α band of M7H is partially split. Additional data taken from (*a*) Itagaki & Hagar (1966), (*b*) Gibney *et al.* (1998), and (*c*) Sharp (1998).

is more disordered due to the movement of the heme to accommodate the additional His. Together this will probably result in a more solvent-exposed heme. The modelling also indicates that the two His imidazole moieties will not be in-plane and this is supported by EPR measurements below.

Heme Absorbance

The absorbance spectra of H63N and wt cyt are indistinguishable (data not shown). The absorbance spectra of oxidised and reduced H63N and M7H are shown in Figure 3.6 and the peak maxima are listed in Table 3.2. The spectra are all typical of low-spin cyts. The Soret band is blue-shifted by 3 and 1 nm, respectively in ferri- and ferrous-M7H relative to H63N. Ferrous M7H auto-oxidises very quickly. The α band of reduced M7H is broadened and somewhat split relative to wt and also shows a decreased intensity from 32 $mM^{-1}cm^{-1}$ to 24 $mM^{-1}cm^{-1}$. This is shown in the inset of Figure 3.6

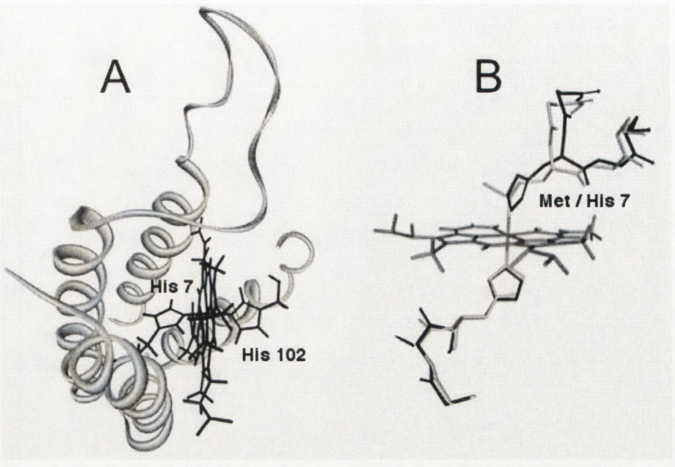

Figure 3.5: (A) Molecular model of the M7H mutant of cyt b_{562}. The model is an energy minimised structure based on PDB file 256B created in HyperChem (Hypercube Inc.) using the Amber94 force field with a periodic box. (B) The heme ligating side chains of M7H and wt cyt b_{562}. In grey is the coordinates from the wt protein. The two structures were aligned using the heme molecule. The backbone of the two amino acids either side of Met/His 7 and His 102 are shown to highlight the perturbations the M7H mutation is thought to create near His 7.

relative to that of H63N. Heme bound through His/Met ligation in the oxidised state has a characteristic absorbance band at about 695 nm in cyt *c* (Dickerson & Timkovich, 1970) and 720 nm in wt cyt b_{562} (Moore *et al.*, 1985) at neutral pH. This absorbance is thought to arise from charge transfer (CT) from the Met sulfur to the heme Fe(III) (Eaton & Hochstrasser, 1967). We observed this CT band in the wt (and H63N) cyt at about 720 nm at pH 7 but, as expected, it is not visible in M7H (data not shown)

The absorbance spectra of oxidised and reduced M7H are not remarkable except for the unusually broad and partially split α band of ferrous M7H (Figure 3.6, Table 1). Splitting of the α band is uncommon but is seen in the split α cyts (Meyer & Kamen, 1982). Such splitting was recently reported for a heme-ligating Met to His mutant of *Pseudomonas* cyt c_{551} (Miller *et al.*, 2000) and may be a characteristic of the perturbed ligand environment of Met to His cyt *b* mutants. Interestingly no splitting of this α band has been reported for the synthetic heme binding peptides of Dutton and others, yet these peptides are expected to have an unusual heme-binding environ-

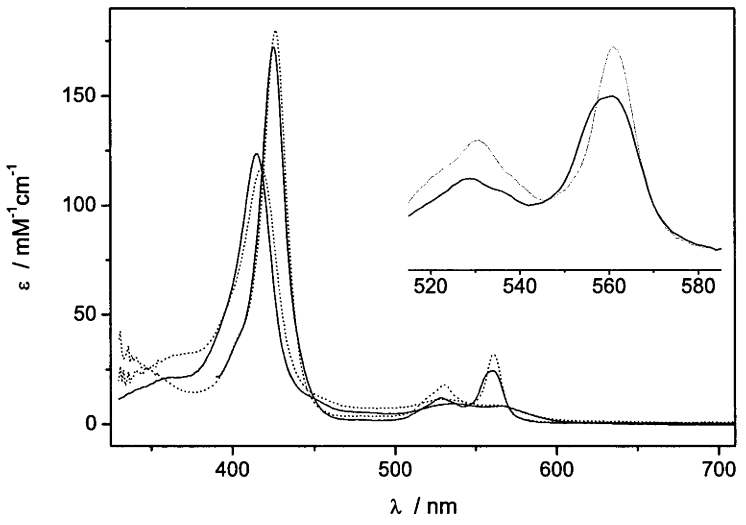

Figure 3.6: Absorbance spectra of oxidised and reduced H63N (dotted lines) and M7H (solid lines) mutants of cyt b_{562}. The peak positions are given in Table 3.2. The inset shows the α and β bands of the ferrous cyts and highlights the splitting of the M7H α band.

ment (reviewed in Gibney & Dutton (2001)). No changes in the absorbance spectra of freshly-reconstituted holo-M7H are observed on the minutes-to-days time-frame suggesting this splitting is not due to heme orientation disorder. Rather, this splitting is probably due to asymmetry of the bound heme (see for example (Reddy *et al.*, 1996)) perhaps due to iron movement out of the porphyrin plane or slight deformation of the porphyrin due to steric strain. The absorbance bands of both ferri- and ferrous-M7H are blue-shifted relative to those of H63N. This is consistant with previous experiments, which have shown that axial ligation can shift the absorbance maxima of bound heme. The N-acetylmethionine complex of ferric microperoxidase-8, which contains His/Met-ligated Fe(III)-heme, has a Soret absorbance maxima 1.5 and 3.0 nm to the red of the respective N-acetylHis and imidazole complexes (Othman *et al.*, 1994; Othman & Desbois, 1998). An alternate explanation for these shifts is the observation that increasing the solvent polarity causes blue-shifting of the absorbance maxima of model heme complexes (Romberg & Kassner, 1982). Thus the shifts observed between M7H

Table 3.3: Heme binding constants

Protein	K_d[a] (nM)		$\Delta\Delta G$[b]
	(Fe(III)-heme)	(Fe(II)-heme)	(kJ mol^{-1})
H63N	13 ± 3	2.8 ± 0.6	3.8
M7H	< 1	20 ± 3	> 7
maquette[c]	<1, 400	42, 15,000	>9, 8.8

[a] Determined by optical titrations fit to eqn 1 as described in the text, or [c]Data for a *de novo*-designed maquette taken from Reedy *et al.* (2003); [b] Difference in the energetics of Fe(III)-heme binding relative to Fe(II)-heme binding to each protein ($\Delta G = -RTln(K_d1/K_d2)$).

and H63N are probably due both to the different axial ligation and additional solvent-exposure of heme in M7H.

Heme Binding

The careful of titration of heme into the apo-cyts was used to calculate K_d values, which are given in Table 3.3 Representative titrations are shown in Figure 3.7. Fe(III)-heme-binding to wt cyt b_{562} was measured by calorimetry to have a $K_d$of 9 nM (Robinson *et al.*, 1997) and agreement with the value obtained for H63N further suggests that the N-terminus Met and H63N mutations have little effect on cyt b_{562}. Interestingly, both the wt and M7H apo-proteins bind a free-base protoporphyrin IX with μM affinity shifting the Soret absorbance from 393 to 408 nm despite the lack of any metal ligation (data not shown).

Circular Dichroism.

The far-UV circular dichroism (CD) spectra of the apo- and Fe(III)-heme-reconstituted M7H are shown in Figure 3.8. Upon fitting of the CD spectra, the helical content of the apo form of M7H was estimated to be 54%. This is similar to the value of 57% reported for wt apocyt (Feng & Sligar, 1991). Upon reconstitution of M7H with Fe(III)-heme there was a small increase in helicity to ~60% and this was sensitive to buffer condi-

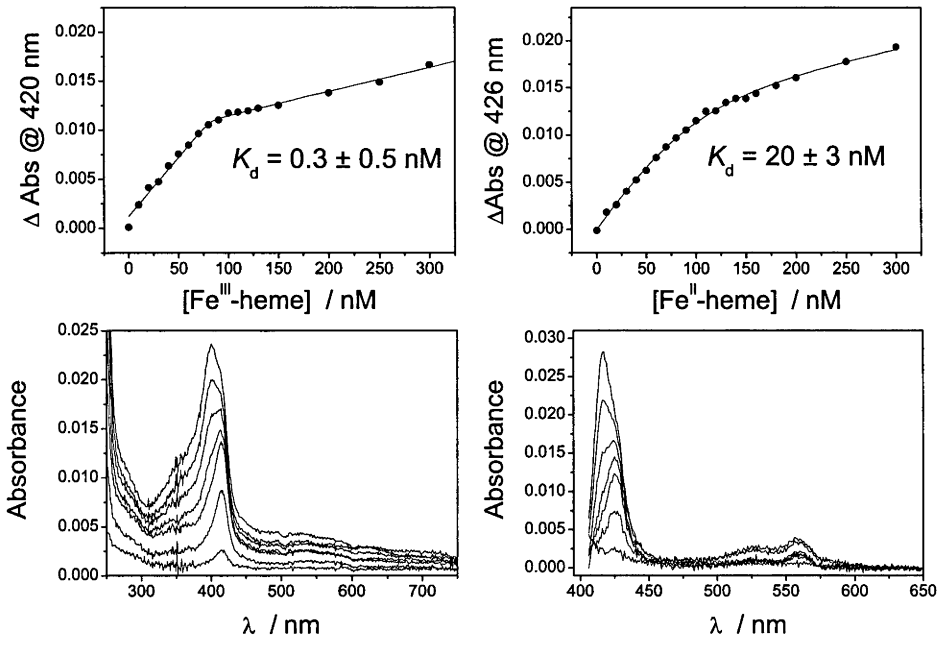

Figure 3.7: K_d determination in M7H. Fe(III)-heme (Left) and Fe(II)-heme (Right) titrations in apo-M7H. Top, the extent of binding as determined from bound Soret absorbance obtained from titrations shown below.

P_i

tions, requiring 100 mM KCl for maximal increase. This contrasts with the increase in the helicity of wt cyt to 82% upon Fe(III)-heme binding (Feng & Sligar, 1991). The $\theta_{222}/\theta_{208}$ ratios of the apo- and ferri-M7H mutant are 1.02 and 1.03 respectively, indicating these proteins have a coiled coil conformation (Zhou *et al.*, 1992), but this is less so than for the apo-H63N protein which has a $\theta_{222}/\theta_{208}$ ratio of 1.14. The Soret-region CD of ferri- and ferrous-M7H confirmed that despite only a small increase in helicity, the heme was bound to M7H in these experiments. These spectra are also shown in Figure 3.8 and are similar to those reported for wt cyt b_{562} (Bullock & Myer, 1978).

The far-UV CD spectra of apo- and holo-M7H (Fig. 3.8) suggests that upon Fe(III)-heme binding less structural rearrangement occurs than in the wt. The solution structure of apo-cyt b_{562} shows the C-terminal helix is largely unstructured (Arnesano *et al.*, 1999) and presumably in the wt, helix formation only occurs upon heme binding. Gel

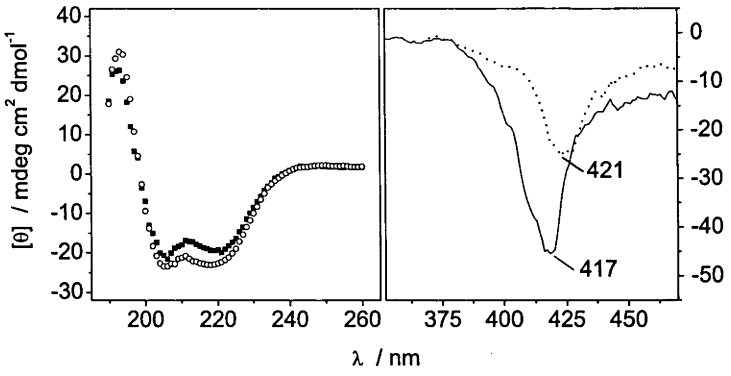

Figure 3.8: Circular dichroism spectra. Left, apo- (filled square) and Fe(III)-heme-reconstituted (open circles) M7H. Right, The Soret-region of oxidised (solid line) and reduced holo-M7H. The protein concentration was 5 μM (far UV) or 20 μM in 10 mM KP_i , 100 mM KCl, pH 7.0 at room temperature.

filtration chromatography shows that both apo- and holo-M7H has a larger hydrodynamic radius than H63N suggesting a more disordered fold. However, as for the wt protein, there is a decrease in the apparent size of M7H upon Fe(III)-heme binding which suggests that there is some conformational change. This may simply be due to the formation of the heme-His102 ligation which will anchor the C-terminal helix region of the protein. With the CD data, this suggests that there is little C-terminal helix formation in M7H upon heme binding which will result in a potentially more solvent-exposed porphyrin and a less stable protein.

Denaturation

The stability of the ferri-M7H and ferri-H63N proteins was investigated using guanidine denaturation at pH 7.0. The guanidine-induced unfolding of the ferricyts was monitored by loss of bound heme (data not shown). It has been shown that heme loss occurs concurrently with loss of secondary structure in wt cyt b_{562} (Feng & Sligar, 1991) and this was assumed to be the case for H63N and M7H. The energetics of the unfolding process were fit to a two-state linear denaturant binding model Pace (1986) with a ΔG^{H_2O} of 7.0 for ferri-wt cyt b_{562} (with N-terminus Met), 29 kJ mol^{-1} for ferri-H63N

Table 3.4: Thermal denaturation parameters

Protein	T_M (°C)	ΔH[1] (kJ mol^{-1})	ΔG[2] (kJ mol^{-1})
apo-M7H	54.3 ± 0.3	186 ± 21	15
ferrous-M7H	58.5 ± 0.3	236 ± 17	18
ferri-M7H	61.4 ± 0.3	55.2 ± 13	18
apo-wt[3]	54.04 ± 0.02	198 ± 212	16
holo-wt[3]	66.99 ± 0.15	436 ± 10	47

[1] The enthalpy of unfolding, ΔH, from this work was determined by the method described in (John & Weeks, 2000). [2] The free energy of unfolding, ΔG, was estimated using the Gibbs-Helmholtz equation (eqn 2.3) with ΔC_p= 2.3 kJ mol^{-1} K^{-1} for apo-proteins and ΔC_p= 3.8 kJ mol^{-1} K^{-1} for holo-proteins (Robinson *et al.*, 1998). [3]Additional data taken from Robinson *et al.* (1998) was measured by differential scanning calorimetry and are similar to those reported by (Feng & Sligar, 1991) as measured by loss of absorbance or CD.

and 75 kJ mol^{-1} for ferri-M7H. A ΔG^{H_2O} of 28 kJ mol^{-1} has previously been reported for the wt ferricyt denatured in urea by Feng & Sligar (1991) who also determined a ΔG^{H_2O} of 13 kJ mol^{-1} for the apo-cyt. The stabilisation of heme-binding to M7H was further investigated by thermal denaturation which is shown in Figure 3.9 for the apo-, ferrous- and ferri-M7H proteins. This is compared to data from similar experiments for the wt protein (Feng & Sligar, 1991; Robinson *et al.*, 1998) in Table 3.

Thermal denaturation of apo-M7H and apo-wt cyt b_{562} occur with a similar ΔG (Table 3.4) suggesting that the N-terminal methionine, H63N and M7H mutations do not significantly destabilise the apo-protein. There have been some differences in the reported chemical and thermal stabilities of holo-wt cyt b_{562} Feng & Sligar (1991); Robinson *et al.* (1998); Wittung-Stafshede *et al.* (1997). The calculation of ΔG from thermal denaturation data requires an accurate ΔC_pvalue and this may account for some of this disparity between values determined by thermal and chemical denaturation. The guanidine denaturation of ferri-wt and ferri-H63N yielded very similar ΔG

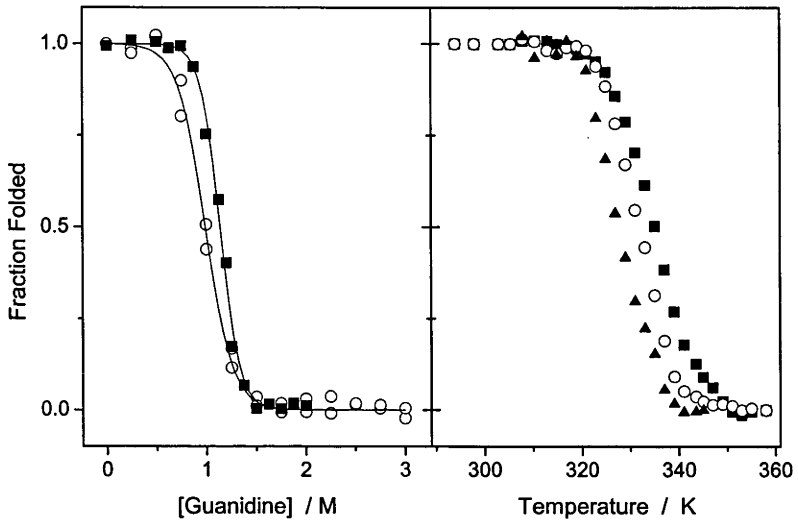

Figure 3.9: Denaturation of M7H. Left, Guanidine denaturation of ferri-H63N (squares) and ferri-M7H (circles) as measured by loss of bound heme Soret absorbance. Right, Thermal denaturation of apo-M7H (triangles), measured by second derivative UV absorbance, and ferrous- (open circles) and ferri-M7H measured by the loss of the bound heme Soret absorbance. All samples were in 50 mM KP_i, 100 mM KCl, pH 7. The thermodynamic parameters obtained are given in Table 3.4.

values (29 and 28 kJ mol^{-1}) further confirming the minimal impact the H63N mutation has had on the stability of the cyt. The stability of holo-M7H measured by both thermal and guanidine denaturation are in remarkably good agreement and show only a small ~4 kJ mol^{-1} stabilisation of the protein upon heme binding. The difference in chemical stability between holo- M7H and H63N was measured to be ~10 kJ mol^{-1} (ΔG(H63N) = 28 kJ mol^{-1}, ΔG(M7H) = 18 kJ mol^{-1}). It is reasonable to assume that this difference does not reflect the difference in bond strength between Met 7 S-Fe and His 7 N-Fe but rather that the M7H has disrupted hydrophobic contacts between the protein and the heme. The extent of the hydrophobic effect has been estimated to be ~9.9 kJ/nm^2 of water-excluded surface (Chothia, 1974). The surface area of one side of a porphyrin is ~1.0 nm^2 so the difference in stability of H63N and M7H could be explained by the heme in M7H having additionally one half of one side of the porphyrin

solvent exposed relative to H63N (if the side chains also become solvent exposed) and this could be achieved by the disruption of heme-contacts of only two or three side chains in the binding pocket. This is consistent with the model of M7H (Figure 3.5) and it seems that difference in stability between holo- H63N and holo-M7H is likely due to disruption of the residues either side of postion 7 and/or disruption of heme contacts in the C-terminal helix. Interestingly, M7A mutants of the wt protein have been created and these bind high-spin (5-coordinate) heme through His 102 with the ΔG^{H_2O} of the holo- and apo-protein very similar ($\Delta\Delta G \sim 2$ kJ mol^{-1}) (Kamiya *et al.*, 2001; Uno *et al.*, 2001). This suggests that once the methionine ligand in the wt protein is displaced then the His-bound heme offers little additional stability to the protein. It also appears that *bis*-His ligation of heme in M7H offers little additional stability to the protein relative to ligation by a single His.

The difference in stability of the oxidised and reduced holo-cyt is directly related to the difference in redox potential (ΔE_f) between the folded (Table 1) (E_F) and unfolded (E_U) protein (reviewed in (Mines *et al.*, 1996)). As an exposed heme in solution, i.e. E_f, has a midpoint of about -100 mV (Mines *et al.*, 1996; Bixler *et al.*, 1992), in the wt cyt b_{562} ΔE_f is $\sim$300 mV and thus, $\Delta\Delta G \sim 29$ kJ mol^{-1}. This difference in stability has been observed (Wittung-Stafshede *et al.*, 1997). The difference in the stability between ferri- and ferrous-M7H should be much smaller as $E_F \sim E_U$ and this was confirmed by thermal denaturation where no significant difference in ΔG between oxidised and reduced holo-M7H was observed.

Ferric and ferrous-heme binding to apo-M7H was measured to occur with $K_d$values of < 1 nM and 20 nM, respectively. Conversely, binding to apo-H63N occurred with $K_d$values of 13 nM and 3 nM for ferric and ferrous-heme, respectively. This reversal in affinity for ferric over ferrous heme binding to M7H is expected as in solution Fe(III)-porphyrins generally bind imidazoles and basic pyridines more tightly than Fe(II)-porphyrins ((Nesset *et al.*, 1996) and references within). These values are only estimates as it is possible that they were not measured at equilibrium due to ferric or ferrous-heme being kinetically trapped in either H63N or M7H in an analogous manner to that reported for cyt b_5 (Altuve *et al.*, 2001). Nevertheless, the M7H has altered the energetics of heme binding in a predictable fashion and to our knowledge this is the

first example of a comparison between the heme binding energetics in equivalent cyts with *bis*-His and His/Met ligation.

Both apo-H63N and apo-M7H can bind free-base protoporphyrin IX which implies that the heme binding pocket, i.e. those amino acids in the vicinity of the bound heme, is not seriously compromised by the M7H mutation and plays a role in heme binding. This suggests that the destabilisation of holo-M7H is due to subtle conformational changes that leave the binding pocket relatively intact. The experiments of Huffman *et al* (Huffman & Suslick, 2000) showed that the presence of non-coordinating hydrophobic residues flanking the heme-binding His can increase heme binding to a synthetic peptide by >20 kJ mol^{-1}. As the differences between the energetics of binding of heme or Fe(III)-heme to H63N or M7H are probably smaller than this (< 8 kJ mol^{-1}, Table 2), this also suggests that the heme binding pocket is not significantly altered in M7H. The Soret-region CD spectra (Figure 3.8) of ferri- and ferrous-M7H are qualitatively similar to those reported for wt cyt b_{562} (Bullock & Myer, 1978) and it is unlikely that this would be the case if the binding pocket in M7H was significantly altered.

EPR Measurements

The low-temperature X-band EPR spectra of ferri-H63N and ferri-M7H are shown in Figure 3.10. The features at g ~3 and g ~2.2 arise from low-spin heme. The sharp feature at g=5.9 is high-spin heme and accounts for less than 10% of the spins in the system. This resonance is possibly an artifact brought about by the denaturation of the proteins upon freezing whereby at least one of the heme ligands is displaced. The M7H spectrum shows a shoulder at g ~6.3 which becomes much more pronounced at pH 9 (data not shown). The low-spin resonances of wt cyt b_{562} H63N and M7H are listed in Table 3.5. The $g_{z,y}$, of wt and H63N are indistinguishable and are almost identical to those of M7H. The resonances are also similar to those of *bis*-imidazole-ligated Fe(III)-heme in solution (*bis*-Im-heme), which are also shown in Table 3.5. A precise g_x value for either cyt was difficult to determine due to the weak and broad nature of this feature so g_x values of 1.40 and 1.41 were calculated for H63N and M7H, respectively by the method of Walker *et al.* (1986) as described in the Chapter 2.

The H63N and M7H EPR data (Figure 3.10) are very similar and consitant with

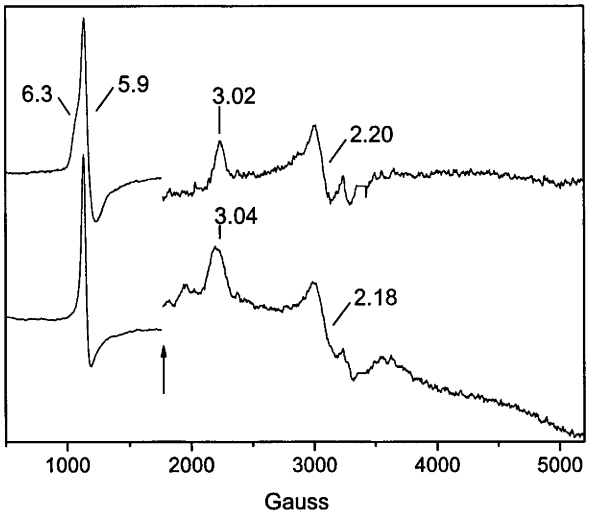

Figure 3.10: X-band EPR spectra at 10 K of ferri-M7H (top) and ferri-H63N. The portion of the spectra to the right of the arrow are magnified 5x. The proteins were at 100 μM concentration in 50 mM KP_i , 100 mM KCl, 20% glycerol, pH 7. Spectra were recorded at a microwave power of 2 mW and a modulation amplitude of 10 G. The g-values mentioned in the text are marked.

the Fe(III)-heme in a predominantly low-spin (LS) six-coordinate configuration. Both spectra show some high-spin (HS) signal at g ~5.9 which is probably due to freezing-induced dissociation of the heme from the cyt. However, the M7H spectrum has some broadening and splitting of the heme g ~5.9 resonance which becomes much more pronounced at pH 9 (not shown). This splitting has been attributed to the paramagnetic electron no longer having equal interaction with the four nitrogen atoms of the porphyrin (i.e. the porphyrin ring is no longer planar) and is observed in some high-spin globins and cyts (Peisach *et al.*, 1973). This would suggest that the HS heme is still bound to M7H and is non-planar. There is no evidence of HS M7H-bound Fe(III)-heme at room temperature, as there are no typical HS absorbance peaks, but it is interesting to speculate that the M7H mutation may place the bound heme under some steric strain and this could account for the split α absorbance band of ferrous-M7H. Using the measured LS g_z, g_y and calculated g_x tensors of H63N and M7H (Table 1), the rhombic

Table 3.5: EPR g tensors of hemin-reconstituted H23M42 and related peptides

Protein	g_z	g_y	g_x	V/λ	Δ/λ	V/Δ
wt b_{562} pH 6.9[a]	3.04	2.18	1.40[i]	1.60	3.39	0.47
wt b_{562} pH 10.5[a]	2.79	2.26	1.67	2.32	3.78	0.61
cyt *c* pH 7.4[b]	3.05	2.25	1.53	1.77	3.64	0.49
H63N	3.04	2.18	1.40[i]	1.60	3.37	0.47
M7H	3.02	2.20	1.41[i]	1.64	3.27	0.50
H23M42	2.86	2.26	1.6	2.11	3.59	0.59
H23H42	2.84	2.24	1.62[i]	2.16	3.82	0.56
bis-Im-Heme	3.02	2.24	1.51	1.77	3.54	0.50

The crystal field parameters V/λ, Δ/λ and V/Δ were calculated by the method of Taylor (1977) (Chapter 2). [i]These g_x values could not be assigned from the spectra and were calculated by the method of Walker *et al.* (1986) (Chapter 2). Additional data taken from (*a*) Moore *et al.* (1985), (*b*) from Gadsby *et al.* (1987) and (*c*) from Peisach *et al.* (1973).

and tetragonal splittings were calculated with V/λ = 1.60 and 1.64 and Δ/λ = 3.37 and 3.27, respectively. When these are plotted by the method of Peisach *et al.* (1973) as rhombicity (V/Δ) vs. tetragonal field (Δ/λ) they both fall within the H group of heme EPR spectra, which is assigned to ligation of the heme iron by two His imino-nitrogens. This is obviously not the case for H63N. Interestingly the M7H V/λ value of 1.64 is considerably less than $V = 2\lambda$ (which occurs when the two His imidazole groups are parallel to each other) suggesting that the orientation of the two ligating His imidazole planes are somewhat twisted relative to each other and is in agreement with the molecular model of Figure 3.5.

Redox Potentiometry

The redox properties of the Fe(III)-heme-reconstituted H63N and M7H mutants and also *bis*-Im-heme were examined by redox potentiometry and the redox titration curves are shown in Figure 3.11 A. The H63N mutation has no effect on the midpoint potential

but the conversion of the heme ligating methione to a His reduced the midpoint potential of the M7H cyt by 260 mV from +187 mV to -73 mV at pH 7.0. Despite this the E_{m7} of M7H is 70 mV more positive than that of *bis*-Im heme (-143 mV). Assuming that *bis*-Im-heme obeys a redox Bohr effect of -60 mV/pH unit (1 electron/1 proton) then the E_{m7} we have measured is in good agreement with the $E_{m8.5}$ of -235 mV measured for *bis*-Im-heme previously Shifman *et al.* (2000).

The pH dependence of the M7H midpoint potential was examined and the data are shown in Figure 3.11 B. Similar data for the wt protein taken from reference Moore *et al.* (1985) are also shown for comparison. The M7H data are fit to the following equation:

$$E = E_{low} + 59\log\frac{[H^+] + K_{red}}{[H^+] + K_{ox}} \tag{3.3}$$

where pK_{red} and pK_{ox} describe a protonation event when the heme is reduced and oxidised, respectively and E_{low} is the E_m at pH $\ll pK_{ox}$ (Clarke, 1960). The data were fit to pK_{red} = 6.8 and $pK_{ox} \ll 5$ (where the protein heme complex is not sufficiently stable to measure the E_m).

It has been experimentally shown that heme bound through His/Met ligation has a midpoint potential ~150 mV more positive than its *bis*-His equivalent (Harbury & Loach, 1960). This difference is due to the greater electron withdrawing ability of the Met sulfur, which destabilises the positively charged oxidised heme. This effect is exemplified in the *c*-type cyts where the redox potentials of His/Met and *bis*-His ligated heme range between 0 to +400 and -400 to -100 mV, respectively (reviewed in Moore & Pettigrew (1990)). In addition this effect is additive as H102M mutants of cyt b_{562}, which bind heme through *bis*-Met ligation, have midpoint potentials about 180-200 mV higher than the wt cyt (Barker *et al.*, 1996). The ΔE_{m7} of M7H vs. H63N (Figure 3.11 A, Table 1) is 260 mV, ~100 mV greater than the 150 mV predicted Harbury & Loach (1960). rCDH, the only other known *b*-type cyt with His/Met ligation, has an $E_{m4.5}$ of +164 mV, while the *bis*-His mutant of this protein has an $E_{m4.5}$ of -53 mV (Rotsaert *et al.*, 2003). This ΔE_m of 217 mV is more similar to that observed for wt and M7H cyt b_{562} than that suggested by model compounds (Harbury & Loach, 1960). The *bis*-His mutant of rCDH has unusual ligation through His imidazole $N^{\delta 1}$ and $N^{\epsilon 2}$ nitrogens. This form of ligation is very rare but is observed in one of the four hemes of cyt c_{554}

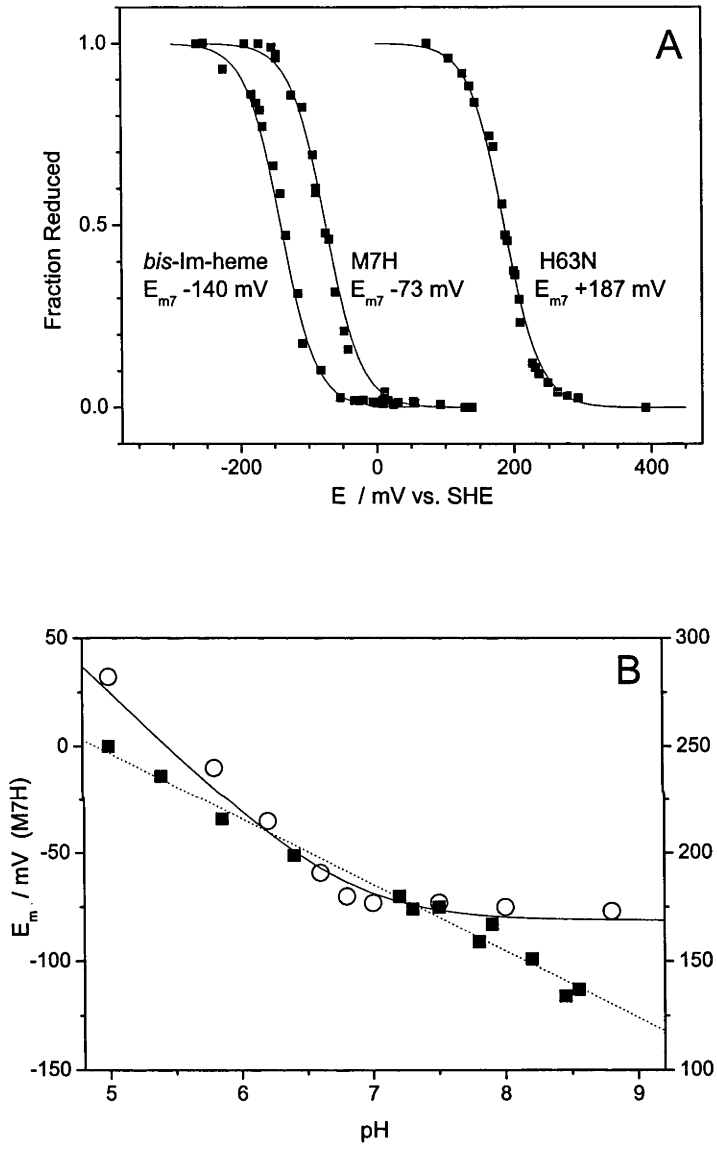

Figure 3.11: (A) Redox titration curves for *bis*-imidazole heme, and the Fe(III)-heme-reconstituted cyt b_{562} mutants M7H and H63N at pH 7.0. The fraction of reduced heme was determined by the change in absorbance of the α band at ~560 nm. The data are fit to a single Nernst curve with n = 1.0 and the midpoint potentials are given in Table 3.2. (B) The pH dependence of the midpoint potential of M7H (open circles) fit to equation 3.3 with pK_{red} = 6.8 ± 0.1 and pK_{ox} fixed at 0. The filled squares are data for the wt taken from reference Moore *et al.* (1985) and are fit to a line with a slope of -30 mV/pH unit.

from *Nitrosomonas europaea*. This heme has been assigned an unusually high (for *bis*-hisitidine ligation) midpoint potential of +47 mV (Upadhyay *et al.*, 2003) and it seems that N^{ϵ}/N^{δ}-ligated heme can have a higher midpoint potential than an equivalent $N^{\epsilon}/N^{\epsilon}$-ligated heme (see (Upadhyay *et al.*, 2003) for a discussion of this). While this type of ligation can not be ruled out in M7H there are other explanations as to why there is such a large difference in midpoint potentials between H63N and M7H. One explanation for this is consistent with the observation that the M7H mutation leaves the bound heme more solvent exposed than in the wt. It has been experimentally shown using synthetic heme-binding peptides that the protein hydrophobicity can exert $\pm$ $\sim$50 mV effect on the heme redox potential (Gibney *et al.*, 2001) but this presumably accounts for at least some of the 70 mV difference between the E_{m7} of *bis*-imidazole and M7H-ligated heme. The difference in K_{d}values for ferric and ferrous heme-binding to H63N and M7H (Table 2) will play a role in the difference in midpoint potentials (ΔE_{m}) between these two cyts. The stability of ferric over ferrous heme binding in M7H stabilises the oxidised state by at least $\sim$7 kJ mol^{-1} or 75 mV (see (Kennedy *et al.*, 2001) for a complete description of this effect). Similarly, the difference in binding energetics in H63N also contributes to this and ΔE becomes $\sim$110 mV between M7H and H63N due to this preferential binding. The magnitude of this effect can account for the unexplained difference between the ΔE_{m} of H63N and M7H but it should be stated that some of the 150 mV difference between the ΔE_{m} of His/Met and *bis*-His ligated heme observed by Harbury & Loach (1960) can probably also be explained by this argument. A range of midpoint potentials spanning >160 mV was observed in a library of *in vitro*-evolved cyt b_{562} variants (Springs *et al.*, 2000, 2002). In two generations of mutants, which all maintained His/Met heme ligation, only one mutant displayed a midpoint potential more positive than the wt protein. This led the authors to suggest that cyt b_{562} has evolved to have a midpoint potential at the positive extreme allowed by the protein's architecture and almost any alteration to the protein will lower this potential. Thus, the M7H mutation, which has a potential in the upper range of *bis*-His ligated cyts, is expected to disrupt some of the mechanisms cyt b_{562} has perfected to produce the most positive midpoint potential the protein architecture will allow. This will result in lowering of the midpoint of M7H through protein-porphyrin interactions

in addition to those manifested through the axial ligands.

The pH dependence of the midpoint potential of M7H is dominated by a single ionisation in the reduced state (Figure 3.11 B). A pK of 6.8 has previously been assigned to a heme propionate in wt cyt b_{562} by using NMR chemical shifts (Moore *et al.*, 1985) and this propionate is most likely the ionisable group responsible for the pK_{red}. The pH dependence of the wt E_m is unusual with an approximately linear dependence with a slope of ~30 mV per pH unit. The pH dependence from pH 5.0 to pH 8.5 has been described as arising from at least 5 single proton ionisations including both heme propionates (Moore *et al.*, 1985). Direct electrochemistry of cyt b_{562} gave similar results Barker *et al.* (1996) and the authors fit their data to two pK_{red} and two pK_{ox}. The data set for M7H does not contain enough data points to reliably exclude other pK_{red} and pK_{ox} events but the dominance of the single propionate on the measured E_m is evident. One of the ionisable groups in the wt cyt b_{562} is probably neutral His102 which appears to get deprotonated at an unusually low pH (pKa ~9) due to the stabilisation of the histidinate anion by argines 98 and 106 (Moore *et al.*, 1985). This appears to be disrupted in M7H where presumbably this stabilisation is lost and the pKa of His102 becomes > 9. This is consistent with structural pertubation of the C-terminal helix as previously suggested but could also be achieved through a relatively small twist of the plane of the imidazole of His102 which is consistent with EPR. Interestingly the *bis*-Met mutants of cyt b_{562} have a qualitatively similar E_m pH dependence as the wt protein described by two each pK_{red} and pK_{ox} events (Barker *et al.*, 1996). These mutants were generated by replacing the His at position 102 and indicate that other ionisable groups play a significant role in the unusual pH behaviour of the redox properties of the wt cyt b_{562}.

Many of these arguments could be resolved by knowledge of the structure of the M7H cyt so we are currently attempting to crystalise this protein for X-ray diffraction. We have generated small crystals thus far which, although are too small for measurements, give us hope that the protein is reasonably well structured and has a dominant conformer. The M7H mutant cyt is a small, soluble, single-heme-binding protein. With *bis*-His ligation the protein becomes a good minimalistic example of a typical *b*-type cyt.

H23M42

Although His/Met-ligated heme has been reported in a member of a library of randomly-designed four-helix bundle peptides (Rojas *et al.*, 1997) we are not aware of any reports of a rationally-designed peptide with a His/Met heme-ligation site. The H23H42 peptide was mutated at postion 42 (His to Met) creating H23M42. Heme binding to the H23M42 peptide is discussed below.

Heme Absorbance

The absorption spectra of oxidised and reduced [H23M42-heme]$_2$ are both typical of low-spin heme (data not shown, peak positions given in Table 3.2). The titration of Fe(III)-heme into H23M42 yields a binding stoichiometry very similar to that obtained when Zn-protoporphyrin IX (ZnPP) is titrated. Dutton and coworkers have shown that for the similar peptide α-*l*-α, a maximum of one ZnPP can bind per *bis*-His heme-binding site (although ZnPP forms only 1 axial ligand) (Sharp *et al.*, 1998*a*) due presumably to the prohibitive steric hindrance of two ZnPP binding in such close proximity. This lends evidence to the binding of heme to H23M42 through His/Met ligation rather than between peptide monomers in a *bis*-His fashion (which in α-*l*-α has a K_d value of 23 μM (Sharp *et al.*, 1998*a*)).

Strong evidence for His/Met ligation is the "695 nm" Met (S)→Fe(III) CT band mentioned earlier for cyt b_{562} (Section 3.2). A CT band was observed in Fe(III)-heme-bound H23M42 at 700 nm (Figure 3.12). The absorption coefficient of this band is about 300 $M^{-1}cm^{-1}$, similar to that of cyt b_{562} (Moore *et al.*, 1985). The band is lost at high pH and when the heme is reduced. This is fairly good evidence for His/Met ligation of heme in H23M42 and the absorbance spectrum of this CT band is shown in Figure 3.12. The difference spectra between the complex at pH 7 and pH 11 is shown to better visualise the peak's weak absorbance. In cyt*c*, the Met ligand to heme is displaced at alkaline pH and is thought to be replaced by one of several surface-exposed lysines. This alkaline transition has been investigated in many mutants of the protein and the midpoints for this transition all fall between about pH 8.5 and 9.5 (Caffrey & Cusanovich, 1994). A similar alkaline transition also occurs in cyt b_{562} where the Met

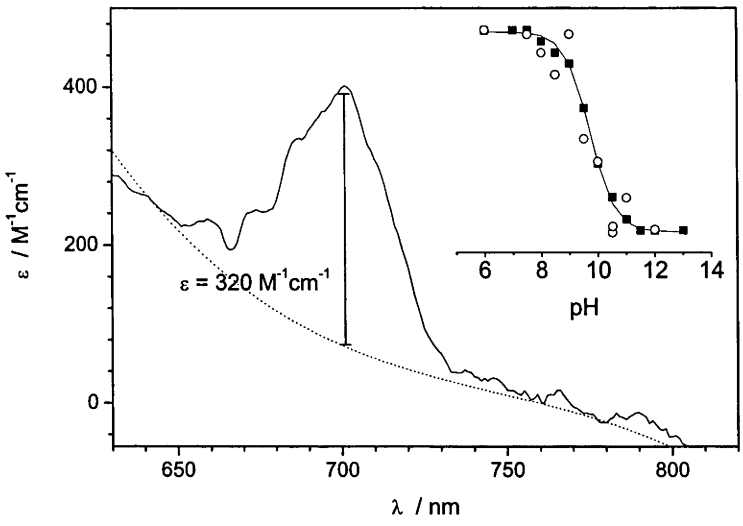

Figure 3.12: Difference absorbance spectra (pH 7.0 minus pH 11.0) of $[H23M42]_2$-Fe(III)-heme showing the putative Met S→ Fe(III) CT band. The inset shows the relative loss of Soret absorbance (solid squares) and CT band absorbance (open circles) as a function of increasing pH.

ligand is not displaced but rather the His ligand loses a proton (mentioned earlier) and the Met S → Fe(III) CT band shifts from 720 nm to 680 nm (Moore *et al.*, 1985). The alkaline transition of $[H23M42\text{-heme}]_2$ is shown in the inset to Figure 3.12 where the loss of the CT band absorbance at 700 nm is plotted. This loss of CT absorbance occurs with a pK of 9.5 ± 0.5, which is consistent with cyt*c* values. There is a concomitant blue-shift of the Soret position and decrease in absorbance (also plotted in the inset to Figure 3.12) with a pK of 9.7 ± 0.1. The Soret blue-shift is consistent with the displacement of the Met ligand and while the His ligand may also be displaced the process is completely reversible and does not appear to involve protein denaturation. In addition there is no change in the Soret position of reduced $[H23M42\text{-heme}]_2$ over the pH range 5-13. The secondary structure of a peptide of similar design was shown to be stable over this pH range where there was no significant change in peptide α-helicity between pH 1-12 (Shifman *et al.*, 1998).

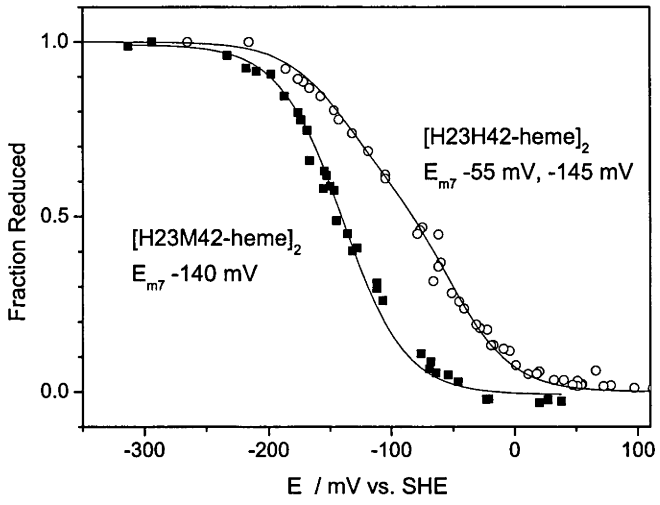

Figure 3.13: Redox titrations of $[H23H42\text{-heme}]_2$ and $[H23M42\text{-heme}]_2$.

EPR

The low temperature EPR spectra of Fe(III)-bound H34M42 and H23H42 was measured (data not shown) and the g tensors are given in Table 3.5. Both spectra are indicative of low-spin iron ligated by strong axial ligands and are similar to those of other His/Met-ligated heme proteins (Moore & Pettigrew, 1990; Moore *et al.*, 1985) and *bis*-His ligated heme. It has been noted that EPR is unable to identify the mode of ligation in cyts (Moore *et al.*, 1985) and this is the case here. The only real trend is that the *de novo* peptides have more similar EPR spectra to each other than to the cyt b_{562} mutants.

CD and Chromatography

H23H42 is expected to dimerise in the *syn* topology (Sharp *et al.*, 1998*b*) with the peptide monomers orientated such that the two glycine loops are adjacent. This will place the two bound heme molecules in quite close proximity. The H23H42 and H23M42 peptides were shown by far-UV CD to fold correctly, forming a similar degree of α-helical secondary structure (data not shown, see Razeghifard & Wydrzynski (2003) for a spectrum of H23H42). Both peptides were shown to dimerise correctly by size-

exclusion chromatography (data not shown) both eluting with an apparent mass of 17 kDa, consistent with a well-ordered dimer. The heme-bound complexes eluted as dimers with a similar elution time.

Heme Redox

Redox potentiometry of [H23M42-heme]$_2$ and [H23H42-heme]$_2$was performed and the data are shown in Figure 3.13. The potentiometric curve for H23H42 is similar to reports for similar maquettes (Sharp *et al.*, 1998*b*) if the data are corrected for a redox Bohr effect of -60 mV per pH unit. The E_m values are given in Table 3.2. In the H23H42-heme complex there are two separate E_{m7} values split by 90 mV, which is consistent with heme-heme electrochemical anti-cooperativity, which is seem in other multi-heme maquettes in the *syn* topology (Robertson *et al.*, 1994; Sharp *et al.*, 1998*b*). This anti-coperativity is thought to be caused by the electrostatic repulsion of the positively charged oxidised heme molecules (Robertson *et al.*, 1994; Leitch *et al.*, 1985), which destabilises the oxidised heme and subsequently elevate the heme midpoint potential. Once one heme becomes reduced the second heme reduction occurs at a similar E_m as a non-cooperating heme due to the elimination of this electrostatic repulsion. There is no splitting in the potentiometric curve of [H23M42-heme]$_2$ (Figure 3.13. This could be explained by several ways. There may only be one heme bound per 4-helix bundle. This is inconsistent with the ZnPP titration mentioned earlier but not ruled out. Another explanation is that the peptide is not dimerised (inconsistent with chromatography discussed above), or is dimerised in an *anti* conformation (c.f. *syn*) thus alleviating the electrostatic influence of the nearby heme. The E_m for the His/Met complex is unusually low for a His/Met-ligated heme (discussed above in Section 3.2 and much more consistent with a *bis*-His ligated heme. It is possible for the H23M42 peptide to ligate a single heme (per 4-helix bundle) by intra-monomer *bis*-His ligation. This has been demonstrated in a similar peptide with a His/Ala ligation motif with a K_d of 23 μM (Sharp *et al.*, 1998*a*). This mode of ligation is not consistent with the measured Fe(III)-heme K_d values (Table 3.3), nor with the observed CT band at 700 nm.

Detailed structural data, or perhaps NIR-CD and resonance Raman, are required to

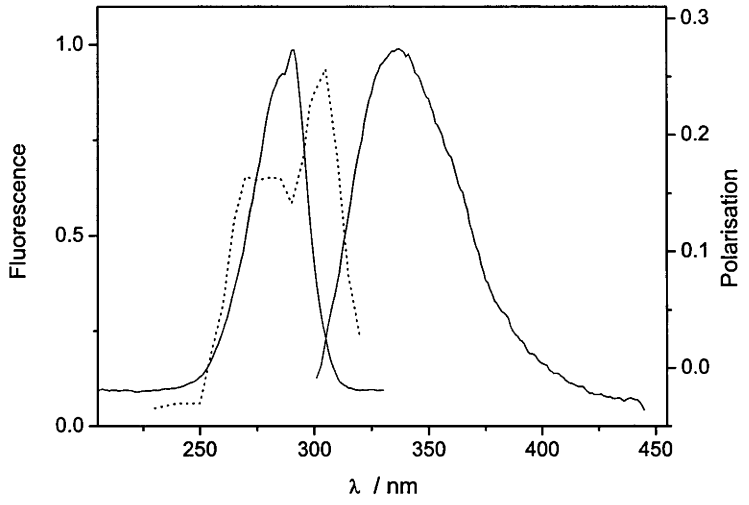

Figure 3.14: Fluorescence excitation and emission spectra (solid line) and polarisation excitation spectrum (dotted line, $\lambda_{emission}$ = 340 nm) of the *de novo*-designed peptide H23H42.

unequivocally determine the mode of heme ligation in H23M42. This remains to be done, and for the moment this question will remain un-resolved.

Tryptophan Fluorescence

The *de novo*-designed peptides all contain a single Trp at position 26 on the N-terminal helix. The fluorescence excitation, emission and polarisation excitation spectra of the Trp in H23H42 are shown in Figure 3.14. The emission spectrum, with a maximum at ~340 nm, is classed as a type II Trp fluorescence spectrum, which are characteristic of a solvent-exposed but relatively imobile Trp (Ladokhin, 2000). In the presence of high-concentration of guanidine the emission maxima shift only slightly to ~350 nm with little change in intensity (data not shown) suggesting the Trp is solvent-exposed in the native peptide but becomes more mobile upon denaturation of the peptide.

In these peptides the Trp is one helical turn from His 23, a heme ligand. Upon the addition of porphyrins such as Fe(III)-heme the Trp fluorescence is dramatically quenched. There is a considerable spectral overlap between the Trp emission and

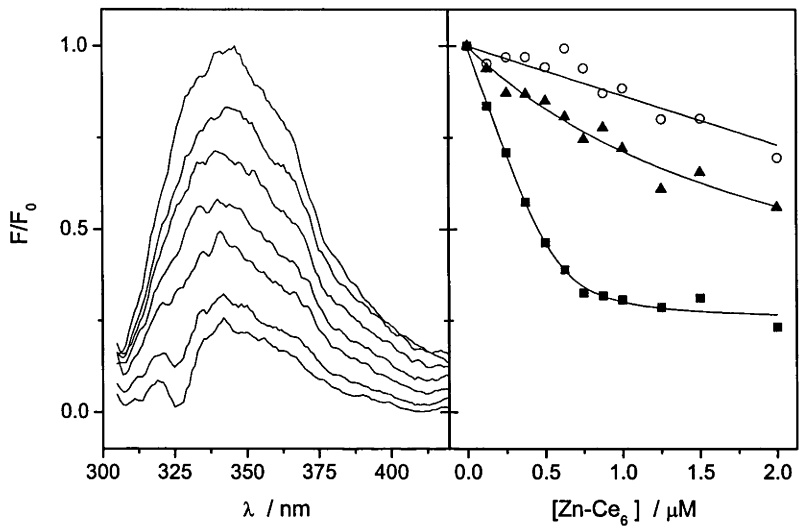

Figure 3.15: Binding of Zn-Ce_6 to *de novo* peptides measured by Trp quenching. Left, Trpytophan fluorescence in H23H42 in the presence of 0, 0.5, 1, 0.5, 2.0, 4.0 and 8.0 Zn-Ce_6 per monomeric peptide. Right, Titration of Zn-Ce_6 into H23H42, pH 7.0 (squares); H23H42, pH 5.5, (circles); and F23F42 (triangles).

Fe(III)-heme absorbance and this quenching is thought to occur through a Förster mechanism (see Chapter 1.4). This quenching was used to characterise the initial binding of Fe(III)-heme to H23H42 (data not shown, see Figure 3.15 for a similar experiment). The K_d (54 $\pm$ 7 nM) is in reasonable agreement with the value of 35 nM determined by Sharp (1998) (obtained using absorbance analogous to Figure 3.7). Thus, this method offers an alternative and reasonably accurate method of measuring porphyrin binding to these *de novo* peptides.

3.3 Chlorin-Binding

The *de novo*-Designed Peptides

Trp quenching was used to characterise the binding of porphyrin and chlorin molecules to several *de novo* peptides. The titration of Zn-Ce_6 into H23H42 at pH 7.0 and 5.5, and into F23F42 is shown in Figure 3.15. There is only significant quenching with the

H23H42 peptide at pH 7.0. At pH 5.5 the His ligands are protonated (pK_a His ~6.0) and thus unable to ligate Zn-Ce_6. Likewise, in F23F42 the His ligands have been replaced with non-ligating phenylalanines. Thus, Zn-Ce_6 binding to these peptides requires a His residue under conditions where the His is not protonated. The data in Figure 3.15 can be fit to eqn 3.4 which is a modified form of eqn 2.1:

$$F = F_{max} - Q[([E_0] + [L] + K_d) - \sqrt{([E_0] + [L] + K_d)^2 - 4([E_0][L])}]/2, \qquad (3.4)$$

where F_{max} is the Trp fluorescence in the absence of quencher (L), and Q is a constant which describes the efficiency of quenching by a particular ligand. E_0 and K_d are standard. The K_d values obtained by this method are given in Table 3.6. Trp quenching was prefereable to absorbance titrations for monitoring the binding of Zn-Ce_6 and the chorophylls to these *de novo* peptides as the absorbance changes of the chlorins upon ligation by the protein are quite subtle (Section 3.1 and Razeghifard & Wydrzynski (2003)). Additionally the fluorescence technique offers potentially greater sensitivity which allowed the use of lower concentrations of both peptide and chlorin. This is advantageous as the porphyrins, chlorins and particular the chorophylls have a tendency to aggregate in aqueous solutions and this aggregation is concentration-dependent (see for example (Margalit *et al.*, 1983; Scheer, 1991)).

The binding stoichiometries obtained from the quenching data are consistent with our previous report for Zn-Ce_6 binding to these peptides (Razeghifard & Wydrzynski, 2003). Whilst the peptides only bind one heme per monomer, two Zn-Ce_6 molecules will bind, one per His. Chl *b* was shown to bind to H23H42. There was no binding detected to F23F42 suggesting that this binding involved His ligation. in contrast to Zn-Ce_6, only one Chl *b* bound per peptide monomer. This may be due to steric reasons, with the Chl's phytyl tail preventing the binding of a second Chl. The K_d was an order of magnitude weaker than that of Zn-Ce_6 and thus, the binding of a second Chl *b* may occur at $K_d \gg 1$ μM. It becomes problematic working with the Chls in aqueous solution at the concentrations required to confirm this. The K_d values for the binding of the Zn-Ce_6 were determined by absorbance to be about 0.3 and 1 μM (Razeghifard & Wydrzynski, 2003). This is consistent with results obtained by Trp quenching at peptide concentrations of 5 μM dimer. At lower concentrations there was some disagreement

Table 3.6: Porphyrin and chlorin binding to monomeric[a] *de novo* peptides

Protein Porphyrin	K_d[b] (nM)	ΔG (kJ mol^{-1})	n[c]
H23H42			
Fe(III)-heme	54 ± 7	40.7 ± 0.3	1
Zn-Ce_6	34 ± 16	42 ± 2	2
Zn-$Ce_6$6*d*	1,200 ± 200	33 ± 1	2
Chl *b*	540 ± 210	35 ± 1	1
H23M42			
Fe(III)-heme	120 ± 40	39 ± 3	1
H23H42 pH 5.5			
Zn-Ce_6	<4000	-	<1
F23F42			
Zn-Ce_6	nd	-	<1

[a]The peptide concentration was 250 nM where it is predominantly monomeric (see Table 3.7 and the text); [b]K_d was determined by a fit of eqn 3.4 to Trp quenching data (Figure 3.15); [c]Ratio of porphyrin or chlorin binding per monomeric peptide. This experiment was performed at 5 μM $[H23H42]_2$ concentration.

in K_d values and this proved to be due to concentration-dependent dissociation of the peptide dimer.

Peptide Dimerisation

There is a relationship between polarisation, fluorescence lifetime and rotational diffusion (reviewed by Jameson & Seifried (1999)). The Perrin-Webber equation states:

$$\left(\frac{1}{P_i} - \frac{1}{3}\right) = \left(\frac{1}{P_0} - \frac{1}{3}\right)\left(1 + \frac{3\tau}{\rho}\right), \tag{3.5}$$

where P_i is the observed polarisation, P_0 is the intrinsic polarisation[4], τ is the excited state lifetime and ρ is the Debye rotational relaxation time[5] which for a 17 kDa peptide dimer is ~20 ns. If we assume the Trp has a lifetime of 3 ns (a reasonable assumption for a solvent-exposed Trp), and we use a P_0 of 0.3, using eqn 3.5 we find that the polarisation of the dimeric H23H42 peptide should be about 0.2. This is in good agreement with observation (see Figure 3.14). This polarisation will decrease upon dissociation of the dimerised peptide into monomers. To determine if it is feasible to measure this difference, guanidine denaturation of $[H23M42]_2$ was measured by loss of Trp fluorescence polarisation (data not shown). At very high guanidine concentration a loss of polarisation from ~0.2 to < 0.05 was observed corresponding to a $[Gdn]_{1/2}$ of 5.7 M. This is similar to previous reports for these maquettes obtained by following the loss of secondary structure by CD (Gibney *et al.*, 1997; Gibney & Dutton, 1999) and tertiary structure (Gibney *et al.*, 1997). From a fit[6] to the data a ΔG^{H_2O} of 28 ± 5 kJ mol^{-1} and an m value of 4.0 ± 1 kJ mol^{-1} M $^{-1}$ was obtained. These values are considerably lower than those obtained by Gibney *et al.* (1997) following the loss of native structure, and secondary structure (Gibney *et al.*, 1997, 1998). This may be due to this method only monitoring dissociation and not loss of α-helicity and demonstrates the possibility

[4]The intrinsic polarisation, P_0, is the polarisation in the absence of depolarisation influences such as rotation and energy transfer. This is determined by:

$$\left(\frac{1}{P_0} - \frac{1}{3}\right) = \frac{5}{3}\left(\frac{2}{3\cos^2\theta - 1}\right), \tag{3.6}$$

where θ is the angle between the absorption and emission oscillator.

[5]The Debye rotational relaxation time is the harmonic mean of the relaxation times about the 3 axis of rotation. This was simplified by Perrin for the case of spherical molecules where:

$$\rho = \frac{3\nu M(v + h)}{RT}, \tag{3.7}$$

where ν is the solvent viscosity (0.01 in the case of water), M is the mass of the peptide (in Da), v is the partial specific volume of the peptide (we will use 0.74 mg mL^{-1}), h is the degree of hydration (we will use 0.2 mg g^{-1}), and R = 8.314 x 10^7 erg mol^{-1}K^{-1}. These values are taken from Jameson & Seifried (1999)

[6]The denaturation data was fit to a dimer folded to monomer unfolded model:

$$\text{fraction dimer} = 1 - (K_{unf}/4P_T)[\sqrt{(1 + 8P_T/K_{unf})} - 1], \tag{3.8}$$

where $k_{unf} = \exp(-\Delta G_{unf}/RT)$ and $\Delta G_{unf} = \Delta G^{H_2O} + m[Gdn]$.

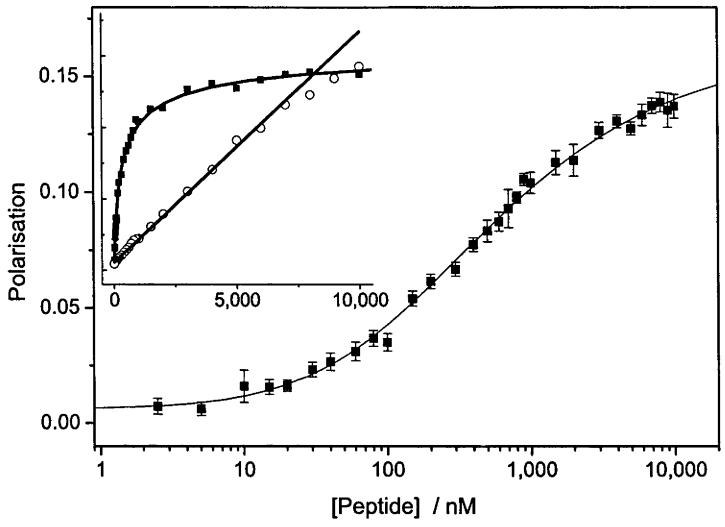

Figure 3.16: Concentration-dependent change in polarisation of H23M42 as a measure of the K_d of dimerisation. The inset shows the polarsation (squares) and emission intensity (open circles).

of using this Trp fluorescence to probe the dimerisation state of the peptide

The *de novo* peptides will be in a monomer/dimer equilibrium:

$$2M \rightleftharpoons D, \quad k_d = \frac{[M]^2}{D}, \tag{3.9}$$

where M and D are the monomeric and dimeric peptide, respectively, and the total peptide concentration, P_T, = [M] + 1/2[D]. This was measured for several peptides and Fe(III)- and Zn-Ce_6-bound to H23H42 by diluting the peptides or complexes whilst measuring the Trp polarisation. This is shown for H23M42 in Figure 3.16. The data fits the model (eqn 3.9) well suggesting that if the monomer unfolds, it does so after dissociation. It made no difference if this experiment was performed in reverse, by increasing the peptide concentration. The energy of dissociation (ΔG_d) value for H23H42 is in agreement with the ΔG^{H_2O} value obtained by denaturation of H23H23 (discussed above) confirming the utility of these measurements. The K_d values are given in Table 3.7.

The dimerisation of similar peptide maquettes have been analysed by gel permeation chromatography and the peptides are reported to be dimeric over the concentra-

Table 3.7: Energetics of dimerisation of the *de novo* peptides

Protein	v (μM)	ΔG_d (kJ mol^{-1})	$\Delta\Delta G_d$ (kJ mol^{-1})
H23H42	1.5 ± 0.3	32.7 ± 0.5	0
H23F42	1.0 ± 0.3	33.7 ± 0.9	
H23M42	1.00 ± 0.07	33.7 ± 0.2	
H23H42-heme	1.9 ± 0.7	32 ± 1	0.7
H23H42-Zn-Ce$_6$	3.7 ± 0.7	30.5 ± 0.5	2.2
H23H42-Zn-Ce$_{62}$	4.5 ± 1.0	30.0 ± 0.6	2.7
H23H42[a]	-	28 ± 5	

[a]Disruption of dimeric H23H42 by guanidine. The ΔG and error values were obtained from a fit to eqn 3.8. The K_d values were obtained from $\Delta G_d = -RTlnK_\mathrm{d}$.

tion range 0.1 - 100 μM (Gibney & Dutton, 1999). The values in Table 3.7 suggest that the peptides used here dimerise with a K_d of about 1 μM. The peptides characterised by Gibney & Dutton (1999) are of a slightly different design, consiting of single helices covalently linked to form dimers, which then dimerise. The differences in the loop regions between these peptides and those used in this work may account for the differing K_d values.

The majority of Trp quenching titrations presented in Table 3.4 were performed with a monomeric peptide concentration of 200-500 nM. In this regime the peptide is predominantly monomeric (as suggested by the polarisation data) and this explains why the K_d values of Zn-Ce$_6$ binding were peptide-concentration specific. As the K_d of Zn-Ce$_6$ and Fe(III)-heme binding to monomeric H23H42 is $\sim$50 nM, these porphyrins remain bound during the course of the dilution experiment. The monomeric peptide is expected to retain its secondary structure (Gibney *et al.*, 1997). Despite this, heme and Zn-Ce$_6$ binding only destabilises the H23H42 peptide complex by about 1 and 2-3 kJ mol^{-1}, respectively (Table 3.7).

Despite the fact that two Zn-Ce$_6$ molecules bind per H23H42 monomer, under both conditions of monomeric and dimeric peptide there is no evidence that these Zn-Ce$_6$

molecules are excitonically coupled: (*i*) The chlorin absorbance is identical to that of the monomeric species, and (*ii*) There is no shift in the chlorin fluorescence emission nor any fluorescence depolarisation upon the binding of the second equivalent of Zn-Ce_6 per peptide monomer. Additionally, the width of the Zn-Ce_6 cation radical does not change when bound singularly or doubly to $H23H42_2$ (data not shown). The redox potentiometry of [H23H42-heme]$_2$ shows considerable heme-heme electrostatic interactions (discussed above, Figure 3.13) but these interacting heme molecules are expected to be separated by about 15-20 Å, which is probably too far apart to expect excitonic coupling. Then what is the structure of the [H23H42-Zn-Ce_{62}]$_2$ complex? As there is no evidence that the four bound chlorin molecules are within 10 Å of each other, it seems likely that they are facially bound on the surface of the peptide. The absorbance spectrum of this complex (shown in (Razeghifard & Wydrzynski, 2003)) is fairly similar to that of the Zn-Ce_6 imidazole complex (Figure 3.17) which supports this argument. Zn-Ce_6 has three carboxylate groups (Figure 3.1) which makes it potentially more soluble than either heme or ZnPP and thus more likely to bind to a fairly solvent-exposed position on H23H42.

To summarise, the *de novo*-designed peptide [H23H42] binds heme, ZnPP, Zn-Ce_6, and Chl *b*. This binding involves His ligation and the peptide is able to bind 1 heme, ZnPP, or Chl *b* per monomer, or 2 Zn-Ce_6 per monomer. In the [H23H42-Zn-Ce_{62}]$_2$ complex, the bound heme are electrochemically coupled but there is no evidence for excitonic coupling in any of the porphyrin-peptide complexes despite the close proximity of Zn-Ce_6 in [H23H42-Zn-Ce_{62}]$_2$. This leads to some uncertainty in the relative position of the bound Zn-Ce_6 molecules. As an alternative, chlorin binding was explored in cyt b_{562}.

Chlorin Binding to Cytochrome b_{562}

The apo-H63N protein can be reconstituted with the light-active Chl analogue Zn-Ce_6 and with ZnPP. These porphyrins are ligated by a single His (Figure 3.2) and in the H63N protein the only remaining His is at postion 102. This is one of the heme ligands within the binding pocket of the cyt. The binding of Zn-Ce_6 to apo-H63N occurs with a K_d of ~25 nM at a stoichiometry of 1:1. The absorbance spectrum of H63N-bound Zn-

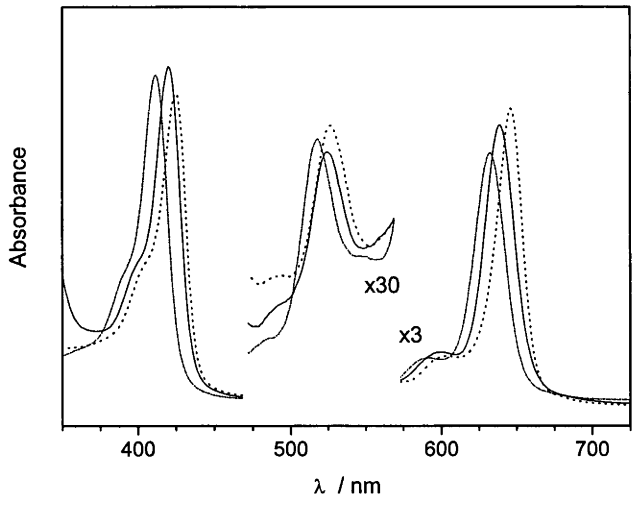

Figure 3.17: Absorbance spectra of Zn-Ce_6 in solution (dashed line), ligated with imidazole (solid line) and bound to cyt b_{562} (dotted line). All samples were in 50 mM KP_i, 100 mM KCl, pH 7.0.

Ce_6 is shown in Figure 3.17. The Zn-Ce_6-H63N spectrum is red-shifted relative to both Zn-Ce_6 in solution and the imidazole complex of Zn-Ce_6. The Zn-Ce_6-H63N spectrum is red-shifted relative to Zn-Ce_6-H23H42 also (data not shown, see Table 3.8). The additional red-shifting to that caused by imidazole (His)-ligation is probably caused by the lower dielectric of the heme binding pocket relative to the solvent. This suggests not only that the Zn-Ce_6 is bound within the cyt b_{562} heme binding pocket, but also that the H23H42-bound Zn-Ce_6 is relatively more solvent exposed.

Despite the M7H protein having two His residues within the heme binding site only a single ZnPP and Zn-Ce_6 molecule bound per M7H. The absorbance and fluorescence of M7H-bound Zn-$Ce_6$and ZnPP were almost identical to their H63N-bound counterparts. The M7H-bound Zn-Ce_6 Soret position is blue-shifted 4 nm relative to Zn-Ce_6-H63N (Table 3.8). This is probably due to the greater porphyrin solvent-exposure within the heme biding site (discussed above with regard to bound heme) rather than the presence of His 7.

Neither apo-H63N or apo-M7H showed any Chl *b* binding suggesting that the cyt

Table 3.8: Protein-bound Zn-Ce_6 absorbance

Protein	Peak Position (nm)		
	Soret	Q_X	Q_Y
none	411	518	633
imidazole	420	524	639
H23H42	417	nd	641
H23M42	417	nd	641
H63N	425	527	646
M7H	421	525	646

heme binding site has some selectivity. Nevertheless cyt b_{562} proved to be a useful protein for the binding of a single porphyrin in a well-defined binding site. This is exploited in Chapter 5. A final attempt to create a peptide capable of binding an excitonically-coupled porphyrin dimer is outlined below.

3.4 3hlx: A Radical Cytochrome b_{562} Mutant

The H63N heme binding pocket was able to accommodate a single porphyrin molecule. In M7H, despite the presence of two potential ligands, only one porphyrin bound, presumably due to space constraints within the binding pocket. One key difference between the *de novo*-designed peptides used here and cyt b_{562}, is that the cyt has quite different apo- and holo-protein conformations. The apo-cyt b_{562} has a reasonably well-order structure except for the C-terminal helix, which is unfolded. Upon heme, and presumably other porphyrin, binding this region of the protein becomes helical. This allows a "snug" fit around the bound porphyrin at the expense of protein stability in the apo-protein.

It was reasoned that the C-terminal helix could be removed from M7H without completely disrupting the proteins conformation. The resultant three-helix-bundle (3hlx) may be able to still bind a porphyrin (care of His 7) and the hydrophobic residues previously sequestered by the C-terminal helix could allow the 3hlx protein to dimerise.

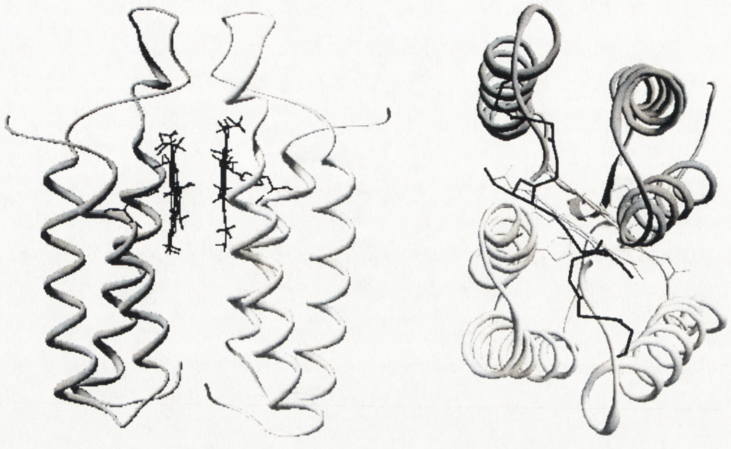

Figure 3.18: Molecular modelling of dimerised porphyrin-bound His3hlx

Thus, the protein would be a six-helix-bundle homo-dimer and the heme binding site would now perhaps be large enough to accommodate a porphyrin dimer. A molecular model of this protein is shown in Figure 3.18.

The 3hlx protein was created and and the mutagenesis is described in Chapter 2.1. The C-terminus was removed from after Gly 82, which is within the loop linking helix 3 and 4. To ensure that the protein would dimerise a new C-terminal comprising the sequence GGGC was added. A similar sequence has been used at the C terminus of the original single-helix heme maquettes (Choma *et al.*, 1994; Gibney & Dutton, 2001) and the cysteine allows the covalent dimerisation of these peptides. The same was hoped to be possible with the semi-synthetic 3hlx protein. The protein was expressed analogously to the other cyt b_{562} mutants in *E. coli* and surprisingly the crude cells showed some pink colour characteristic of the recombinant cyt b_{562} proteins which bind heme *in vivo*. These cells were lysed and the absorbance spectrum of the crude supernatant is shown in Figure 3.19. The spectrum is similar to reduced wt cyt b_{562} and largely consists of low-spin heme. It is not known what the heme's sixth ligand would be in this case. There is an unusual un-assigned absorbance at 502 nm and significant absorbance at 630 nm, which is characteristic of high-spin (singly-ligated) heme. This absorbance was due to the presence of the 3hlx protein as a control experiment, with an *E. coli* culture lacking the plasmid encoding the 3hlx protein, failed to show any significant

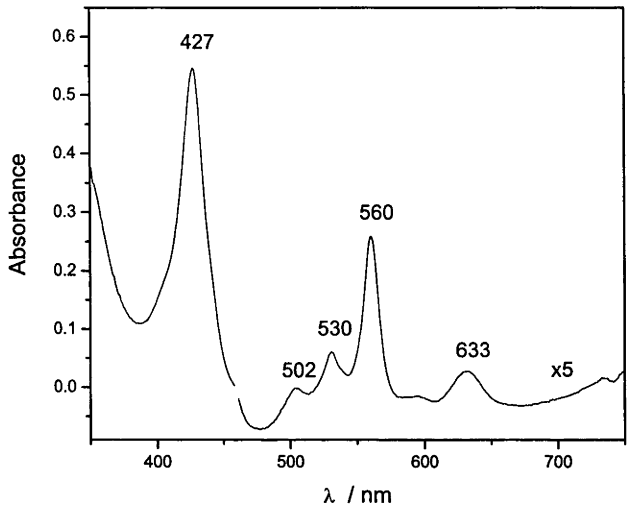

Figure 3.19: Absorbance spectra of the crude supernatant of His3hlx-over-expressing *E. coli* cells. The background absorbance was fit with a polynomial and subtracted.

heme absorbance.

It proved to be very difficult to purify this protein but it proved possible under denaturing conditions using urea. Some of the protein covalently dimerised as judging by non-reducing SDS PAGE (Figure 3.20 A) but the yield was variable and never 100 %. The C-terminal GGGC sequence is not stabile in *E. coli*[7] and thus some of the protein is probably cleaved *in vivo*. This protein would be unable to covalently dimerise. Size exclusion chromatography of the 3hlx protein gave a single peak with a similar elution time under both both reducing and non-reducing conditions (Figure 3.20 B and C, respectively). This suggests that the protein is able to non-covalently dimerise as designed. The apparent mass of the protein is about 30 kDa which is in excellent agreement with the theoretical mass of the dimer, 28 kDa. If the protein is dimerised in a similar conformation to that shown in Figure 3.18, it is much more globular than the highly asymmetric wt cyt b_{562} (see Section 3.2). Thus, the chromatographic properties of the 3hlx dimer would be expected to be well-behaved (i.e. the apparent and

[7]Stability was judged by the instability index computed with ExPASy ProtoParam, http://us.expasy.org/tools/protparam.html

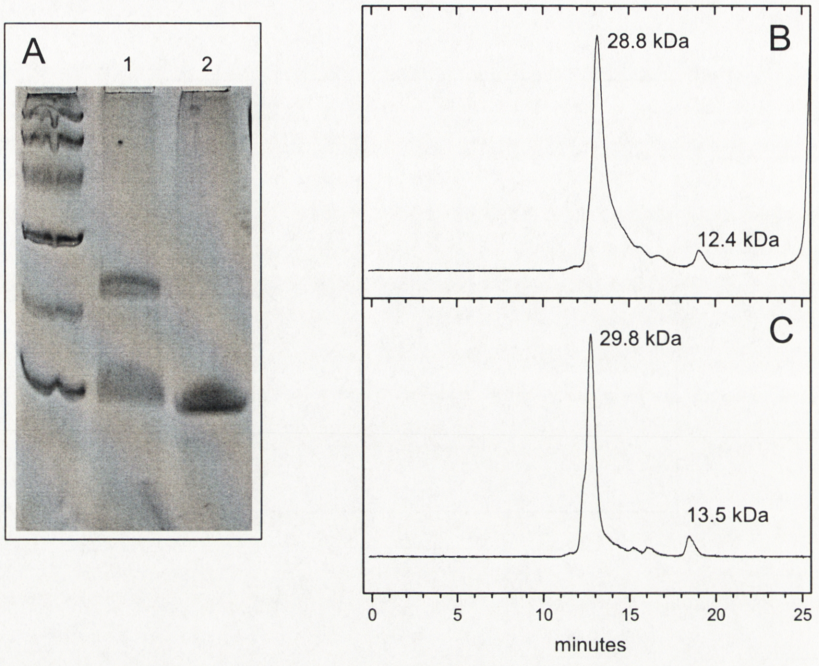

Figure 3.20: (A) SDS-PAGE of His3hlx in the absence (1) and presence (2) of β mercaptoethanol showing cross-linking of the peptide. (B) Size exclusion chromatography of His3hlx in the presence and (C) in the absence of DTT showing non-covalent dimerisation of the peptide.

theoretical mass should be similar).

The purified 3hlx protein had no heme bound as judged by absorbance. The protein was reconstituted with Fe(III)-heme. The bound heme had an absorbance maxima at about 400 nm and is similar to that of penta-coordinate myoglobin-bound heme (data not shown). The Fe(III)-heme bound with a K_{d} of $\sim$0.5 μM, at least 500-fold weaker than in M7H ($<$ 1 nM)). The 3hlx protein was also titrated with ZnPP and this is shown in Figure 3.21. The K_{d} of ZnPP binding to 3hlx (2.1 μM) is nearly 2 orders of magnitude weaker than that obtained for binding to H63M ($\sim$70 nM). The absorbance of bound ZnPP shows no evidence for any porphyrin excitionic coupling. The same can be said for the ZnPP fluorescence (not shown). The binding stoichiometry was not determined due to uncertainty in the protein concentration[8]. It seems that while the 3hlx protein is able to bind both heme and ZnPP it is not able to do so in a conformation conducive to binding a special-pair-like porphyrin dimer.

[8]The estimated absorption coefficient at 280 is very low due to a lack of trp residues.

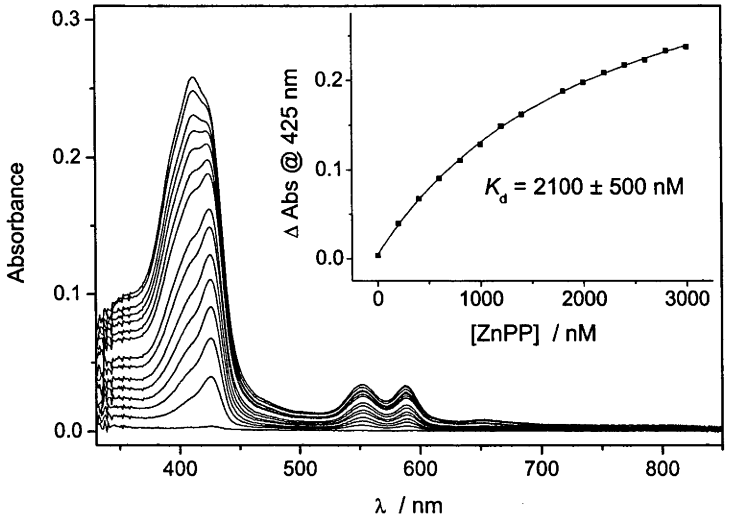

Figure 3.21: Reconstitution of His3hlx with ZnPP

3.5 Summary

A range of porphyrins (heme, ZnPP, Zn-Ce_6, Chl) were shown to bind to *de novo*-designed heme-binding peptides, cyt b_{562}, and/or a semi-synthetic hybrid protein. Binding was shown to involve ligation to a His residue. Chl would not bind to cyt b_{562}, which has a heme binding pocket, but would bind to a *de novo*-designed peptide via a His. Presumably there are steric constraints within the cyt b_{562} binding pocket that are absent is the less well-defined binding site of the *de novo* peptides. Generally the absorbance of the cyt b_{562}-bound porphyrins were red-shifted relative to their *de novo* peptide-bound counterparts. This is probably due to a lower dielectric within the cyt binding pocket.

By altering a heme ligand (M7H) in cyt b_{562}, the binding preference for Fe(II)- over Fe(III)-heme was reversed. This can be correlated with the different redox properties of the M7H and H63N cyts. The differing stability of the ferrous- and ferri-H63N and M7H holo-proteins can also be accounted for in terms of a thermodynamic square. The creation of a *de novo*-designed peptide with a His/Met heme-binding motif showed some evidence for His/Met heme ligation (700 nm CT band, binding stoichiometry)

but had a redox potential consistent with *bis*-His ligation.

CHAPTER 4

Quinone binding

Several mutants of the *E. coli* cyt b_{562} have been designed to bind a quinone within the hydrophobic interior of the protein. The quinone binding site is novel and the quinone is bound covalently to an engineered cysteine. The bound quinone remains redox active and the 2-electron reduction potential can be tuned by mutating amino acids neighbouring the binding site.

4.1 Quinone Chemistry

Quinones are diketones and have the general structure $O = C - (C = C)_n - C = O$. Ubiquinone (ubiQ), named after it's ubiquitous presence in nature, is a *para*-benzoquinone and is found in, among other places, the mitochondrial respiratory chain and bacterial photosynthetic reactions centres. Menaquinone, a 1,4-napthoquinone, is similarly found in some reaction centres and mitochondrial complexes such as cyt bc_1. In place of ubiQ, plastoquinone, another benzoquinone, is found in the reaction centres of cyanobacteria and higher plants. The structures of these three quinones are shown in Figure 4.1. Typically quinones are non-covalently associated with proteins and act as one or two-electron donor/acceptors in ET reactions.

Redox Chemistry

Typically quinones are excellent electron acceptors and in aprotic solvents are reduced in two 1-electron reactions forming a semiquinone anion ($Q^{-\cdot}$) then the dianion (Q^{2-}). *p*-benzoquinone (*p*BQ) is the simplest of the *para*- quinones and the redox and protonation states of this quinone are shown in Figure 4.1. Due to electrostatic considerations, the formation of the dianion requires more energy than the formation of the semiquinone. Thus, the two redox reactions are resolved and reversable with n=1 behaviour[1]. This is not the case in protic solvents where the quinone reduction can be

[1] n=1 behaviour describes a one-electron redox reaction, while n=2 behaviour describes a 2-electron reaction

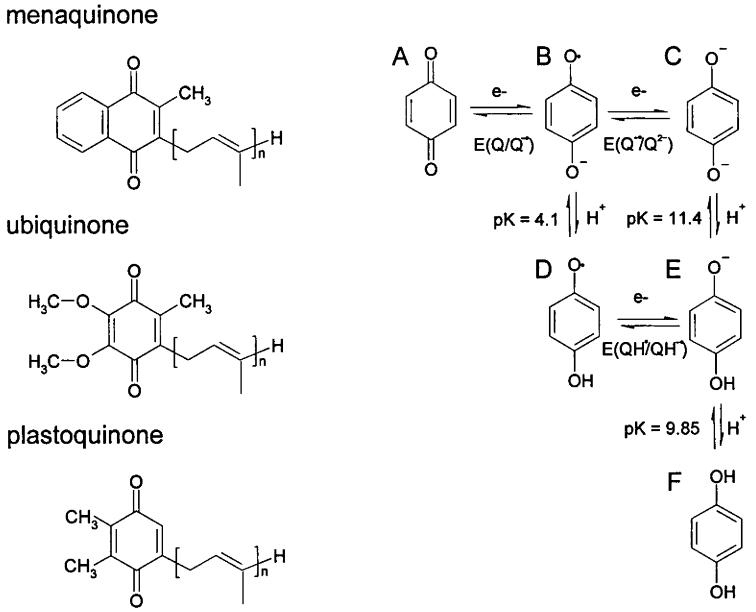

Figure 4.1: Left, The structures of some common biological quinones. The phytol tail is of variable length and is species-specific. Right, The redox and protonation states of benzoquinone at pH > 0. The pK values are taken from (Chambers, 1988). See the text for a description.

accompanied by protonation[2]. The physiologically-relevant pK values for the steps in pBQ reduction are shown in Figure 4.1. As the Q^{2-} oxygens have a high proton affinity (p$K > 11$), Q^{2-} is neutralised by protonation (forming QH_2) and thus stabilised relative to the semiquinone. The result is that $E(Q^{-\cdot}/Q^{2-}) \gg E(Q/Q^{-\cdot})$ and the reduction of the quinone shows n=2 behaviour. Essentially the reduction is coupled to proton binding in a 2-electron, 2-proton reaction:

$$Q + 2e^- + 2H^+ \rightleftharpoons QH_2. \tag{4.1}$$

For a review see (Depew & Wan, 1988; Rich, 2004). This makes the study of the aqueous semiquinone rather challenging. The $E(Q/Q^{-\cdot})$ values in water can be calculated from electrochemistry performed at very high pH (essential aprotic) and extrapolated

[2]A note on nomenclature used here. If the protonation state of the quinone species is not explicit then the semiquinone and doubly-reduced species will be presented as $Q^{-\cdot}$ and Q^{2-}, respectively.

to pH 7 values by:

$$E(Q/Q^{-\cdot})_{pH} = E(Q/Q^{-\cdot})_{pH7} + 59\log\left(\frac{10^{-pK} + 10^{-pH}}{10^{-pK} + 10^{-7}}\right), \tag{4.2}$$

where pK is $pK(Q^{-\cdot}/QH^{\cdot})$. It is more difficult to measure $E(Q^{-\cdot}/Q^{2-})$ and this is usually calculated from the relationship between the 1- and 2-electron reduction potentials:

$$E(Q/Q^{2-}) = \tfrac{1}{2}[E(Q/Q^{-\cdot}) + E(Q^{-\cdot}/Q^{2-})]. \tag{4.3}$$

Information regarding the relative stability of the semiquinone can be derived from another characteristic property of the quinones, the comproportion (or dismutation) reaction:

$$Q + Q^{2-} \rightleftharpoons 2Q^{-\cdot}, \quad k_{semi} = \frac{[Q^{-\cdot}]^2}{[Q][Q^{2-}]}, \tag{4.4}$$

where k_{semi}, the semiquinone stability constant, is related to the difference in 1-electron reduction potentials:

$$E(Q/Q^{-\cdot}) - E(Q^{-\cdot}/Q^{2-}) = \frac{RT}{nF}\ln k_{semi}. \tag{4.5}$$

For the case of *p*BQ in water at pH 7.0, $E(Q/Q^{-\cdot})$ = 99 mV, $E(Q/Q^{2-})$ = 286 mV (Depew & Wan, 1988); therefore $E(Q^{-\cdot}/Q^{2-})$ = 473 mV (eqn 4.3) and k_{semi} = 3.7 x 10^{-7} (eqn 4.5). Thus, at neutral pH no semi-*p*BQ is observed. However, as the pH is increased above pH 7, $E(Q/Q^{-\cdot})$ does not change but $E(Q^{-\cdot}/Q^{2-})$ decreases by 120 mV per pH unit at pH < p*K*(QH^{-}/QH_2) (p*K*$\sim$ 10, Figure 4.1). This decreases $[E(Q/Q^{-\cdot}) - E(Q^{-\cdot}/Q^{2-})]$ and thus stabilises the semiquinone. This has been exploited to resolve quinone 1-electron reduction potentials. See for example Robertson *et al.* (1984).

Protein-Bound Quinones

In the pheophytin/quinone type RCs the final two electron acceptors are quinones. The penultimate acceptor, the primary quinone, Q_A, is only involved in 1-electron reduction ($Q \rightarrow Q^{-\cdot}$) and is not doubly-reduced under physiological conditions. This contrasts with the ultimate acceptor, the secondary quinone, Q_B, which is reduced (by Q_A) in two separate 1-electron reductions ($Q \rightarrow Q^{-\cdot} \rightarrow Q^{2-}$) and becomes protonated[3]

[3]protonation may be coupled to ET rather than subsequent to reduction.

($Q^{2-} + 2H^+ \rightarrow QH_2$). In order for Q_A to doubly reduce Q_B:

$$E(Q_A/Q_A^{-\cdot}) < E(Q_B/Q_B^{-\cdot}) \quad (4.6)$$

$$E(Q_A/Q_A^{-\cdot}) < E(Q_B^{-\cdot}/Q_B^{2-}). \quad (4.7)$$

This is complicated by the fact that in *R sphaeroides* RCs and in PS II of cyanobacteria and higher plants, Q_A and Q_B are chemically identical quinones (ubiQ in the RC, plastoquinone in plants). Thus, the difference in the properties of these quinones must be due to specific interactions between the quinone and the protein. Specifically, the protein must lower the $E(Q/Q^{-\cdot})$ of Q_B relative to Q_A in order to satisfy eqn 4.6. If we consider the *Rhodopseudomonas spheroides* BRC (where Q_A and Q_B are ubiQ), eqn 4.6 has been verified, as $E(Q_A/Q_A^{-\cdot})$ = -45 mV (Dutton *et al.*, 1973), while $E(Q_B/Q_B^{-\cdot})$ has been calculated to be about +20 mV (Wraight, 1998). Differences in the protein environment can (at least qualitatively) account for the differing redox properties of Q_A and Q_B. Q_A is tightly bound within a relatively hydrophobic part of the M subunit while Q_B is loosely associated with a more polar region of the L subunit. The semiquinone anions can be stabilised by a positive electrostatic potential, which can be provided through hydrogen-bonding, charged neighbouring amino acids and the dipole of the protein backbone. The backbone dipole may play a significant role as it is very large in RCs (Gunner *et al.*, 1996).

As yet, there is no general structural motif for a quinone binding site (Fisher & Rich, 2000). The best characterised binding site is the Q_A site of the BRC (Allen *et al.*, 1988), which has recently been shown to be structurally similar to the Q_A site of photosystem II (Ferreira *et al.*, 2004) (Figure 1.4) and has similarites to the Q_D quinone binding site in the *E. coli* fumarate reductase (Iverson *et al.*, 1999). Quinone binding is stabilised by hydrogen-bonding to the quinone carbonyl oxygen, van der Waals contact between the protein and quinone head group (benzoquinone moiety) and especially by hydrophobic binding of the large quinone phytol tail (Warncke *et al.*, 1994). As discussed in Chapter 1.1, the protein environment not only plays a major role both in modulating the redox properties of the cofactors (see e.g. (Ivancich *et al.*, 1998; Rinyu *et al.*, 2004)) but also the ET reaction (discussed in (Winkler *et al.*, 1999; Page *et al.*, 1999)). It would then seem to be useful to use a protein-based system to mimic or

study the photochemistry of a reaction centre. However, whilst quinones are common biological redox-active cofactors we are not aware of any previous work using them as bound electron donor/acceptors in designed or engineered proteins. The *de novo* design of a binding site that mimics all the features of the natural system is far too complex. To simplify this, I took a different approach which binds the quinone covalently.

4.2 A Novel Quinone-Binding Protein

It has long been known that quinones such as *p*BQ form addition compounds with thiol-containing compounds (Snell & Weissberger, 1939) including cysteine (Redfearn, 1965). The reaction of cysteine and coenzyme Q_0 (CoQ_0) (ubiQ lacking the phytol tail) is thought to follow the reaction scheme in Figure 4.2.

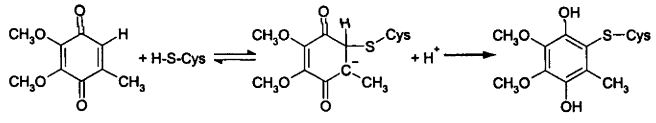

Figure 4.2: The reaction scheme of CoQ_0 with cysteine.

Whilst the quinones associated with photosynthetic reaction centers are not covalently attached to the protein this is not expected to have a major influence on the redox properties of the quinones (Brunmark & Cadenas, 1989). Most model protein systems previously used for ET have relied upon the covalent attachment of one or both of the donor/acceptor molecules to the surface of the protein (reviewed in Bjerrum *et al.* (1995)). As a result, the donor/acceptor molecules are not shielded from the high dielectric solvent. The solvent exposure is expected to influence the ET event as solvent reorganisaton energy will play a major role. By attaching the quinone to a cysteine within the interior of the protein it is possible to bury both donor and acceptor within the interior of the protein. This has several advantages. The reorganisation energy should be reduced (relative to a quinone bound to the protein surface) due to less sol-

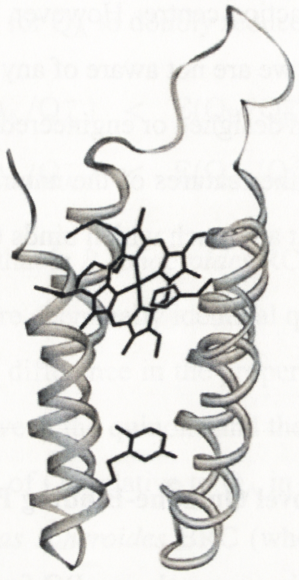

Figure 4.3: Molecular model of quinone-bound cyt b_{562} I17C showing the porphyrin binding site and cysteine-bound benzoquinone.

vent reorganisation. Additionally the route of ET will be through the protein, and free of the solvent. The advantage of this is that the electronic coupling will more closely resemble that of natural proteins ($\beta \sim 1.4$, see Chapter 1).

To initially study the reaction of cysteine with quinone, reduced glutathione (γ-L-Glu-L-Cys-Gly) was used as a minimalistic cysteine-containing peptide and *p*BQ was used as a simple quinone. Mass spectrometry of 1:1 GSH:*p*BQ in water showed 2 peaks with m/z = 414.0 and 435.9 (data not shown) which were assigned as the protonated and Na salt of glutathionyl-hydroquinone (GS-*p*BQ-H_2), respectively confirming the covalent attachment of *p*BQ to glutathione.

Design of the Quinone Binding Site

Once it was established that benzoquinones could efficiently react with cysteine, cyt b_{562} H63N (described in the previous chapter) was mutated at amino acid position 17 replacing isoleucine with a cysteine creating the I17C mutant. This residue was chosen as it is not solvent-exposed in the holo-protein but reasonably accessable in the apo-protein when the porphyrin is removed. The equivalent residue in a structural homologue of cyt b_{562}, cyt *c* prime, is Trp. A cysteine-benzoquinone conjugate is of similar

Table 4.1: Absorbance, EPR, redox properties and chemical stabilities of wildtype, H63N and I17C cyt b_{562}.

Protein	Absorbance Maxima (nm)		EPR	E_{m7}	$^1\Delta G^{H_2O}$
	oxidised	reduced	g_z, g_y	(mV)	(kJ mol^{-1})
wt	418, 529, 558[a]	427, 531, 562[a]	3.04, 2.18[b]	+189[c]	30 ± 5
H63N	418, 530, 560	427, 531, 561	3.04, 2.18,	+187	29 ± 3
I17C	418, 530, 560	427, 531, 561	3.04, 2.19,	+192	34 ± 3

[1] Guanidine denaturation of the ferri-proteins. Additional data (*a*) taken from Itagaki & Hagar (1966); (*b*) from Walker *et al.* (1986); (*c*) from (Barker *et al.*, 1996).

size to Trp so it was estimated that cyt b_{562} could accommodate the quinone in this postion. Additionally, molecular modelling of the protein (Figure 4.3) suggested that the edge-to-edge distance between the bound porphyrin and quinone would be about 10 Å which is the roughly the average distance between cofactors in the photosynthetic reaction centres (Moser *et al.*, 2003) and a feasible distance for electron tunnelling to occur over (Page *et al.*, 1999).

Characterisation of the I17C Protein

The absorbance, redox, and EPR properties of the heme-bound holo-I17C protein are indistinguishable to those of the H63N or wt protein suggesting that the I17C mutation does not disrupt the heme binding site (see Table 4.1). About 30% of the purified protein contained bound heme which was successfully removed by the method of Teale (1959) and no heme was detected in the apo-protein after this treatment. The apo-I17C protein had a tendency to cross-link during purification which was reversible by treatment with dithiothreitol. This indicates that the cysteine residue is at least partially solvent exposed in the apo-protein.

Quinone Binding

It has been reported that cysteine-reacted quinone has a characteristic absorbance spectrum with a peak at ~303 nm (Redfearn, 1965; Brunmark & Cadenas, 1989). This

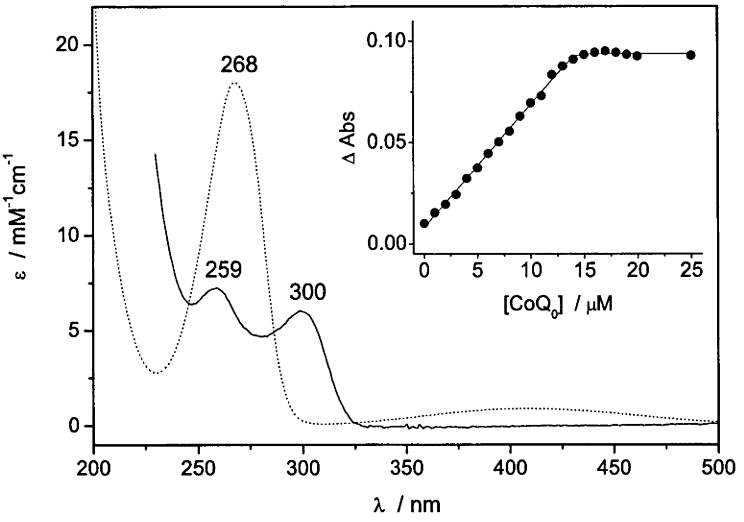

Figure 4.4: Absorbance spectra of CoQ_0 (dotted line) and I17C-bound (reduced) CoQ_0 (solid line). The inset shows a titration of CoQ_0 into 15 μM apo-I17C as measured by absorbance at 300 nm. Both samples were in 50 mM KP_i, 100 mM KCl, pH 7.0.

was used to monitor the titration of CoQ_0 into apo-I17C, which is shown in Figure 4.4. Quinone binding occurred with a concomitant loss of free thiol (cysteine) as measured by Ellman's reagent (data not shown) and no binding was observed if the apo-protein was cross-linked prior to the addition of the quinone. There was no cross-linking of the protein after reaction with CoQ_0 and the loss of reduced cysteine is attributed to the covalent attachment of the quinone. The absorbance at ~303 nm is thought to be due to the doubly-reduced (hydroquinone) cysteine-quinone conjugate (Redfearn, 1965) and is consistent with the reaction scheme in Figure 4.2.

Hydroquinone fluoresces in aqueous solution with an excitation peak at 290 nm and an emission peak at 330 nm (Tchaikovskaya *et al.*, 2000). Upon the stoichiometric addition of *p*BQ to I17C a fluorescent species was observed with these spectral attributes, confirming the formation of bound hydroquinone (Figure 4.5). The binding of Fe^{III}-heme to *p*BQ-bound I17C caused a ~30% quenching of the hydroquinone fluorescence (data not shown). Quenching of fluorescent protein side-chains such as

Table 4.2: Protein-bound hydroquinone fluorescence

Protein	eqn	K_{SV} (M^{-1})	V (M^{-1})	peak position
I17C	4.8	0.69 ± 0.05	-	333 nm
GS	4.8	1.9 ± 0.1	-	333 nm
I17C, denatured	4.8	2.0 ± 0.1	-	346 nm
I17C, pH 9	4.9	2.0 ± 0.1	$0.55 \pm .04$	345 nm
L30Y	4.9	1.1 ± 0.2	$0.74 \pm .09$	334 nm
L30H	4.9	0.9 ± 0.2	$0.6 \pm .1$	333 nm

Trp by heme through resonance energy transfer is well characterised (see Willis *et al.* (1990) and references within) and a similar mechanism is expected to occur for the hydroquinone. The distance between the heme iron and hydroquinone was then estimated using Förster theory (see Chapter 1.4). The spectral overlap (J) was calculated to be 2.6 x 10^{-15} and the quantum yield of the bound hydroquinone estimated to be 0.1 (Tchaikovskaya *et al.*, 2000). Using the rather poor approximation[4] that $\kappa^2 = 2/3$, R_0 was calculated (eqn 1.8) to be ~18 Å. Thus, with a quenching of 30% the distance between the heme iron and hydroquinone is ~21 Å. There is a large error in this value due to uncertainty in the quantum yield and particularly κ^2. Nevertheless, this fluorescence quenching suggests that the porphyrin/quinone distance is in the right ballpark when considering the molecular model (Figure 4.3).

The fluorescence of bound hydroquinone was used to determine the extent of solvent shielding conferred by the protein by using sodium iodide as a quencher. Charged iodide will only quench solvent-exposed chromophores and thus if the bound hydroquinone is buried within the protein then quenching will not occur. Stern-Volmer quenching analysis was performed using either eqn 4.8 or eqn 4.9:

$$F_0/F = 1+K_{SV}[Q] \tag{4.8}$$

$$F_0/F = (1+K_{SV}[Q])e^{V[Q]} \tag{4.9}$$

where K_{SV} is the Stern-Volmer constant, V is the static quenching constant and Q is

[4] $\kappa^2 = 2/3$ when the donor and acceptor can undergo unrestricted isotropic motion

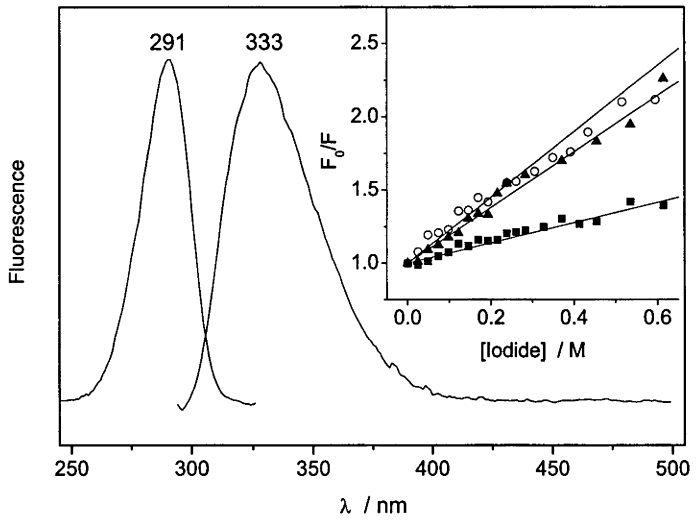

Figure 4.5: Fluorescence excitation and emission spectrum of reduced (hydroquinone) I17C-bound *p*BQ. The fluorescence from the protein (tyrosine) has been subtracted. The spectra were acquired with excitation at 290 nm or emission at 330 nm with an entry and exit bandpass of 2 nm. The inset shows Stern-Volmer plots of potassium iodide quenching of this fluorescence for GS-*p*BQH$_2$ (circles), denatured (4 M guanidine) I17C-*p*BQH$_2$ (triangles) and native I17C-*p*BQH$_2$ (squares). The quenching constants are given in Table 4.2.

the quencher concentration, which in this case is molar potassium iodide. If, at higher concentrations of quencher, the Stern-Volmer plots show a positive deviation from linearity, then eqn 4.9 is used, which is based on the sphere-of-action static quenching model. This is based on the assumption that quenching can occur with unit efficiency for a Poisson distribution of a non-bound quencher within a volume (V) around the fluorophore. Typical Stern-Volmer plots for hydroquinone in solution and bound to I17C and glutathione are shown in the inset in Figure 4.5. The measured quenching constansts are given in Table 4.2. GS-*p*BQ-H-2 has a K_{SV} of 1.9 M^{-1} while native apo-I17C-*p*BQ-2 (no heme bound) has a K_{SV} of 0.69 M^{-1}. The reduced K_{SV} when hydroquinone is bound to I17C suggests the cyt is providing some solvent shielding. Denatured apo-I17C-*p*BQ-2 (in 4 M guanidine) has a K_{SV} of 2.0 M^{-1}. similar to that

of GS-*p*BQ−2. The increase in K_{SV} of I17C-bound hydroquinone upon denaturation suggests that the native protein confers some solvent shielding to the quinone which is lost upon denaturation of the protein in guanidine. A similar increase in K_{SV} was seen in I17C-bound hydroquinone when the pH was raised from 7.0 to 9.0. This suggests that there is also some pH-induced denaturation of the protein. When possible all following work was preformed at pH 7.0.

The effect of quinone-binding on the stability of the I17C protein was examined by guanidine denaturation. The binding of *p*BQ to I17C does not significantly effect the stability of the heme-bound protein toward denaturation by guanidine at pH 7.0. The denaturation curves are shown in Figure 4.6 and the ΔG values[5], given in Table 4.3. Whilst there is no significant change in ΔG^{H_2O}, the cooperatively of the transition (m) is somewhat decreased in the quinone-bound protein. This suggests that the bound quinone causes a more disordered or inhomogeneous protein conformation. The loss of *p*BQ solvent-shielding during protein denaturation was also determined by measuring the extent of fluorescence quenching of bound hydroquinone by 0.2 M NaI in the presence of titrated guanidine. This was done in the absence of heme as it complicated the measurements due to its quenching of *p*BQ fluorescence. The solvent screening of the protein is disrupted with a ΔG^{H_2O} of 7 kJ mol^{-1}. The stability of apo-wt cyt b_{562} has been reported by Feng & Sligar (1991) and (Robinson *et al.*, 1998) as discussed in the previous chapter. In urea the loss of secondary structure in the apo-wt protein is reported to occur with a ΔG^{H_2O} of 3.2 kcal mol^{-1} (13 kJ mol^{-1}) (Feng & Sligar, 1991). In the case of the loss of hydroquinone solvent shielding in I17C, either: (*i*) the difference in charge-screening by urea and guanidine account for the differences in ΔG^{H_2O}; or (*ii*) the secondary structure is destabilised by 6 kJ mol^{-1}; or (*iii*) the bound hydroquinone becomes solvent exposed prior to the loss of all secondary structure. As the ΔG^{H_2O} of ferri-wt and ferri-I17C are not significantly different (*ii*) is unlikely. The extent of the hydrophobic effect has been estimated to be ~9.9 kJ nm^{-2} of water-excluded surface (Chothia, 1974). The surface area of a hydroquinone molecule was

[5]The denaturation was assumed to occur by a folded to unfolded transition and the data in Figure 4.6 were fit to eqn 2.2. ΔG^{H_2O} and m values were obtained from these fits

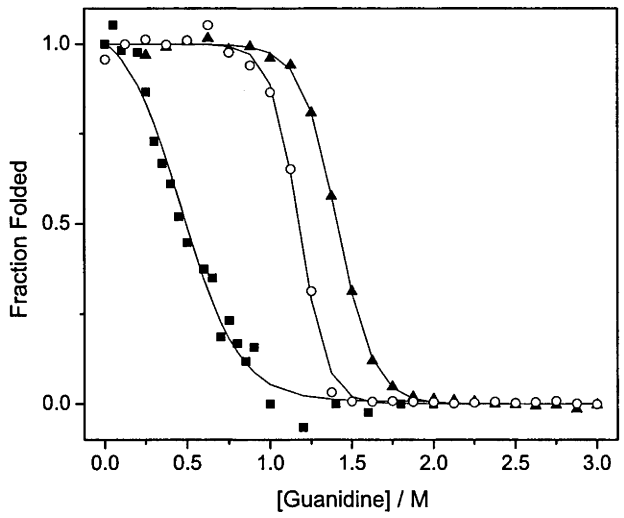

Figure 4.6: Guanidine denaturation of I17C. Loss of *p*BQ solvent shielding in apo-I17C as measured by fluorescence quenching (squares) and loss of bound heme to I17C (circles) and *p*BQ-bound I17C (triangles). The bound *p*BQ causes a reduction in bound heme absorbance which is seen in the initial data points for heme-I17C-*p*BQ where, upon quinone denaturation, heme absorbance is restored to normal levels.

calculated[6] to be 119 Å^2 (1.19 nm^2) and the disruption of van der Waals contacts between the surface of one side of the bound hydroquinone ($\sim$0.6 nm^2) would account for the ΔG^{H_2O} measured. The 2 hydroxide groups in hydroquinone are not really hydrophobic however and thus the magnitude of the "hydrophobic effect" is probably less than 10 kJ nm^{-2} in the case of hydroquinone. If this is the case then the denaturation simply suggests that more than 0.6 nm^2 of hydroquinone are buried.

Quinone Redox Properties

Whilst the sulfur addition to the quinone causes the reduction of the quinone to hydroquinone the bound quinone can be re-oxidised. The 2-electron equilibrium oxidation/reduction of I17C-bound CoQ_0 occurs with a midpoint potential (E_m) of +205 mV at pH 7 (Figure 4.7). The E_m of CoQ_0 in solution was similarly measured to be +180

[6]The area of an energy-minimised structure of hydroquinone was calculated in Swiss-PdbViewer from a surface calculated with a 1.4 Å probe.

mV (Figure 4.7) which is in reasonable agreement with reported values (+162 mV (Lemma *et al.*, 1990)). Thus the combined effect of sulfur attachment and the effect of the protein environment on the redox properties of CoQ_0 appear to be minimal (about +25 mV). Both titrations in Figure 4.7 were fit to a single Nernst curve (eqn 2.8) with n as a free variable and both showed n=2 behaviour. No semiquinone absorbance was observed and the titrations showed isosbestic behaviour consistent with only two species. This is consistent with $k_{semi} \ll 1$ for the I17C-bound semiquinone as is the case for ubiQ in solution (Hastings *et al.*, 1998). Thus, the E_m measured likely corresponds to the $E(Q/QH_2)$ reaction.

To determine whether the difference in E_m between CoQ_0 in solution and bound to I17C is due to the presence of a quinone sulfur bond or a more general protein environment effect (e.g. local dielectric), the redox properties of *p*BQ were more closely examined. *p*BQ was chosen as it is better characterised (reviewed in Patai & Rappoport (1988)). The redox potentials of *p*BQ and GS-*p*BQ were measured by cyclic voltammetry (CV) in water at pH 9 with a glassy carbon working electrode. The $E_{1/2}$ of *p*BQ and GS-*p*BQ extrapolated to pH 7 (assuming $E_7(\mathrm{mV}) = E_{pH} + 59\Delta\mathrm{pH}$) are +296 and +263 mV, respectively (data not shown). The value for *p*BQ is in good agreement with literature. The pH dependence of the $E_{1/2}$ of aqueous GS-*p*BQ was determined and a slope of -57 mV per pH unit was fit over a pH range of 5-9. This is consistent with a 2-electron, 2-proton redox mechanism and $pK(Q^{\cdot-}/QH^{\cdot}) < 5$, and $pK(Q^{2-}/QH^{-}) < 9$ as is shown in Figure 4.1 for *p*BQ.

Table 4.3: Guanidine denaturaton of ferri-I17C and ferri-I17C-*p*BQ

Protein	$[Gdn]_{1/2}$ (M)	ΔG^{H_2O} (kJ mol^{-1})	m (kJ mol^{-1} M^{-1})
ferri-proteins			
I17C	1.2	34 ± 4	29 ± 3
I17C-*p*BQ	1.4	31 ± 1	22 ± 1
apo-protein			
I17C-*p*BQ	0.5	7 ± 1	15 ± 1

Direct electrochemistry of cyt b_{562} has been reported (Barker *et al.*, 1996) using pyrolytic graphite or modified gold electrodes. I attempted to measure the redox potential of I17C-CoQ_0 and I17C-*p*BQ using a modified[7] gold electrode but were unable to obtain a stable reversible response. The reasons for this remain unclear. Instead, the redox properties of GS- and I17C-bound *p*BQ were examined by chemical potentiomentry similarly to the titrations shown in Figure 4.7 (data not shown). The $E_{m,7}$ of GS-*p*BQ is +265 mV while that of I17C-*p*BQ is +177 mV. Both titrations showed n=2 behaviour and the GS-*p*BQ potentiometric $E_{m,7}$ is in excellent agreement with the $E_{1/2}$ obtained by cyclic voltammetry. The $E_{m,7}$ of I17C-*p*BQ is about 100 mV lower than that of GS-*p*BQ or *p*BQ. The value for I17C-bound *p*BQ was determined for a sample prepared by the addition of excess quinone and subsequent dialysis (see Chapter 2.4). It is possible that during this relatively lengthy procedure the protein-bound quinone underwent a chemical reaction with the solvent water or hydroxide forming protein-bound-5-hydroxy-1,4-benzoquinone. This was not the case with the GS-*p*BQ experiment which was performed immediately after formation of GS-pBQ-H_2. This *p*BQ hydroxylation is not unprecedented and is discussed in a review by Brunmark & Cadenas (1989). The E_m value of +177 mV is in good agreement with the reported midpoint potential of 5-hydroxy-*p*BQ (+181 mV) (Clarke, 1960). This is also consistent with the bound oxidised quinones absorbance peak position of ~345 nm which is characteristic of 2-sulfur-5-hydroxy-1,4-benzoquinone (Brunmark & Cadenas, 1989) and significantly shifted from that of of 5-sulfur-*p*BQ (367 nm (Brunmark & Cadenas, 1989)). This highlights the problems of working with quinones in aqueous solution. However, cysteine-bound CoQ_0 has a saturated quinone ring and thus is not susceptible to attack by water/hydroxide. Thus, aside form hydroquinone fluorescence experiments, CoQ_0 was the quinone of choice for the remaining experiments.

As the E_m of CoQ_0 does not change substaintially upon binding I17C we will assume that the $E(Q/Q^{-\cdot})$ does not change significantly either. The $E(Q/Q^{-\cdot})$ of ubiQ in water has been estimated to be -100 to -120 mV (Wraight, 1998). The effect of a prenyl group (phytol tail) on $E(Q/Q^{-\cdot})$ is similar to the effect of a methyl group (Prince *et al.*, 1983) which lowers the $E(Q/Q^{-\cdot})$ of *p*BQ by ~80 mV (Prince *et al.*, 1983; Depew &

[7]The gold electrode was modified with the peptide KCTCCA

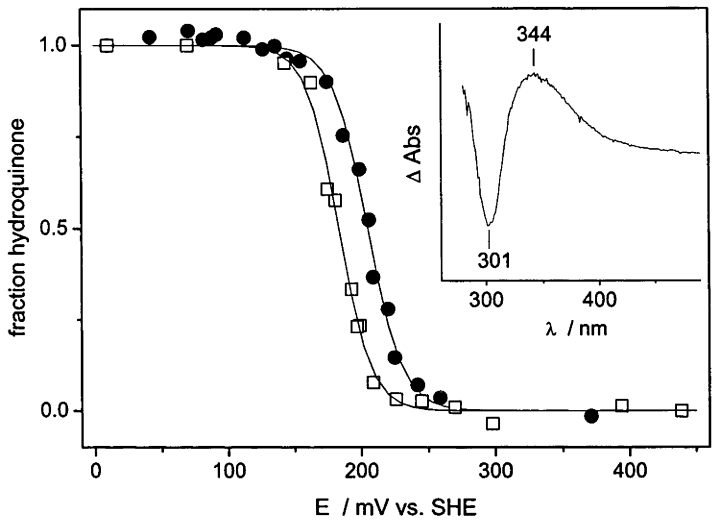

Figure 4.7: Redox titration curves of I17C-bound CoQ_0 (filled circles) and CoQ_0 in solution (open squares) as measured optically in 50 mM KP_i, 100 mM KCl, pH 7.0. The data are fit to a Nernst curve with E_m= +205 mV (n = 1.9 ± 0.1) for I17C-CoQ_0 and E_m= +180 mV (n = 2.1 ± 0.1) for CoQ_0 in solution. The inset shows the oxidised-minus-reduced absorbance difference spectrum of the I17C-CoQ_0 titration.

Wan, 1988). Thus, we can estimate an $E(Q/Q^{-\cdot})$ of -30 mV for CoQ_0 in solution and a similar value for I17C-bound CoQ_0. As mentioned earlier, the value of $E(Q/Q^{-\cdot})$ can often be directly measured at high pH, typically using EPR. This is discussed later in Section 4.4.

4.3 The L30 Mutants

To tune the redox properties of the I17C-quinone a variety of different quinones were bound to I17C. This is further discussed in the following chapter but the values of measured and reported redox potentials of quinone species used in this work are given now in Table 4.4. It proved difficult to find other suitable quinones with significantly lower redox potentials than CoQ_0. As an alternative, the redox properties of the bound quinone were altered by mutating an amino acid neighbouring the bound quinone. In I17C the leucine at position 30 was replaced with a histidine and tyrosine creating the

Table 4.4: Redox properties of the quinones

Quinone	measured $E(Q/Q^{2-})$	reported $E(Q/Q^{2-})$	reported $E(Q/Q^{-\cdot})$
*p*BQ	+296	+286	+99
GS-*p*BQ	+266	-	-
I17C-*p*BQ[1]	+177	-	-
ubiQ	-	+90	-100 - -120[a]
CoQ_0	+180	+162	-
I17C-CoQ_0	+205	+205	-
2-hydroxy-*p*BQ	-	+181[b]	-

All values (mV vs. SHE) are for the quinones in water at pH 7. Reported values are taken from Depew & Wan (1988), except (*a*) from Wraight (1998) and (*b*) from Clarke (1960). [1]This was possibly protein-bound 2-hyroxy-benzoquinone as discussed in the text.

L30H and L30Y mutants, respectively (together denoted the L30 proteins). Leu 30 was carefully chosen after molecular modelling to optimally place the His or Tyr residue in contact with the bound quinone. A molecular model of L30Y is shown in Figure 4.8 and the relative postion of the residue at position 30 in I17C, L30H and L30Y relative to the bound quinone in molecular models are shown in Figure 4.8.

The L30 proteins were expressed and purified as for the other cyt b_{562} proteins. Unlike I17C and L30Y, the L30H protein had no endogenous heme bound after purification. The lack of *in vivo* heme binding suggested that the L30H mutation was fairly destabilising. This was examined by guanidine denaturation and the denaturation curves of the L30 ferri-proteins are shown in Figure 4.9. Both the L30 proteins are significantly less stable than I17C and the ΔG^{H_2O} values are given in Table 4.5. Both L30 proteins contain four mutations relative to wt cyt b_{562}, M0, H63, I17 and L30. It is interesting that the protein tolerated the first three mutations with little change in ΔG^{H_2O}, yet the L30 mutation has reduced the stability (ΔG^{H_2O}) by more than half. Attempts to add additional mutations were abandoned due to the likelihood that any

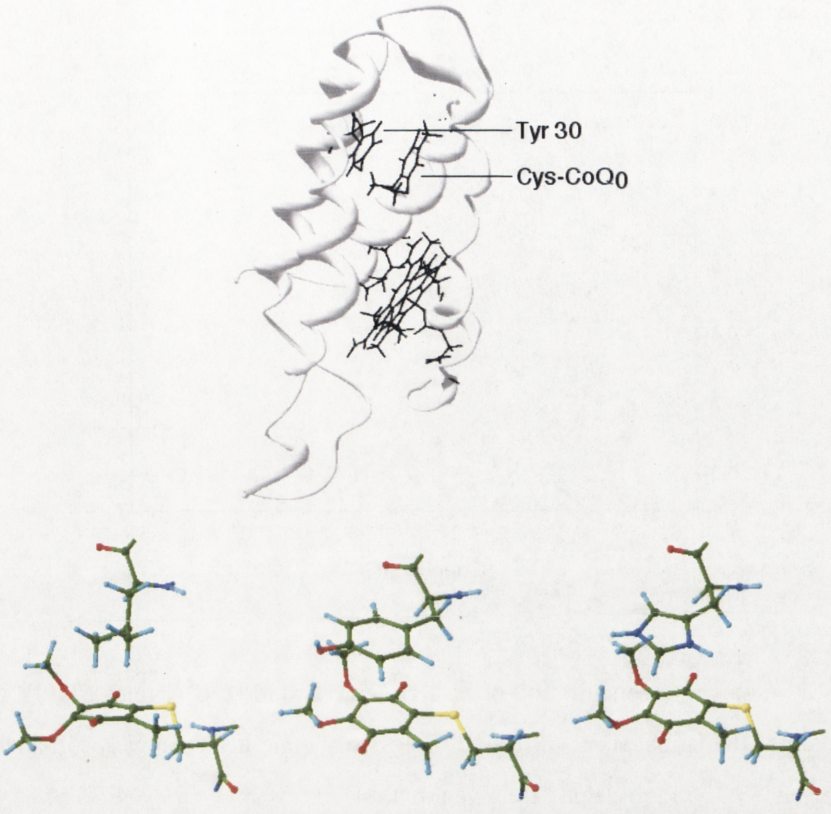

Figure 4.8: Molecular models of CoQ_0-bound L30Y (top) and the postion of the the residue at position 30 relative to the cysteine-bound CoQ_0 in the energy minimised structures of the three L30 proteins from left, I17C, L30Y and L30H (bottom). The closest distance between these residues and the quinone ring is < 3.8 Å.

other mutations would further prevent the correct folding of this protein.

CoQ_0 and *p*BQ still readily bound to the apo-L30 proteins and to determine if the decreased stability of these proteins yielded a more solvent-exposed quinone, iodide quenching was again performed. The Stern-Volmer plots are shown in Figure 4.10 and the K_{SV} values given in Table 4.2. Both L30 proteins have K_{SV} values larger than for I17C-*p*BQ-H_2 but smaller than for solvent-exposed hydroquinone when bound to glutathione or denatured I17C. This suggests that the quinone-binding site in the L30 proteins is altered relative to I17C and is probably more solvent-exposed. It is interesting to also note that while the Stern-Volmer plots for both L30-*p*BQ-H_2 proteins showed deviation from linearity at high iodide concentrations, I17C*p*BQ-H_2 did not.

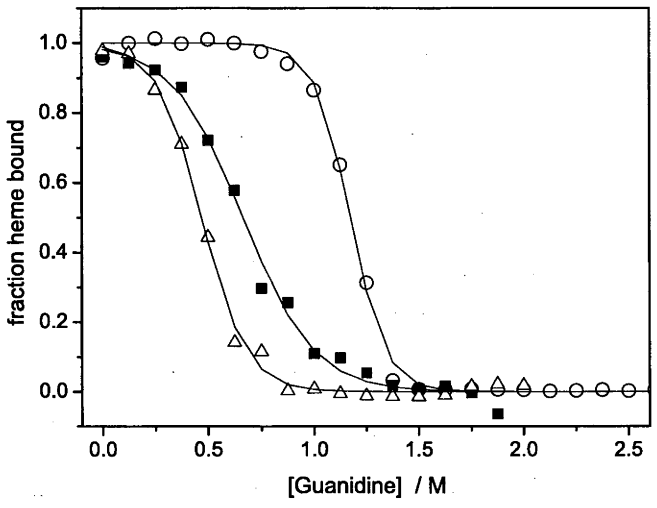

Figure 4.9: Guanidine denaturation of Fe(III)-heme-bound I17C (circles), L30Y (triangles) and L30H (squares) as measured by loss of bound heme Soret absorbance at pH 7. The ΔG^{H_2O} and m values are given in Table 4.5

This too suggests that there are differences in the quinone binding site in the L30 proteins. The cause of theses differences in quenching properties is uncertain and more precise structural information is required.

The redox properties of CoQ_0 bound to the L30 proteins were examined by chemical potentiometry at pH 7 analogously to those in Figure 4.7 and this is shown in Figure 4.11. Both L30H and L30Y drastically lower the $E(Q/Q^{2-})$ potential. Both displayed n=2 behaviour and again no semiquinone was observed. There is a lot of scatter in the L30H data and thus some error in the precise E_m value. This is due to several factors. The protein has a tendency to aggregate at modest concentrations and the experiment was thus performed at a protein concentration with a lower-than-optimal quinone absorbance. Additionally, the low E_m necessitated the use of several naptho- and anthroquinones to mediate this reaction. These have relatively strong and interferring absorbance which complicated deconvolution of the spectra. Nevertheless, the E_m of L30H-bound CoQ_0 is significantly lower than that of L30Y and much lower again than that of I17C-bound CoQ_0.

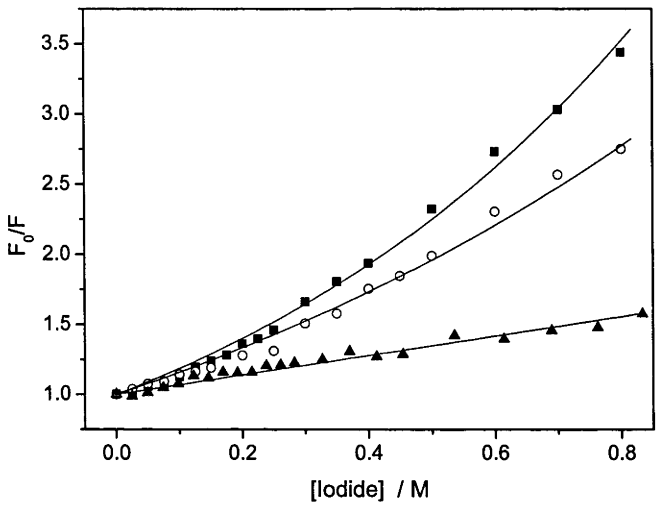

Figure 4.10: Stern-Volmer plot of potassium iodide quenching of *p*BQ-H_2-bound fluorescence in apo-I17C (triangles), apo-L30Y (circles) and apo-L30H (squares). The experimental conditions are identical to those in Figure 4.5 and the K_{SV} values are given in Table 4.2.

The iodide quenching suggests that the quinone is more solvent exposed in the L30 proteins, yet this should lead to more positive E_m values. The Tyr placement in L30Y is designed to allow the Tyr phenol moiety to π-stack with the quinone ring (Figure 4.8). The negative electrostatic potential associated with the tyrosine π system should destabilise the semiquinone anion and thus lower $E(Q/Q^{-\cdot})$ and in-turn $E(Q/Q^{2-})$. It is also possible that the Tyr could form a H-bond with one of the quinone carbonyl oxygens. This could stabilise hydroquinone formation and also lower the E_m. The effect of the histidine is more difficult to explain. It is quite possible that the histidine could also form a hydrogen-bond with a quinone oxygen. However, it is difficult to envisage that the bound quinone is completely sequestered from the solvent and thus not hydrogen-bonded to water.

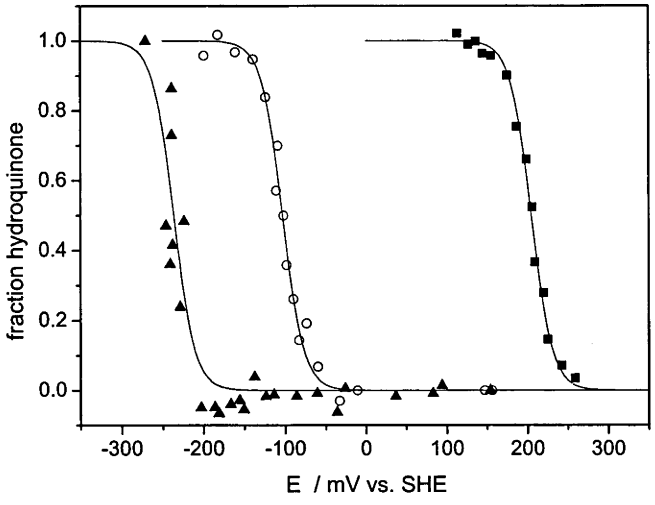

Figure 4.11: Chemical redox potentiometric titrations at pH 7.0 of CoQ_0 bound to apo-I17C (squares) apo-L30Y (circles) and apo-L30H (triangles). All three titrations are fit to a single Nernst curve for 2 electron reduction (n = 2). The E_{m7} values are given in Table 4.5.

Table 4.5: Selected properties of the L30 proteins.

Protein	shielding[a]	stability[b] ΔG^{H_2O}, m	redox[c] E(Q/Q^{2-}), n
I17C	2.9	$34 \pm 3, 29 \pm 2$	$+205, 1.9 \pm 0.1$
L30Y	1.8	$11 \pm 1, 23 \pm 2$	$-105, 1.9 \pm 0.2$
L30H	2.2	$10 \pm 1, 15 \pm 2$	$-240, 2.1 \pm 0.5$

[a]Shielding as determined from Figure 4.10. The value here is the ratio K_{SV}(denatured I17C)/K_{SV}; [b]Guanidine denaturation of the Fe(III)-heme-bound protein from Figure 4.9. The values shown are in units of kJ mol^{-1} M^{-1}, ΔG^{H_2O}, and kJ mol^{-1} M^{-1}, cosolvation (m); [c]E_m (in mV) determined from the fit of Nernst curve to data in Figure 4.11.

Semiquinone

To better characterise the protein-bound quinone, the semiquinone was examined by absorbance. Initially the formation of semi-*p*BQ was observed at alkaline pH (Figure 4.12). As the pH is raised above ~7.5 *p*BQ forms relatively low yields of semiquinone anion. Above pH 9 the solution rapidly became brightly red coloured, obscurring the weak semiquinone absorbance. This red colour is characteristic of hydroxy-benzoquinone formation, so pH 9 was used as an upper-limit for these experiments. The formation of semiquinone in Figure 4.12 can be fit to a pK of about 9, but due to uncertainty in the maximal absorbance this is not very accurate. The semiquinone anion has a peak at 425-435 nm in water with ε ~7000 $M^{-1}cm^{-1}$ while the neutral semiquinone has a peak at 410-415 nm with ε ~5000 $M^{-1}cm^{-1}$ (Depew & Wan, 1988). Thus, the yield of semiquinone generation by alkalinisation is very low (< 1 %). The mechanism of the formation of the semiquinone is not certain. If there is a small hydroquinone contamination, the comproportion reaction (eqn 4.4) will generate some semiquinone. Additionally, as the pH is elevated k_{semi} increases and the semiquinone becomes more stable. It is possible that the quinone is also reduced by abstraction of an electron from a hydroxide radical (Depew & Wan, 1988):

$$Q + OH^- \rightarrow Q^{-\cdot} + OH^{\cdot}. \tag{4.10}$$

and this would explain the alkaline pH dependence. Interestingly, the neutral semiquinone radical was observed in a solution of hydroquinone at pH 9 (Figure 4.12). This is quite remarkable as pK($Q^{-\cdot}$/$QH^{\cdot}$) ~ 4. Similar amounts of the semiquinone anion were observed in solutions of *p*BQ and hydroquinone at pH 9 (Figure 4.12). This suggests that the major determinant of semiquinone concentration is probably k_{semi} rather than the mechanism of formation (which must be different for *p*BQ and hydroquinone). Whatever the mechanism of radical formation, the presence of the semi-*p*BQ anion in *p*BQ solutions at pH 9 allows a simple and easy method of radical generation free of other contaminating reagents.

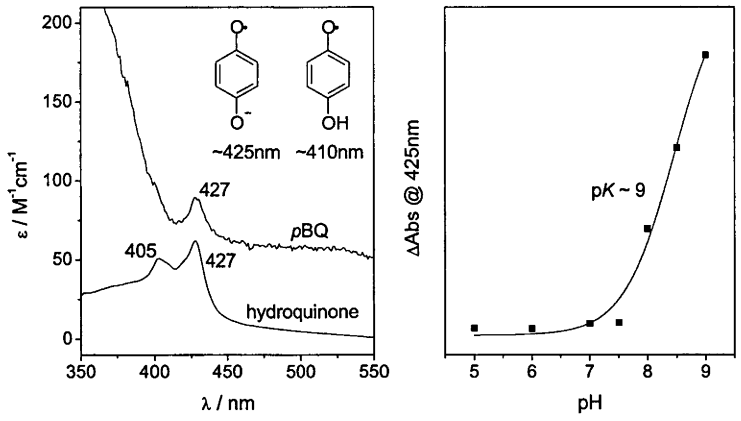

Figure 4.12: Left, The absorbance spectra of 1 mM *p*BQ and 1 mM hydroquinone at pH 9.0 showing the neutral and anionic semiquinone absorbance. Right, Generation of the *p*BQ semiquinone anion by raising the pH.

4.4 Quinone EPR

EPR offers a sensitive method of free radical measurement and this was employed to further characterise the semiquinone radicals. An analogous experiment to that shown in Figure 4.12 was performed by EPR and this is shown in Figure 4.13. The [semiquinone] vs pH dependence as measured by EPR is similar to that measured by absorbance. X-band EPR measurements were made at room temperature. The semiquinone radicals, like most organic radicals, have very long spin-lattice (T_1) relaxation times which results in their EPR spectra exhibiting narrow peaks even at room temperature (as opposed to the case of Fe(III)-heme EPR discussed in the previous chapter). Thus, changes in semiquinone EPR spectra can be resolved at room temperature and this technique was used to look at I17C-bound semiquinones.

The EPR spectra of *p*BQ and GS-*p*BQ at pH 9.0 are shown in Figure 4.14 a and b, respectively. The spectrum of semi-GS-*p*BQ is very different to that of *p*BQ. This species shows line broadening at relatively low magnetic power (power at half saturation, $P_{1/2}$ (Rupp *et al.*, 1978), = 5 mW) and the resultant broadened spectrum is shown in Figure 4.14 c on the same y scale as Figure 4.14 b. The resolved GS-*p*BQ spectrum

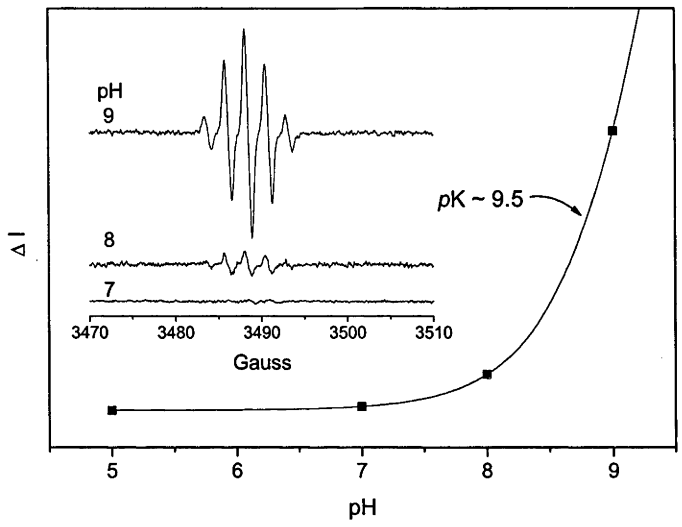

Figure 4.13: Generation of the *p*BQ semiquinone by raising the pH as measured by room temperature X-band EPR.

was simulated by Karin Ahrling and it cannot be fitted with less than three anisotropic interactions. As the cysteine-bound *p*BQ anion radical has a sulfur in place of one of the hydrogens it contains three non-equivalent hydrogens which account for these three anisotropic tensors. The EPR spectrum of I17C-*p*BQ at pH 9.0 is shown in Figure 4.14 d and is quite similar to that of GS-*p*BQ at high microwave power. This spectrum was acquired at 6.3 mW which is well below the measured $P_{1/2}$ of 15 mW. This relaxation (relative to $P_{1/2}$ = 5 mW in GS-*p*BQ) is probably caused by the protein matrix (Allen *et al.*, 1982).

The lines in the low-power GS-*p*BQ spectrum are very sharp, consistent with a very long T_1. The broadening at high microwave power is thought to then arise through T_2 processes causing inhomogeneous broadening rather than pure relaxation broadening. T_2 processes depend on the correlation time (τ_c) of the molecule, which in turn depends on the viscosity of the solution and the Bohr radius of the radical. In these experiments the radical is in the regime where $\omega_0\tau_c \gg 1$, where T_1 becomes much longer than T_2 and τ_c approaches that of a solid (Carrington & McLachlan, 1967). This is consistent with the observation that the hyperfine interactions in GS-*p*BQ are not absolutely symmetric

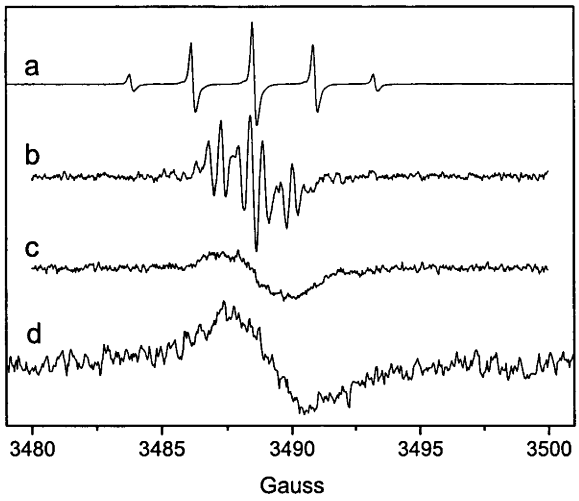

Figure 4.14: Room temperature X-band EPR spectra of (a) *p*BQ at 0.1 G modulation amplitude (MA); (b) GS-bound *p*BQ at 0.2 G MA, 6.3mW; (c) *p*BQ at 0.2 G MA, 80mW scaled relative to (b); (d) I17C-bound *p*BQ at 1.0 G MA, 6.3 mW. These samples were at pH 9.0 in 50 mM tris, 100 mM KCl.

indicating that the molecule is tumbling too slowly for the interactions to be averaged out. The I17C-*p*BQ spectrum is broadened and the individual peaks unresolved which could simply be due to a longer T_2 brought about by the slower tumbling of the much larger protein molecule. As I17C is obviously much larger than GSH this difference in τ_c and thus T_2 might account for the our inability to resolve the hyperfine interactions in I17C-*p*BQ at low microwave power.

The EPR spectra of the CoQ_0 semiquinone in solution and bound to I17C are shown in Figure 4.15. The 5 line spectrum of CoQ_0 in solution is consistent with reports for the semiquinone anion while the 4 line spectrum of I17C-bound CoQ_0 is similar to that reported for the glutathione-bound semi-CoQ_0 anion (Guo *et al.*, 2002). Unlike *p*BQ, the power-saturation behaviour of semi-CoQ_0 does not change upon binding to apo-I17C ($P_{1/2}$ of semi-CoQ_0 = 27 ± 1 mW, $P_{1/2}$ of semi-CoQo-I17C = 25 ± 2 mW). In semi-CoQ_0 the hyperfine splitting is dominated by the single hydrogen on the quinone ring. This is lost upon binding to the protein. There are 3 equivalent hydrogens (5-

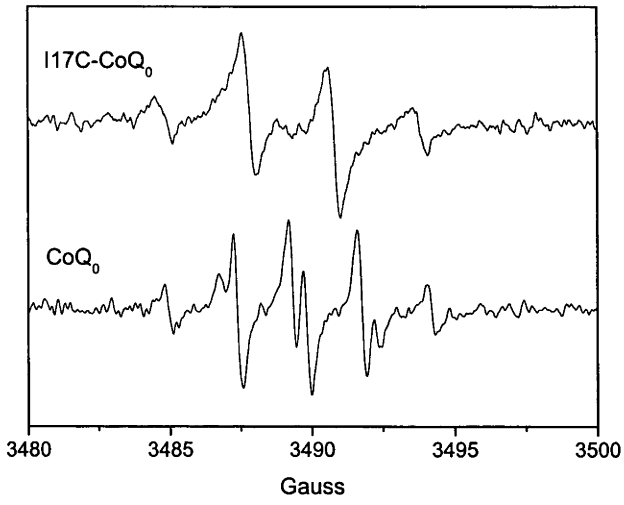

Figure 4.15: Room temperature X-band EPR of I17C-bound CoQ_0 and CoQ_0 at pH 9.0, 0.2 G modulation amplitude, 10 mW microwave power.

methyl) which also contribute to the hyperfine interactions and, as these interactions are relatively weak, the splitting is quite large. Thus, the spectra of the I17C-bound CoQ_0 semiquinone is reasonably well resolved despite the inhomogeneous broadening caused by the slow tumbling of the protein.

The EPR spectra of the L30H and L30Y-bound *p*BQ and CoQ_0 semiquinones are not measurably different to those of the I17C-bound quinones. Iodide quenching of I17C-bound hydroquinone at pH 9 (under the same buffer conditions as EPR was performed) gave a K_{SV} value similar to that of denatured I17C-*p*BQ-H_2 (Table 4.2). This suggests that increasing the pH from 7 to 9 causes some structural perturbation to the protein-quinone complex. If the quinone is no longer bound within the interior of the protein then the interactions between the quinone at residue 30 will be lost and thus the semiquinone in the I17C and L30 proteins would be expected to have similar EPR properties. Attempts to measure the $E(Q/Q^{-\cdot})$ values for the protein-bound quinones was abandoned as a result of this finding.

4.5 Summary

Quinones such as *p*BQ and CoQ_0 can bind to an engineered cysteine within the interior of the I17C mutant of cyt b_{562}. This quinone binding site is novel and we are not aware of any previous reports of a designed quinone-binding protein. The bound hydroquinone is partially shielded from the solvent and is not significantly destabilising to the ferri-protein. The bound quinone undergoes 2-electron oxidation/reduction at physiological pH and the semiquinone can be generated at pH 9. The EPR spectrum of I17C-bound semi-CoQ_0 is consistent with sulfur addition and similar to reported spectra of glutathione-bound CoQ_0. The L30 mutants of the cyt b_{562} I17C are significantly less stable than I17C yet still bind CoQ_0. The E_m of bound CoQ_0 in the L30 mutants is significantly lower than in I17C but the mechanisms by which this is achieved are not well understood.

This chapter merely represents the preliminary characterisation of a new quinoprotein. Considerable future work is required to better-characterise this system. The major focus of this work would involve: (*i*) measuring the $E(Q/Q^{-\cdot})$ values for protein bound quinones, perhaps by ultra-fast electrochemistry at pH 7; and (*ii*) collecting detailed structural information regarding the effect of quinone-binding on the protein structure, preferentially by X-ray crystallography which, unlike NMR, would also determine the structure of bound (un-labelled) cofactors (quinone and perhaps a bound porphyrin).

The following chapter describes the use of the bound quinone as an electron acceptor in light-induced ET reactions.

CHAPTER 5

Electron Transfer

The quinone-bound I17C and L30 proteins described in the previous chapter retain the heme binding site and can simultaneously bind a quinone and porphyrin. As shown in Chapter 3, cyt b_{562} and its mutants can be reconstituted with light-active chlorophyll analogues such as ZnPP and Zn-Ce_6. When the protein has both a light-active porphyrin and oxidised quinone bound (denoted porphyrin-I17C-quinone), light-induced ET is observed from the porphyrin to the quinone. Thus, this small porphyrin/quinone/protein complex can mimic the primary charge separation event of a pheophytin/quinone-type photosynthetic RC.

5.1 Singlet Electron Transfer: Mimicking a Reaction Centre

Both the apo-I17C and CoQ_0-bound I17C proteins can be reconstituted with the light-active chlorophyll analogue Zn-Ce_6. As the I17C protein contains the H63N mutation (described in Chapter 3), the only remaining histidine in I17C is at postion 102 and this histidine is one of the heme ligands within the binding pocket of the cyt. The binding of Zn-Ce_6 to apo-I17C is indistinguishable from H63N in terms of K_d (~25 nM) and absorbance maxima (the absorbance spectrum of Zn-Ce_6-I17C-CoQ_0 is shown in Figure 5.1). The absorbance spectra of Zn-Ce_6-I17C and Zn-Ce_6-I17C-CoQ_0 are indistinguishable suggesting there is no ground state coupling between the chlorin and quinone. However, the Zn-Ce_6 fluorescence intensity in Zn-Ce_6-I17C-CoQ_0 increases by ~20 % when the bound quinone is reduced with dithionite. This is shown in Figure 5.1 B. Thus, in Zn-Ce_6-I17C-CoQ_0 there is a ~20 % quenching of the chlorin fluorescence by the quinone if it is oxidised. The quenching could be either due to Förster energy transfer (the absence of ground-state coupling rules-out a Dexter mechanism, see Chapter 1.4) or ET. There is no detectable spectral overlap between the Zn-Ce_6 emission and quinone absorbance (J = 0) and as the quenching is only observed in the presence of the oxidised quinone, which is a classic electron acceptor, we favour the later explanation of ET. This is not unprecedented as early reports of porphyrin-quinone diads reported fluorescence quenching when the quinone was oxidised. This too was explained by an ET mechanism rather than energy transfer (see Chapter 1.8).

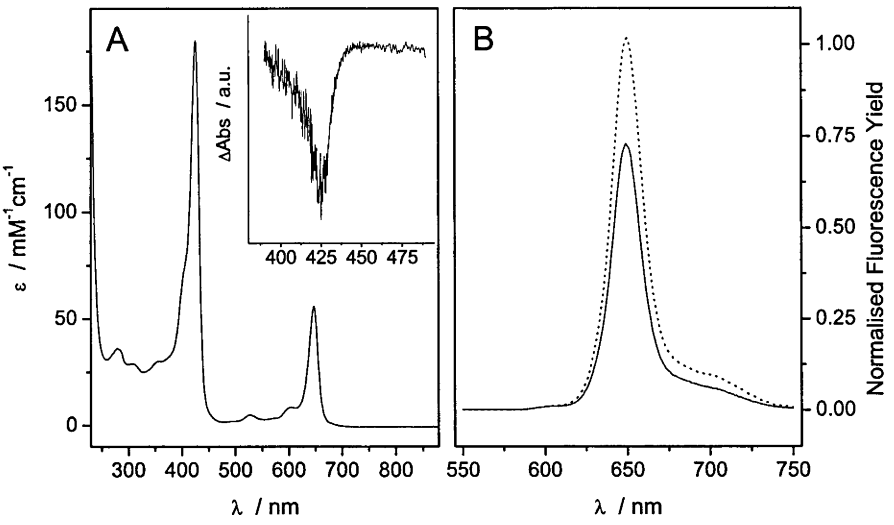

Figure 5.1: (A) Absorbance spectrum of Zn-Ce_6-I17C-CoQ_0 in 50 mM KP_i, 100 mM KCl, pH 7.0. The inset shows the Soret-region light-minus-dark absorbance spectrum of the of this complex (excitation at 650 nm). (B) Fluorescence emission spectra of Zn-Ce_6-I17C-CoQ_0 in the absence (solid line) and presence of sodium dithionite (dotted line) showing $\sim$ 20% quenching of the chlorin fluorescence by the oxidised quinone.

To further characterise the ET reaction in Zn-Ce_6-I17C-CoQ_0, light-induced absorbance changes were examined. The Soret-region light-minus dark absorbance difference spectrum is shown in the inset to Figure 5.1. The difference spectrum is not well resolved but can be explained by a loss of the chlorin $\pi \rightarrow \pi^*$ transition which occurs upon formation of a singlet, triplet or cation state. There is no detectable triplet absorbance at $\sim$460 nm and flash photolysis with a flash lamp ($\sim$ 5 μs flash) failed to resolve the kinetics of the Soret bleaching, which would be relatively slow if a triplet was formed. If there is light-induced ET from Zn-Ce_6 to the quinone in Zn-Ce_6-I17C-CoQ_0 then the chlorin cation and semi-quinone radicals should be detectable upon illumination. These radicals can be detected by EPR.

Under illumination Zn-Ce_6 forms a porphyrin π cation (Razeghifard & Wydrzynski, 2003) and this is shown in Figure 5.2 (a) for I17C-bound Zn-Ce_6. The EPR spectrum

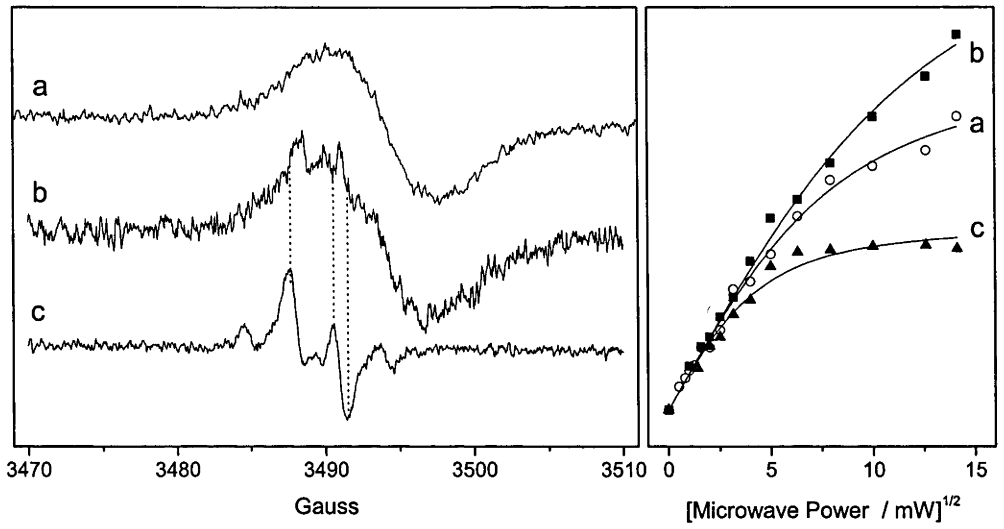

Figure 5.2: Left, Room temperature X-band light-minus dark EPR spectra of (a) Zn-Ce_6-I17C and (b) Zn-Ce_6-I17C-CoQ_0 at pH 7. I17C-CoQ_0 (no chlorin) at pH 9.0 is shown in (c). Note that the dotted lines demonstrate that spectrum (b) is a composite of (a) and (c). Right, progressive microwave power saturation of the spectra. The signal intensity is normalised (I/I_0 and the $P_{1/2}$ values are given in the text).

of Zn-Ce_6-I17C-CoQ_0 under illumination at pH 7 is also shown in this figure. In the dark there is no detectable EPR signal from this sample. The spectrum is a composite of the Zn-Ce_6 cation and semi-CoQ_0 and confirms that light-induced ET occurs from Zn-Ce_6 to CoQ_0. The power-saturation behaviour of the Zn-Ce6 cation changes in the presence of the bound semi-quinone with the $P_{1/2}$ increasing from 86 ± 4 to 198 ± 12 mW (Figure 5.2, right). This relaxation is likely due to the close proximity of the semi-quinone radical which is acting as a relaxer. The distance (r) between Zn-$Ce_6^{+\cdot}$ and the relaxer is related to the power-saturation relaxation (Abragam & Bleaney, 1986) by:

$$\Delta P_{1/2} \propto \frac{S^2}{r^6}, \tag{5.1}$$

where S is the spin of the relaxed radical, which in the case of Zn-$Ce_6^{+\cdot}$ is S = 1/2. In order to achieve a $\Delta P_{1/2}$ of >100 mW, r must be quite small. This is consistent with Figure 4.3 in the previous chapter, where the quinone is ~10 Å from the bound chlorin.

The light-induced ET kinetics in Zn-Ce_6-I17C-CoQ_0 where investigated using time-resolved EPR (TREPR) of the Zn-Ce_6 cation signal. Unfortunately both the forward and back reactions were not resolved due to instrument limitations, $\sim$20 μs resolution (data not shown). This explains why spectrum b in Figure 5.2 has poor signal-to-noise. The radicals (charge separated state) have a short lifetime and thus the signal measured is predominantly ground-state Zn-Ce_6-I17C-CoQ_0. This also hampers measurements of $P680^{+\cdot}$ in photosystem II (Miller & Brudvig, 1991). To prove that this is an instrument limitation, the light-induced ET from H63N-bound Zn-Ce_6 to CoQ_0 in solution was investigated by TREPR. In this case there will be a greater distance between the donor and acceptor and thus k_{ET} will be slower and the kinetics resolved. The charge separation was not resolved but the recombination kinetics were easily resolved (data not shown, $k_{CR} \sim 200\ s^{-1}$) demonstrating the utility of this method for measuring (relatively slow) light-induced ET.

To resolve the rate of the forward ET reaction in Zn-Ce_6-I17C-CoQ_0, the Zn-Ce_6 fluorescence lifetime was measured[1]. The measurements were made with a time-correlated single photon counting apparatus and ultrafast laser with picosecond resolution. The fluorescence lifetime of I17C-bound Zn-Ce_6 decreased in the presence of bound CoQ_0 from 3.01 to 2.42 ns (Figure 5.3). The rate of forward ET was calculated by $k_{ET} = \tau_{DA}^{-1} - \tau_D^{-1}$ to be 8.1 x 10^7 s^{-1} (12 ns lifetime). (τ_{DA} is the lifetime of Zn-Ce_6-I17C-CoQ_0, τ_D is the lifetime of Zn-Ce_6-I17C). If the bound CoQ_0 is subsequently reduced with dithionite the Zn-Ce_6 fluorescence lifetime increases to 3.07 ns as there is no ET to the bound hydroquinone. The efficiency of the ET reaction is $\sim$20 % (eqn 1.4) and in good agreement with steady state fluorescence quenching (Figure 5.1).

The effect of the driving force (ΔG^0) on this ET reaction was investigated by measuring the fluorescence decay kinetics of this system when CoQ_0 was substituted for several other *p*-benzoquinones. CoQ_0 was substituted with *p*BQ, 2,6-dichloro-*p*BQ, and 2,5- and 2,6-dimethyl-*p*BQ. The one-electron reduction potentials of these quinones spans >500 mV in water from -80 mV to +470 mV, yet only a $\sim$2.5 fold change in k_{ET} was observed (see Table 5.1). As discussed in Chapter 1, in Marcus theory $k_{ET} \propto$

[1]The fluorescence decay measurements were performed in collaboration with Dr Trevor Smith and Prof. Ken Ghiggino in the School of Chemistry, University of Melbourne

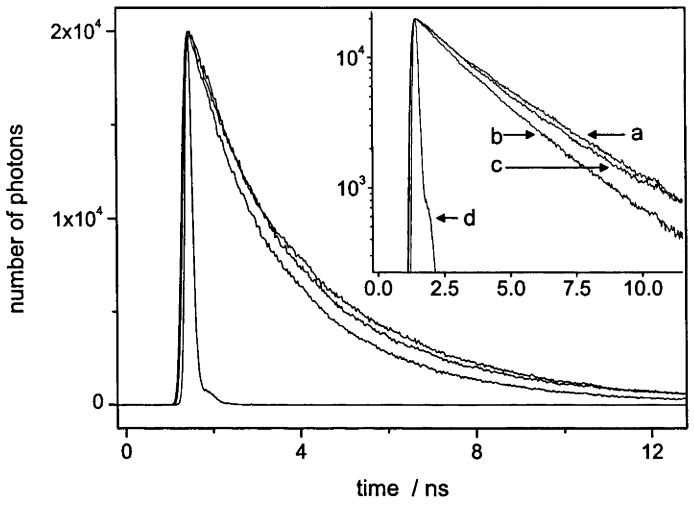

Figure 5.3: Zn-Ce_6 fluorescence decay curves for (a) Zn-Ce_6-I17C, (b) Zn-Ce_6-I17C-CoQ_0 and (c) dithionite-reduced Zn-Ce_6-I17C-CoQ_0. (d) is the instrument response. The lifetimes are given in Table 5.1.

$\exp[-(\Delta G^0 + \lambda)^2/\lambda]$ where λ is the reorganisation energy (reviewed in (Marcus & Sutin, 1985)). In the Zn-Ce_6-I17C-quinone system the electron is transfered from the excited state of Zn-Ce_6 which has an energy ($E_{0,0}$) of 1.91 eV (the average energy of the Q_Y absorbance band and fluorescence emission band (Marcus & Sutin, 1985)). The driving force can be approximated as:

$$\Delta G^0 = \Delta E - E_{0,0} \tag{5.2}$$

where ΔE is the difference between the oxidation potential of Zn-Ce_6 (E(Zn-Ce_6/Zn-$Ce_6^{+\cdot}$)) and the 1-electron reduction potential of the quinone (E($Q/Q^{-\cdot}$)). Attempts to measure the oxidation potential of I17C-bound Zn-Ce_6 were hampered by its apparently high value. The oxidation potential of Zn-Ce_6 will be similar to that of Zn-Chl *a* which is about +1.1 V (Watanabe & Kobayashi, 1991). Using the E($Q/Q^{-\cdot}$) values of the parent quinones in water (Table 5.1) and an oxidation potential of I17C-bound Zn-Ce_6 of +1.1 V, a range of ΔG^0 values from about -0.7 to -1.3 eV is calculated. The driving force is thus large and the small change in k_{ET} suggests that the ET reactions are occurring toward the top of a Marcus curve with a relatively large reorganisation en-

Table 5.1: Zn-Ce_6 Fluorescence lifetimes (τ), rates of electron transfer (k_{ET}) and estimated quinone 1-electron reduction potentials (E($Q/Q^{-\cdot}$)) and driving force (ΔG^0) values for some Zn-Ce_6-I17C-quinone and Zn-Ce_6-L30-quinone complexes

Protein Quinone	τ (ns)	k_{ET}[a] (s^{-1})	E($Q/Q^{-\cdot}$)[b] (mV)	ΔG^0 (eV)
I17C				
none	3.01	-	-	-
CoQ_0	2.42	8.1 x 10^7	-30[c]	-0.78
CoQ_0 reduced	3.07	0	-	-
DCBQ[d]	2.50	6.8 x 10^7	+470	-1.28
*p*BQ	2.47	7.3 x 10^7	+99	-0.91
2,5-DMBQ[d]	1.97	1.8 x 10^8	-66	-0.74
2,6-DMBQ[d]	2.18	1.3 x 10^8	-80	-0.73
L30Y				
CoQ_0	2.13	1.4 x 10^8	-	-
L30H				
CoQ_0	2.06	1.5 x 10^8	-	-

[a] Calculated from the fluorescence lifetime by $k_{ET} = \tau_{DA}^{-1} - \tau_D^{-1}$, see text and Chapter 1.4; [b] Reported values for the parent quinones in water at pH 7 taken from (Depew & Wan, 1988) and [c] described in the previous chapter.

ergy ($\lambda \sim 1$ eV). The k_{ET} values can be fit to Dutton's ruler (Moser & Dutton, 1992), an empirical Marcus curve relating k_{ET} to ΔG^0, λ, and the edge-to-edge cofactor distance in a protein. The fit is poor (data not shown), but yields $\lambda \sim 1$ eV and the distance between Zn-Ce_6 and $CoQ_0 \sim 11$ Å. This distance is in good agreement with the molecular model of Zn-Ce_6-I17C-*p*BQ shown in Figure 4.3.

The values from Table 5.1 were used to create an energy diagram describing the light-induced ET in Zn-Ce_6-I17C-CoQ_0, which is shown in Figure 5.4. The most obvious feature of this diagram is that ΔG^0 (forward) $\sim \Delta G^0$ (backward). This explains

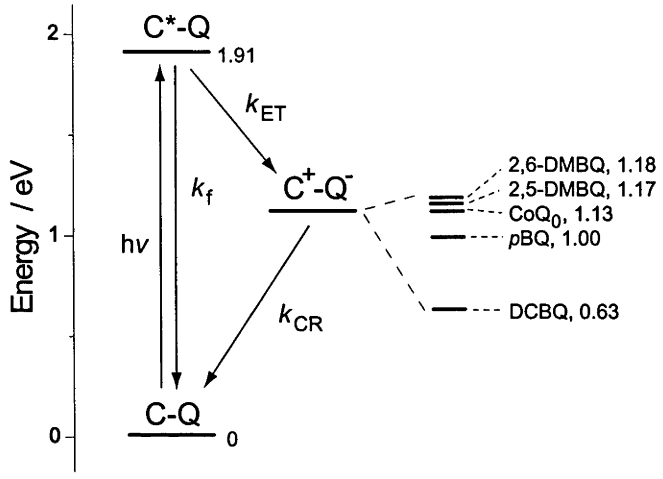

Figure 5.4: Energy levels of light-induced ET in Zn-Ce$_6$-I17C-quinone. C is Zn-Ce$_6$, and Q the quinone.

why the charge recombination kinetics were not resolved by TREPR as the back reaction is occurring near the top of the Marcus curve, probably at a similar rate to that of charge separation (ns timescale).

The L30 mutants described in the previous chapter (Chapter 4.3) were designed to tune the redox properties of the bound quinone. When bound to L30Y and L30H, CoQ_0 had a significantly lower $E(Q/Q^{2-})$ potential than when free in solution or bound to I17C. It is reasonable to assume (due to eqn 4.3) that a significant contribution to this difference in $E(Q/Q^{2-})$ is due to lower $E(Q/Q^{-\cdot})$ potentials in L30H-CoQ_0 and L30Y-CoQ_0 relative to I17C-CoQ_0. It would then be expected that k_{ET} in the L30 proteins would be different to that in I17C. The Zn-Ce$_6$ fluorescence decay kinetics were measured in Zn-Ce$_6$-L30Y-CoQ_0 and Zn-Ce$_6$-L30Y-CoQ_0 and the decay curves are shown in Figure 5.5 and the lifetimes and k_{ET} values given in Table 5.1. Despite the much lower $E(Q/Q^{2-})$ values, both of the L30-CoQ_0 complexes showed little change in k_{ET} relative to Zn-Ce$_6$-I17C-CoQ_0. This is perhaps more startling if one considers that a change in the edge-to-edge distance between Zn-Ce$_6$ and CoQ_0 from 11 to 12 Å should, according to Dutton's ruler (Moser & Dutton, 1992), change the maximal k_{ET} from 2.5 x 10^8 to 6.3 x 10^7 (eqn 1.18 with $\lambda = 1$ eV). This range is of similar magnitude to that observed across all the measurements made in this work. The guanidine denaturation and

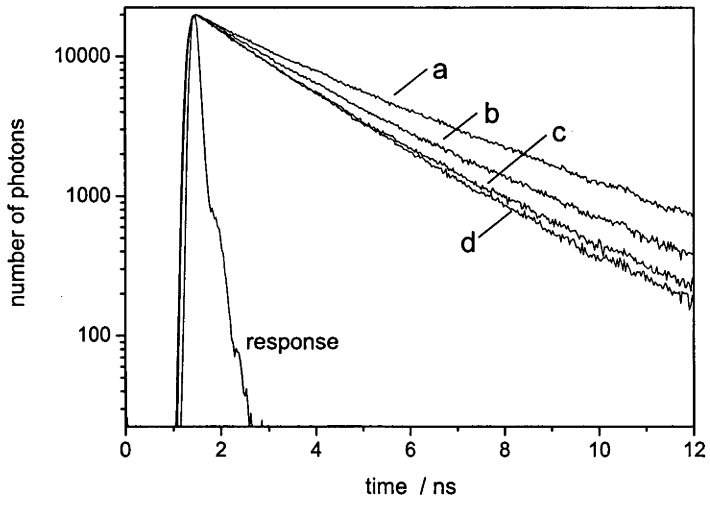

Figure 5.5: Fluorescence decay curves of (a) Zn-Ce_6-I17C; (b) Zn-Ce_6-I17CCoQ_0; (c) Zn-Ce_6-L30Y-CoQ_0; and (d) Zn-Ce_6-L30H-CoQ_0. Lifetimes are given in Table 4.5 and experimental conditions are identical to those in Figure 5.3.

iodide quenching experiments described in the previous chapter (see Table 4.5) demonstrated that the L30 mutations have destabilised, and possibly altered, the conformation of the quinone-protein complex. It is reasonable to expect that the L30 mutations may have perturbed the structure of the chlorin/protein/quinone complex in such a way as to alter the distance between the chlorin and quinone. However, any change in Zn-Ce_6-quinone distance should have caused a much more significant difference in k_{ET} between Zn-Ce_6-I17C-CoQ_0 and Zn-Ce_6-L30-CoQ_0 than was observed. Instead, the results suggest that: (*i*) The L30 mutations have not significantly perturbed the structure of the chlorin/protein/complex relative to I17C; (*ii*) The reorganisation energy is large in this ET reaction; and (*iii*) k_{ET} is relatively insensitive to the driving force in this the system. Detailed structural knowledge of each of the chlorin/protein/quinone complexes is needed to confirm that minimal structural perturbation has occurred across the mutants. It is also possible that the difference in $E(Q/Q^{-\cdot})$ throughout the different quinone complexes is much smaller than estimated here and thus $\Delta\Delta G^0$ is much smaller than expected.

The $E(Q/Q^{2-})$ values for I17C-*p*BQ and CoQ_0 bound to I17C, L30Y and L30H have been measured (Figure 4.11). Although ΔG^0 is related to $E(Q/Q^{-\cdot})$ not $E(Q/Q^{2-})$ there is, in some cases, a reasonably linear correlation between quinone 1- and 2-electron reduction potentials[2]. The relationship between measured $E(Q/Q^{2-})$ potentials and k_{ET} in Zn-Ce_6-protein-quinone complexes is shown in Figure 5.6. The solid line is:

$$k_{ET} = A - \left[(c[E(Q/Q^{2-}) - E_{offset}] + \lambda)^2/(k_B T\lambda)\right]. \quad (5.3)$$

There are several things to consider with regard to this figure: (*i*) The inverted region is to the left and there are not sufficient data points to accurately determine the $E(Q/Q^{2-})$ value at which k_{ET} is maximal. (*ii*) Whilst in some cases there is a linear correlation between $E(Q/Q^{-\cdot})$ and $E(Q/Q^{2-})$, it may not have a slope of 1. The c term in eqn 5.3 is set to 1 but could be adjusted to account for this. As the value of c is not known, the value of λ is not known. (*iii*) The $E(Q/Q^{2-})$ values were measured in the absence of Zn-Ce_6 and the presence of the bound chorin is likely to alter these potentials. However, this difference in potential is likely to be fairly constant across the different proteins and is then accounted for in the E_{offset} term and not of major concern. (*iv*) The change in k_{ET} is sufficiently small as to be possibly caused by minor perturbations to the quinone/protein structures rather than due to $\Delta\Delta G^0$. Nevertheless, there is a trend between the measured quinone redox properties, and thus ΔG^0, and k_{ET} which is consistent with Marcus theory.

It is quite possible that the L30 mutations will have some effect on the electronic coupling between Zn-Ce_6 and CoQ_0. If this is the case, this will then effect k_{ET} (eqn 1.14). The coupling in the Zn-Ce_6-protein-quinone systems was calculated using Beratan's pathways method (Beratan *et al.* (1987); Beratan & Onuchic (1996) and described in Chapter 1.4) implemented in HARLEM[3]. The coupling in Zn-Ce_6-I17C-CoQ_0, from the chlorin to the quinone, was calculated to be 100 μeV (0.8 cm^{-1}) and β = 1.3. The β value is slightly lower than the value of 1.4 determined by Moser & Dutton (1992) for protein ET in the BRC. This may be due to some through-bond ET in the

[2]The $E(Q/Q^{-\cdot})$ and $E(Q/Q^{2-})$ values for aqueous methyl-substituted 1,4-benzoquinones (Depew & Wan, 1988) fall on a straight line with a slope of $0.66E(Q/Q^{2-})$ per $E(Q/Q^{-\cdot})$.

[3]HARLEM was kindly provided by Igor Kurnikov. See Chapter 2

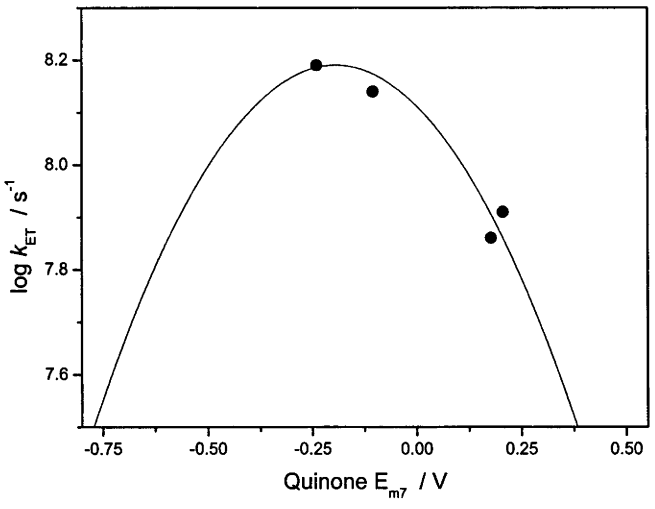

Figure 5.6: The relationship between k_{ET} in Zn-Ce_6-protein-quinone complexes and and the quinone 2-electron reduction potentials. The solid line is described in the text.

cyt or a more tightly-packed protein barrier. It may also reflect the degree of inaccuracy of this type of calculation. The H_{AB} and β values were fairly constant across different molecular models containing all the quinones used in this work. Using a H_{AB} value of 100 μeV, a Marcus curve incorporating the I17C data in Table 5.1 was constructed. This is shown in Figure 5.7 and the data fits this model fairly well. Thus, if the maximal k_{ET} in this protein is about 10^8 s^{-1}, and $\lambda \sim 1$ eV, then the coupling caluclated using the pathways method is surprisingly accurate. The coupling was also calculated in the L30H and L30Y Zn-Ce_6/CoQ_0 complexes. The coupling was calculated to be only slightly higher in these two systems. This is reasonable as a major determinant in this calculation is the donor/acceptor separation, which is very similar in the molecular models of I17C and the L30 proteins (Figure 4.8). There is a considerable degree of uncertainty in the accuracy of these models and both more accurate structural information and electronic coupling calculations are required to determine the effect the L30 mutations may have had on H_{AB}. One interesting finding from the pathways calculations was that the path of ET invariably went through Met 33. The ET pathway in Zn-Ce_6-I17C-CoQ_0 is shown in Figure 5.7. It would be interesting to investigate the

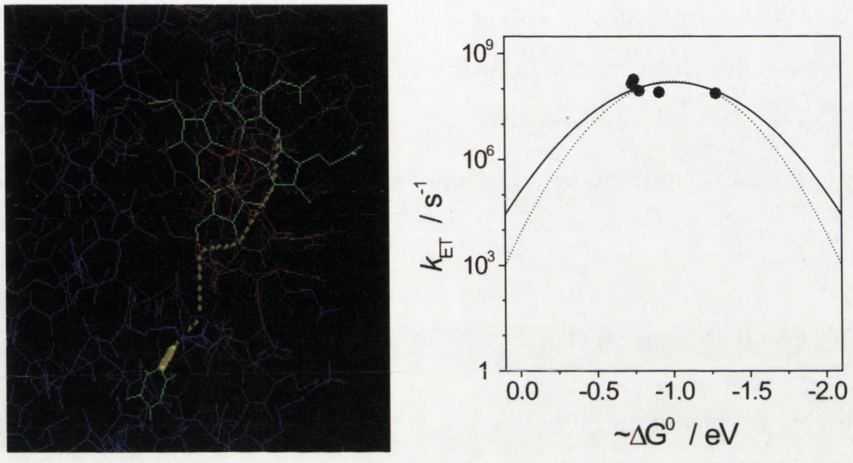

Figure 5.7: Electronic coupling in the Zn-Ce_6-I17C-quinone complexes. Left, the ET pathway (yellow) from the chlorin to quinone (green) in Zn-Ce_6-I17C-CoQ_0 calculated with HARLEM, see text for description. Right, ET vs. estimated ΔG^0. The solid line is a fit to Dutton's ruler with R = 11.3 Å, the dotted line a fit to eqn 1.15 with H_{AB} = 100 μV. Both models have λ = 1 eV.

coupling in this system by mutating Met 33, perhaps replacing it with Trp.

Despite our attempts to bury the quinone within the interior of the protein it appears that the reorganisation energy associated with the ET reaction is quite large ($\geq$ 1 eV). This is currently being evaluated[4] using continuum electrostatics calculations (as per the method of Sharp (1998)) and the solvent reorganisation energy has been estimated as $\sim$1.2 eV. The reorganisation energy associated with the reduction of the quinone has been estimated using standard quantum chemical techniques to be $\sim$0.3 eV and as changes in bond lengths in the chlorin are assumed to be negligible during chlorin oxidation, the total reorganisation energy is about 1.5 eV. It seems that cyt b_{562} is simply

[4]The reorganisation energy and electronic coupling is currently being calculated by Brett Wallace. This will be presented in a future manuscript.

too small to bury the cofactors far enough away from the solvent to prevent wide-spread solvent reorganisaton during the ET reaction. This would be reduced significantly if the protein was incorporated into a lipid membrane as is the case of the RCs. This would require the radical modification of cyt b_{562}, or the adoption of a new protein scaffold altogether. There has been some success by DeGrado (Lear *et al.*, 2001) in the *de novo*-design of α-helical peptides that associate in lipid membranes. Incorporation of the chlorin and quinone binding sites in similar petides may offer one future direction for this work which will result in a reduced λ and thus more typical ET behaviour for the primary charge separation.

5.2 Triplet Electron Transfer: A Long-Lived Charge Separated State

The efficiency of charge separation in the various Zn-Ce_6-I17C-quinone complexes is 15-35% (Table 5.1, eqn 1.4) but in order to harness this energy the charge separated state must be stabilised. Figure 5.4 suggests that the back reaction will occur near the top of the Marcus curve causing a short-lived charge separated state ($\tau < 20$ μs from TREPR data). Attempts to alter ΔG^0 and thus push the back reaction into the inverted region were largely unsuccessful. Another route, triplet ET, was explored to stabilise the charge separated state.

Upon light excitation, ZnPP (described in Chapter 3) forms a triplet state with near-unity efficiency ($\Phi_t = 0.9$) (Sudha *et al.*, 1984) which is long-lived ($\tau \sim 14$ ms) (Zemel & Hoffman, 1981; Sudha *et al.*, 1984). ET can occur from this triplet state which has a redox potential calculated by:

$$ZnPP^+/^3ZnPP^* = E(ZnPP^{+\cdot}/ZnPP) - E_T \qquad (5.4)$$

where $E(ZnPP^{+\cdot}/ZnPP)$ is the (ground state) oxidation potential of ZnPP (analogous to $E(Clz/Clz^{+\cdot})$) and E_T is the excited triplet energy. The excited triplet energy, which is similar to $E_{0,0}$ (described earlier), can be determined from the energy of ZnPP phosphorescence.

The room-temperature phosphorescence spectrum of I17C-bound ZnPP was deconvoluted from the fluorescence emission spectrum (Cowan & Gray, 1989) and is shown in Figure 5.8. The phosphorescence peak position ($\sim$720 nm) and E_T (1.72

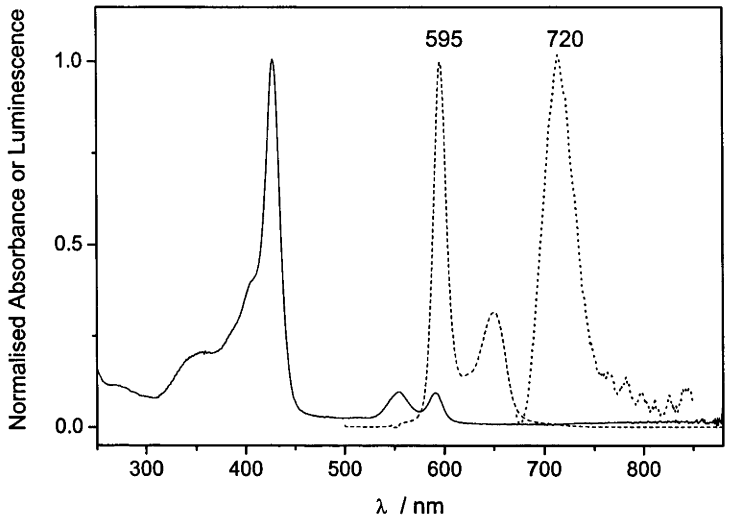

Figure 5.8: Absorbance, fluorescence and phosphorescence spectra of I17C-bound ZnPP.

Table 5.2: Reported oxidation potentials of Zn-substituted hemoproteins

Zn-Protein	$E(P/P^{+\cdot})$ (V)	E_T (eV)	$E(P^{+\cdot}/^3P^*)$ (eV)	reference
HRP[a]	0.75			Kaneko *et al.* (1980)
cyt *c*	0.80	1.68	-0.88	Magner & McLendon (1989)
myoglobin	0.98	1.78	-0.80	Cowan & Gray (1989)
I17C	0.85[b]	1.72	-0.87	this work

$E(P/P^{+\cdot}) = E(ZnPP/ZnPP^{+\cdot})$, $E(P^{+\cdot}/^3P^*) = E(ZnPP^{+\cdot}/^3ZnPP^*)$ calculated from eqn 5.4. [a]horseradish peroxidiase; [b]the average value was used.

eV) are in good agreement with previous reports (Table 5.2). Attempts to measure $E(ZnPP^+/ZnPP)$ for the ZnPP-I17C complex were unsuccessful. The average value for reported protein-bound ZnPP oxidation potential is 0.85 V (Table 5.2) and this value will be used for subsequent calculations.

The E_T and estimated $E(ZnPP^{+\cdot}/^3ZnPP^*)$ values were used to construct an energy

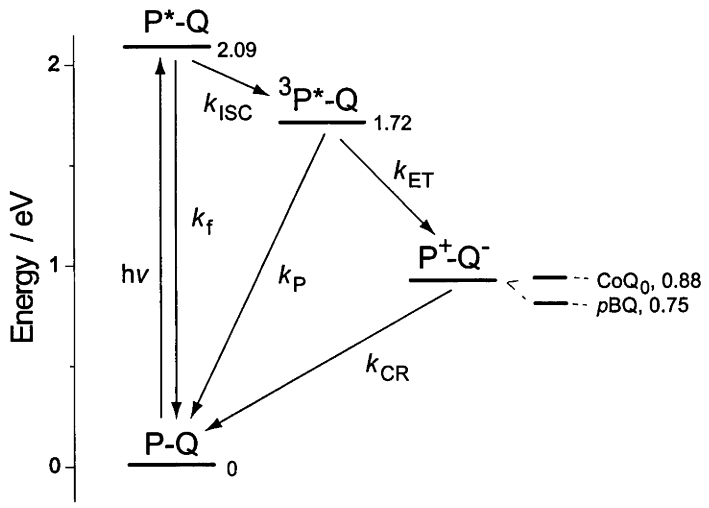

Figure 5.9: Energy levels of light-induced triplet-ET in ZnPP-I17C-quinone complexes.

level digram of light-induced ET in ZnPP-I17C-quinone complexes. This is shown in Figure 5.9. The relevant E(Q/Q$^{-\cdot}$) values in Table 5.1 where also used. These energies are only as accurate as the estimates for the E(ZnPP/ZnPP$^{+\cdot}$) and E(Q/Q$^{-\cdot}$) potentials.

Figure 5.9 assumes that there is no singlet ET to the quinone. Protein-bound ZnPP has a fluorescence lifetime of ~2.4 ns (Bellelli *et al.*, 1996). If singlet ET occurs on a similar time-scale as in the Zn-Ce$_6$-I17C-quinone complexes (8 x 10^7 s^{-1}) then a single ET efficiency of 20% is expected (eqn 1.4). However, as Φ_t = 0.9 (Sudha *et al.*, 1984), the efficiency of singlet ET is actually more like 2% and thus can be largely ignored.

The triplet ET is generally slower than singlet transfer, often occurring on the μs to ms times-scale (Qin & Kostic, 1994; Bellelli *et al.*, 1996; Fahnenschmidt *et al.*, 2001). This is amenable to measurement by TREPR when the porphyrin cation formation is monitored. The ZnPP triplet could also be measured by EPR but this would require very different experimental conditions and instrument parameters (Fahnenschmidt *et al.*, 2001). The room temperature EPR spectra of the I17C-bound ZnPP cation radical is shown in Figure 5.10 B. This was generated by illumination of ZnPP-I17C under aerobic conditions. If the oxygen is removed from the system, by the addition of glucose oxidase and catalase, no signal is observed. The ZnPP triplet state is sufficiently energetic to reduce molecular oxygen and this is the most likely electron acceptor in

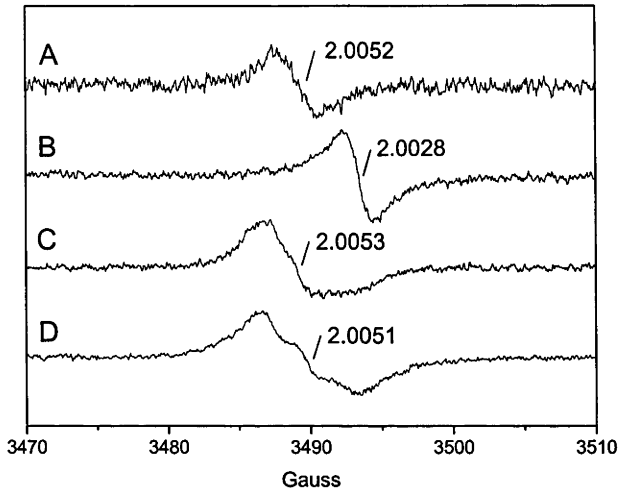

Figure 5.10: Room temperature X-band EPR spectra of (A) I17C-bound *p*BQ, pH 9.0 at 1 G MA, 6.3 mW; (B) I17C-bound ZnPP light-minus-dark, pH 7.0, 80 mW; (C) ZnPP-I17C-*p*BQ light-minus dark, pH 7.0, 6.3 mW; (D) ZnPP-I17C-*p*BQ light-minus dark, pH 7.0, 80 mW.

this reaction. The I17C-bound $ZnPP^{+\cdot}$ spectrum is consistent with a previous report of HRP-bound $ZnPP^{+\cdot}$ (Kaneko *et al.*, 1980). The reported spectrum was collected at 10 G modulation amplitude which will broaden the signal. The spectrum in Figure 5.10 is narrower (peak-to-peak) than that of Kaneko *et al.* (1980), but as the spectrum of $ZnPP^{+\cdot}$-I17C was recorded at 1 G modulation amplitude this is to be expected. The EPR spectra of ZnPP-I17C-*p*BQ under illumination is shown in Figure 5.10 C and D. There was no signal from this sample in the dark and the spectra were acquired in the presence of glucose oxidase and catalase. Superficially these spectra are composites of the protein bound ZnPP cation and semiquinone, but are broadened, probably due to spin-spin relaxation between the porphyrin cation and semiquinone.

The light-induced ET in ZnPP-I17C-*p*BQ and ZnPP-I17C-CoQ_0 was futher characterised by TREPR. This is shown in Figure 5.11 for the *p*BQ complex. This experiment measures the formation and decay of the porphyrin cation radical. The lifetimes are given in Table 5.3. The rate of forward ET is related to the lifetime of the charge

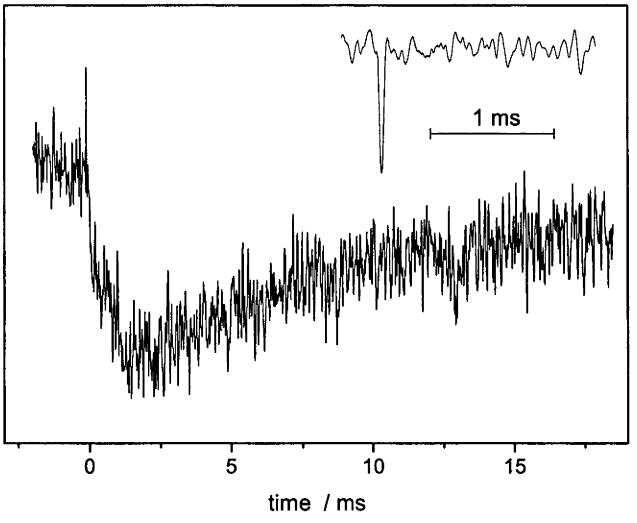

Figure 5.11: Time-resolved EPR of ZnPP-I17C-*p*BQ, pH 7.0, 80 mW, measured at 3495 G, 1 G MA, average of 5000 scans. The inset shows an analogous experiment performed with 200 μM ZnPP and *p*BQ in solution.

separation (see Figure 5.9) by:

$$\tau(\mathrm{CS}) = \frac{1}{\mathrm{k_{ISC}} + \mathrm{k_{ET}}}. \tag{5.5}$$

In the ZnPP-I17C-quinone complexes k_{ET} can be estimated quite accurately. k_{ISC} must be very fast[5], so if k_{CS} occurs on the μs time-scale, such as the case with the EPR data presented in Table 5.3, $\tau(\mathrm{CS}) \cong \tau(\mathrm{ET})$ and $k_{\mathrm{CS}} \cong k_{\mathrm{ET}}$. Thus, by substituting ZnPP for Zn-Ce_6 in this system we have slowed the rate of forward ET by 5 orders of magnitude and the rate of charge recombination by at least 3 orders of magnitude. The lifetime of the charge recombination[6] is 15 ms, long enough to couple the the charge separation to useful secondary chemistry.

[5]Assuming no internal conversion from S_1 (as in eqn 5.5), τ (fluorescence) = 2.4 ns and Φ_t = 0.9, τ (ISC) = 0.24 ns and $k_{\mathrm{ISC}} = 4.2 \times 10^9\ \mathrm{s}^{-1}$.

[6]In a rather uncanny coincidence the lifetime of charge recombination of the ZnPP cation in these two complexes is nearly identical to that of the reported triplet state lifetime. I am confident that this is the cation rather than the triplet due the properties of the EPR spectrum.

Table 5.3: Electron transfer in ZnPP-I17C-quinone complexes.

Quinone	E(Q/Q$^-$) (mV)	τ (CS) (μs)	k_{CS} (s^{-1})	ΔG^0 (eV)	τ (CR) (ms)	k_{CR} (s^{-1})	ΔG^0 (eV)
*p*BQ	+99	600	1.7 x 10^3	-0.97	15	67	-0.75
CoQ_0	-30	200	5.0 x 10^3	-0.84	15	67	-1.88

k_{CS} and k_{CR} are the rate of charge separation and recombination, respectively.

5.3 Summary and Future Work

I have demonstrated light-induced ET from a chlorin/porphyrin to a quinone in an engineered multi-cofactor protein. The rate of electron transfer reactions observed span 6 orders of magnitude (about 10 ns to 10 ms). The mechanism of ET can be determined from the choice of cofactors, occurring from either the singlet state (chlorin) or triplet state (porphyrin). We have a working model of the primary charge separation in a reaction centre. By using a protein scaffold it is now possible to investigate the role of the protein in a type of ET reaction previously only studied in organic molecules or large natural RCs.

CHAPTER 6

Conclusions and Future Work

A minimalistic model of a pheophytin-quinone type photosynthetic reaction centre would comprise a (B)Chl dimer, a pheophytin, 2 quinones linked via a non-heme iron (although ET can occur in RCs with the iron removed), and an un-specified electron donor. The cofactor separation would all be about 10 Å, and the cofactors would be bound to a membrane-spanning complex. This complex, described in Chapter 1, would be capable of vectorial ET upon illumination and form a long-lived charge separated state. The goal of this thesis has been to create small, minimalistic proteins to mimic aspects of the pheophytin-quinone reaction centres.

As the first step, protocols for the binding of Chl and Chl-analogues (porphyrins) to simple peptides and small proteins were developed and analysed (Chapter 3). Apo-cyt b_{562} could be reconstituted with a single porphyrin, while multiple porphyrins could be bound to a single *de novo*-designed peptide. The multiple porphyrins did not bind in a conformation where they are significantly excitonically-coupled as is the case of the "special pair" found in natural reaction centres. This is not a major problem as a simple reaction centre mimic does not require a light-harvesting antennae and thus a low-energy primary electron donor.

In the next step, a novel quinone-binding protein was developed (Chapter 4) and to our knowledge, is the first report of a designed quinone-binding protein. Small benzoquinones such as *p*BQ and CoQ_0 were bound to an engineered cysteine within the interior of a mutant of cyt b_{562}. The bound quinone is partially shielded from the solvent and is not significantly destabilising to the ferri-protein. At neutral pH, the bound quinone undergoes a 2-electron oxidation/reduction and the redox potential of this reaction can be tuned over a range of 300 mV by introducing specific protein-quinone interactions (L30 mutations). The bound semiquinone can be generated at pH 9 and the EPR spectrum of protein-bound semi-CoQ_0 is consistent with sulfur addition and similar to reported spectra of glutathione-bound CoQ_0.

The bound semiquinone can be generated in a light-induced electron transfer from a chlorin or porphyrin ((B)Chl analogue) bound within the cyt b_{562} heme-binding pocket (Chapter 5). The rate of electron transfer reactions observed span 6 orders of magni-

tude (about 10 ns to 10 ms) depending on cofactors selected. The mechanism of ET can be determined from the choice of cofactors, occurring from either the singlet state (chlorin) or triplet state (porphyrin). The excited state chlorin and porphyrin create a high-driving-force, allowing the electron transfer to occur near the top of the Marcus curve. Additionally, the chlorin and quinone appear to be quite strongly electronically coupled. The reorganisation energy of the chlorin to quinone electron transfer reaction appears to be $\geqslant 1$ eV, a downfall of using a small, soluble protein.

We have created a working model of the primary charge separation in a reaction centre. By using a protein scaffold it is now possible to investigate the role of the protein in an ET reaction previously only studied in organic molecules or large natural reaction centres. The (triplet) ET reaction from the bound porphyrin to quinone creates a charge separated state of about 15 ms. A long-lived charge separated state is a hallmark of natural photosystems.

As mentioned previously, the next step in this research would to solve the structure of the quinone-bound cyt. The M7H study would be complemented by a structure of that mutant also. Once the structural consequences of quinone binding to the cyt is established, the next step would be to add an additional redox-active cofactor to the I17C proteins. An electron donor to allow vectorial electron transfer would be the best option. In particular, by introducing a metal-binding site in the large loop between helices two and three in the quinone-binding mutants of cyt b_{562}, it would be possible to mimic photosystem II. An alternative approach, using the accumulated knowledge of heme binding (Chapter 3), would involve the introduction of a heme-binding site near the bound porphyrin. This would then create a bacterial reaction centre mimic. The metal-binding domain would be quite challenging to design as it could have no cysteine ligands and preferably no histidines. On the other hand, it is relatively easy to create selective heme and penta-coordinate porphyrin binding sites. Heme will much more readily bind to a *bis*-histidine motif, allowing subsequent chlorin binding to a single histidine. Instead of a metal centre, a histidine could be added near the porphyrin in the cyt b_{562} mutants and exogenous manganese used as an electron donor to photo-oxidised tyrosine in a four-step electron transfer reaction. In other directions, it may be possible to create multiple quinone-binding proteins, and/or mimic the non-heme iron site of

the pheophytin-quinone reaction centres. I cannot foresee any reaction in the natural reaction centres that would not be amenable to study by the approaches used in this thesis. Getting them all to work together of course may take a billion years.

References

Abragam, A. & Bleaney, B. (1986). *Electron paramagnetic resonance of transition ions*. Dover Publications Inc., Mineola, N.Y.

Ahmad, I., Cusanovich, M. & Tollin, G. (1981). Laser flash photolysis studies of electron transfer between semiquinone and fully reduced free flavins and horse heart cytochrome *c*. *Proc. Natl. Acad. Sci. USA.* **78**, 6724–6728.

Allen, J., Colvin, J., Stinson, D., Flynn, C. & Stapleton, H. (1982). Protein conformation from electron spin relaxation data. *Biophys. J.* **38**, 299–310.

Allen, J. & Williams, J. (1995). Relationship between the oxidation potential of the bacteriochlorphyll dimer and electron transfer in photosynthetic reaction centers. *J. Bioenerg. Biomembr.* **27**, 275–283.

Allen, J. & Williams, J. (1998). Photosynthetic reactions centres. *FEBS Lett.* **438**, 5–9.

Allen, J. P., Feher, G., Yeates, T., Komiya, H. & Rees, D. (1988). Structure of the reaction center from *Rhodobacter sphaerodides* r-26: Protein-cofactor (quinones and fe^{2+}) interactions. *Proc. Natl. Acad. Sci. USA.* **85**, 8487–8491.

Allen, J. P., Feher, G., Yeates, T., Rees, D., Deisenhofer, J., Michel, H. & Huber, R. (1986). Structural homology of reaction centers from *Rhodopseudomonas sphaeroides* and *Rhodopseudomonas viridis* as determined by x-ray diffraction. *Proc. Natl. Acad. Sci. USA.* **83**, 8589–8593.

Altuve, A., Silchenko, S., Lee, K.-H., Kuczera, K., Terzyan, S., Zhang, X., Benson, D. & Rivera, M. (2001). Probing the differences between rat liver outer mitochondrial membrane cytochrome *b*5 and microsomal cytochromes *b*5. *Biochemistry* **40**, 9469–9483.

Arnesano, F., Banci, L., Bertini, I., Faraone-Mennella, J., Rosato, A., Barker, P. & Fersht, A. (1999). The solution structure of oxidized *Escherichia coli* cytochrome *b*562. *Biochemistry* **38**, 8657–8670.

Arnold, F. & Volkov, A. (1999). Directed evolution of biocatalysts. *Curr. Opin. Chem. Biol.* **3**, 54–59.

Baltzer, L., Nilsson, H. & Nilsson, J. (2001). De novo design of proteins - what are the rules? *Chem. Rev.* **101**, 3153–3163.

Barker, P., Butler, J., DeOliveira, P., Hill, H. & Hunt, N. (1996). Direct electrochemical studies of cytochromes *b*562. *Inorg. Chim. Acta.* **252**, 71–77.

Barker, P., Ferrer, J., Mylrajan, M., Loehr, T., Feng, R., Konishi, Y., Funk, W., MacGillivray, R. & Mauk, A. (1993). Transmutation of a heme protein. *Proc. Natl. Acad. Sci. USA.* **90**, 6542–6546.

Barker, P., Nerou, E., Cheesman, M., Thomson, A., de Oliveira, P. & Hill, H. (1996). *Bis*-methionine ligation to heme iron in mutants of cytochrome *b*562. 1. spectroscopic and electrochemical characterization of the electronic properties. *Biochemistry* **35**, 13618–13626.

Bellelli, A., Brzezinski, P., Arese, M., Cutruzzola, F., Silvestrini, M. & Brunori, M. (1996). Electron transfer in zinc-reconstituted nitrite reductase from *Pseudomonas aeruginosa*. *Biochem. J.* **319**, 407–410.

Bendall, D. S. ed. (1996). *Protein Electron Transfer*. BIOS Scientific Publisher Ltd, Oxford.

Beratan, D. & Onuchic, J. (1996). in *Protein Electron Transfer,* Bendall, D. S. ed., chapter 2, pp. 23–42. BIOS Scientific Publisher Ltd, Oxford.

Beratan, D., Onuchic, J. & Hopfield, J. (1987). Electron tunneling through covalent and noncovalent pathways in proteins. *J. Chem. Phys.*, **86**, 4488–4498.

Bixler, J., Bakker, G. & McLendon, G. (1992). Electrochemical probes of protein folding. *J. Am. Chem. Soc.*, **114**, 6938–6939.

Bjerrum, M., Casimiro, D., Chang, I., Di Bilio, A., Gray, H., Hill, M., Langen, R., Mines, G., Skov, L., Winkler, J. & Wuttke, D. (1995). Electron transfer in ruthenium-modified proteins. *J. Bioenerg. Biomembr.*, **27**, 295–2930.

Bolton, J. & Mataga, N. McLendon, G. (1991). *Electron transfer in inorganic, organic, and biological systems*. ACS Adv. Chem. Ser. 228, American Chemical Society, Washington, D.C.

Brunmark, A. & Cadenas, E. (1989). Redox and addition chemistry of quinoid compounds and its biological implications. *Free Radic. Biol. Med.* **7**, 435–477.

Bullock, P. & Myer, Y. (1978). Circular dichroism and resonance raman studies of cytochrome *b*562 from *Escherichia coli*. *Biochemistry* **17**, 3084–3091.

Caffrey, M. & Cusanovich, M. (1994). Site-specific mutagenesis studies of cytochromes *c*. *Biochim. Biophys. Acta,* **1187**, 277–288.

Carrington, A. & McLachlan, A. (1967). *Introduction to magnetic resonance*. Harper and Row, New York.

Chambers, J. (1988). in *The chemistry of the quinonoid compounds*, Patai, S. & Rappoport, Z. eds., vol. 2, chapter 12, pp. 719–759. John Wiley and Sons.

Chang, I.-J., Gray, H. & Winkler, J. (1991). High-driving-force electron transfer in metalloproteins: Intramolecular oxidation of ferrocytochrome *c* by ru(2,2'-bpy)$_2$(im)(his-33)$^{3+}$. *J. Am. Chem. Soc.*, **113**, 7056–7057.

Chen, I.-P., Mathis, P., Koepke, J. & Michel, H. (2000). Uphill electron transfer in the tetraheme cytochrome subunit of the *Rhodopseudomonas viridis* photosynthetic reaction center: Evidence from site-directed mutagenesis. *Biochemistry*, **39**, 3592–3602.

Cheung, E., Taylor, K., Kornblatt, J., English, A., McLendon, G. & Miller, J. (1986). Direct measurements of intramolecular electron transfer rates between cytochrome *c* and cytochrome *c* peroxidase: Effects of exothermicity and primary sequence on rate. *Proc. Natl. Acad. Sci. USA.*, **83**, 1330–1333.

Cheung, M., Daizadeh, I., Stuchebrukhov, A. & Heelis, P. (1999). Pathways of electron transfer in *Escherichia coli* DNA photolyase: Trp306 to FADH. *Biophys J.*, **76**, 1241–1249.

Choma, C., Lear, J., Nelson, M., Dutton, P., Robertson, D. & DeGrado, W. (1994). Design of a heme-binding four-helix bundle. *J. Am. Chem. Soc.*, **116**, 856–865.

Chothia, C. (1974). Hydrophobic bonding and accessible surface area in proteins. *Nature.*, **248**, 338–339.

Clarke, W. (1960). *Oxidation-reduction potentials of organic systems*. Bailliere, Tindall and Cox, LTD.

Cogdell, R., Isaacs, N., Freer, A., Howard, T., Gardiner, A., Prince, S. & Papiz, M. (2003). The structural basis of light-harvesting in purple bacteria. *FEBS Lett.* **555**, 35–39.

Cowan, J. & Gray, H. (1989). Synthesis and properties of metal-substituted myoglobins. *Inorg. Chem.* **28**, 2074–2078.

Cristian, L., Piotrowiak, P. & Farid, R. (2003). Mimicking photosynthesis in a computationally designed synthetic metalloprotein. *J. Am. Chem. Soc.* **125**, 11814–11815.

Davis, C., Bustamante, P., Todd, J., Parkes-Loach, P., McGlynn, P., Olsen, J., McMaster, L., Hunter, C. & Loach, P. (1997). Evaluation of structure-function relationships in the core light-harvesting complex of photosynthetic bacteria by reconstitution with mutant polypeptides. *Biochemistry* **36**, 3671–3679.

DeGrado, W., Summa, C., Pavone, V., Nastri, F. & Lombardi, A. (1999). *De novo* design and structural characterisation of proteins and metalloproteins. *Annu. Rev. Biochem.* **68**, 779–819.

Deisenhofer, J., Epp, O., Miki, K., Huber, R. & Michel, H. (1985). Structure of the protein subunits in the photosynthetic reaction centre of *Rhodopseudomonas viridis* at 3 Å resolution. *Nature.* **318**, 618–624.

Depew, M. & Wan, J. (1988). in *The chemistry of the quinonoid compounds*, Patai, S. & Rappoport, Z. eds., vol. 2, chapter 16, pp. 899–962. John Wiley and Sons.

DeVault, D. & Chance, B. (1966). Studies of photoynthesis using a pulsed laser. i. temperature dependence of cytochrome oxidation rate in *Chromatium*. evidence for tunneling. *Biophys. J.*, **6**, 825–847.

DeVault, D., Parkes, J. & Chance, B. (1967). Electron tunnelling in cytochromes. *Nature.*, **215**, 642–624.

Di Bilio, A., Crane, B., Wehbi, W., Kiser, C., Abu-Omar, M., Carlos, R., Richards, J., Winkler, J. & Gray, H. (2001). Properties of photogenerated tryptophan and tyrosyl radicals in structurally characterized proteins containing rhenium(I) tricarbonyl diimines. *J. Am. Chem. Soc.*, **123**, 3181–3182.

Dickerson, R. & Timkovich, R. (1970). in *The Enzymes,* Hackney, D. & Tamanoi, F. eds., vol. 11, pp. 397–549. Academic Press, New York, 3rd edition.

Diner, B. & Rappaport, F. (2002). Structure, dynamics and energetics of the primary photochemistry of photosystem II of oxygenic photosynthesis. *Annu. Rev. Plant Biol.*, **53**, 551–580.

Dudkowiak, A., Kusumi, T., Nakamura, C. & Miyake, J. (1999). Chlorophyll *a* aggregates stabilized by a synthesized peptide. *J. Photochem. Photobiol. A, Chem.*, **129**, 51–55.

Dudkowiak, A., Nakamura, C., Arai, T. & Miyake, J. (1998). Interactions of chlorophyll a with synthesized peptide in aqueous solution. *J. Photochem. Photobiol. B.*, **45**, 43–50.

Durham, B., Pan, L., Long, J. & Millett, F. (1989). Photoinduced electron-transfer kinetics of singly labeled ruthenium bis(bipyridine) dicarboxybipyridine cytochrome *c* derivatives. *Biochemistry*, **28**, 8659 – 8665.

Dutton, P. (1978). Redox potentiometry: Determination of midpoint potentials of oxidation-reduction components of biological electron-transfer systems. *Methods Enzymol.*, **54**, 411–435.

Dutton, P., Leigh, J. & Wraight, C. (1973). Direct measurement of the midpoint potential of the primary electron acceptor in *Rhodopseudomonas spheroides* in situ and in the isolated state: Some relationships with pH and o-phenanthroline. *FEBS Lett.*, **36**, 169–173.

Dwyer, M., Looger, L. & Hellinga, H. (2004). Computational design of a biologically active enzyme. *Science.*, **304**, 1967–1971.

Eaton, W. & Hochstrasser, R. (1967). Electronic spectrum of single crystals of ferricytochrome-*c*. *J. Phys. Chem.*, **46**, 2533–2539.

Eggink, L. & Hoober, J. (2000). Chlorophyll binding to peptide maquettes containing a retention motif. *J. Biol. Chem.*, **275**, 9087–9090.

Fahnenschmidt, M., Bittl, R., Schlodder, E., Haehnel, W. & Lubitz, W. (2001). Characterization of *de novo* synthesized four-helix bundle proteins with metalloporphyrin cofactors. *Phys. Chem. Chem. Phys.*, **3**, 4082–4090.

Feng, Y. & Sligar, S. (1991). Effect of heme binding on the structure and stability of *Escherichia coli* apocytochrome *b*562. *Biochemistry*, **30**, 10150–10155.

Ferreira, K., Iverson, T., Maghlaoui, K., Barber, J. & Iwata, S. (2004). Architecture of the photosynthetic oxygen-evolving center. *Science.*, **303**, 1831–1838.

Fisher, N. & Rich, P. (2000). A motif for quinone binding sites in respiratory and photosynthetic systems. *J. Mol. Biol.*, **296**, 1153–1162.

Furukawa, Y., Ishimori, K. & Morishima, I. (2000). Electron transfer reactions in Zn-substituted cytochrome p450cam. *Biochemistry*, **39**, 10996–11004.

Gadsby, P., Peterson, J., Foote, N., Greenwood, C. & Thomson, A. (1987). Identification of the ligand-exchange process in the alkaline transition of horse heart cytochrome *c*. *Biochem. J.*, **246**, 43–54.

Gamow, G. (1928). Zur quantum theories des atom kernes. *Z. Phys.*, **51**, 204–212.

Ghiggino, K. P. & Smith, T. A. (1993). Dynamics of energy migration and trapping in photoirradiated polymers. *Prog. React. Kin.*, **18**, 375–436.

Gibney, B. & Dutton, P. (1999). Histidine placement in *de novo* -designed heme proteins. *Protein Sci.*, **8**, 1888–1898.

Gibney, B. & Dutton, P. (2001). *De novo* design and synthesis of heme proteins. in *Adv. Inorg. Chem.*, Mauk, A. & Sykes, A., eds., vol. 51, pp. 409–455. Academic Press, New York.

Gibney, B., Huang, S., Skalicky, J., Fuentes, E., Wand, A. & Dutton, P. (2001). Hydrophobic modulation of heme properties in heme protein maquettes. *Biochemistry*, **40**, 10550–10561.

Gibney, B., Johansson, J., Rabanal, F., Skalicky, J., Wand, A. & Dutton, P. (1997). Global topology and stability and local structure and dynamics in a synthetic spin-labeled four-helix bundle protein. *Biochemistry*, **36**, 2798–2806.

Gibney, B., Mulholland, S., Rabanal, F. & Dutton, P. (1996). Ferredoxin and ferredoxin-heme maquettes. *Proc. Natl. Acad. Sci. USA.*, **93**, 15041–15046.

Gibney, B., Rabanal, F., Reddy, K. & Dutton, P. (1998). Effect of four helix bundle topology on heme binding and redox properties. *Biochemistry*, **37**, 4635–4643.

Gibney, B., Rabanal, F., Skalicky, J., Wand, A. & Dutton, P. (1999). Iterative protein redesign. *J. Am. Chem. Soc.*, **121**, 4952–4960.

Gobets, B. & van Grondelle, R. (2001). Energy transfer and trapping in photosystem I. *Biochim. Biophys. Acta,* , **1507**, 80–99.

Gunner, M., Nicholls, A. & Honig, B. (1996). Electrostatic potentials in *Rhodopseudomonas viridis* reaction centers: Implications for the driving force and directionality of electron transfer. *J. Phys. Chem.*, **100**, 4277–4291.

Gunner, M., Robertson, D. & Dutton, P. (1986). Kinetic studies on the reaction center protein from *Rhodospeudomonas sphaeroides*: The temperature and free energy de-

pendence of electron transfer between various quinones in the Qa site and oxidised bacteriochlorophyll dimer. *J. Phys. Chem.*, **90**, 3783–3795.

Guo, Q., Corbett, J., Yue, G., Fann, Y., Qian, S., Tomer, K. & Mason, R. (2002). Electron spin resonance investigation of semiquinone radicals formed from the reaction of ubiquinone 0 with human oxyhemoglobin. *J. Biol. Chem.*, **277**, 6104–6110.

Gust, D., Moore, T. & Moore, A. (1993). Molecular mimicry of photosynthetic energy and electron transfer. *Acc. Chem. Res.*, **26**, 198–205.

Gust, D., Moore, T. & Moore, A. (2001). Mimicking photosynthetic solar energy transduction. *Acc. Chem. Res.*, **34**, 40–48.

Hamada, K., Bethge, P. & Mathews, F. (1995). Refined structure of cytochrome *b*562 from *Escherichia coli* at 1.4 Å resolution. *J. Mol. Biol.*, **247**, 947–962.

Harbury, H. & Loach, P. (1960). Oxidation-linked proton functions in heme octa- and undecapeptides from mammalian cytochrome *c*. *J. Biol. Chem.*, **235**, 3640–3645.

Hastings, S., Kaysser, T., Jiang, F., Salerno, J., Gennis, R. & Ingledew, W. (1998). Identification of a stable semiquinone intermediate in the purified and membrane bound ubiquinol oxidase-cytochrome bd from *Escherichia coli*. *Eur. J. Biochem.*, **255**, 317–323.

Heathcote, P., Jones, M. & Fyfe, P. (2003). Type I photosynthetic reaction centres: Structure and function. *Philos. Trans. R. Soc. Lond. B Biol. Sci.*, **358**, 231–243.

Hecht, M., Das, A., Go, A., Bradley, L. & Wei, Y. (2004). *De novo* proteins from designed combinatorial libraries. *Prot. Sci.*, **13**, 1711–1723.

Hill, R., Raleigh, D., Lombardi, A. & , W. (2000). *De novo* design of helical bundles as models for understanding protein folding and function. *Acc. Che. Res.*, **33**, 745–754.

Ho, P., Sutoris, C., Liang, N., Margoliash, E. & Hoffman, B. (1985). Species specificity of long-range electron transfer within the complex between zinc-substituted cytochrome *c* peroxidase and cytochrome *c*. *J. Am. Chem. Soc.*, **107**, 1070–1071.

Ho, T.-F., McIntosh, A. & Bolton, J. (1980). Intramolecular photochemical electron transfer in a linked porphyrin-quinone molecule as a model for the primary step of photosynthesis. *Nature.*, **286**, 254–256.

Hoess, R. (2001). Protein design and phage display. *Chem. Rev.*, **101**, 3205–3218.

Hoffman, B. (1975). Triplet state electron paramagnetic resonance studies of zinc porphyrins and zinc-substituted hemoglobins and myoglobins. *J. Am. Chem. Soc.*, **97**, 1688–1694.

Hopfield, J. (1974). Electron transfer between biological molecules by thermally activated ttunneling. *Proc. Natl. Acad. Sci. USA.*, **71**, 3640–3644.

Huang, S., Gibney, B., Stayrook, S., Dutton, P. & Lewis, M. (2003). X-ray structure of a maquette scaffold. *J. Mol. Biol.*, **326**, 1219–1225.

Huffman, D. L. & Suslick, K. S. (2000). Hydrophobic interactions in metalloporphyrin-peptide complexes. *Inorg. Chem.*, **39**, 5418–5419.

Huppman, P., Arlt, T., Penzkofer, H., Schmidt, S., Bibikova, M., Dohse, B., Oesterhelt, D., Wachtveit, J. & Zinth, W. (2002). Kinetics, energetics, and electronic coupling of the primary electron transfer reactions in mutated reaction centers of *Blastochloris viridis*. *Biophys. J.*, **82**, 3186–3197.

Ishida, Y., Konishi, K., Aida, T. & Nagamune, T. (1998). Apocytochrome *b*562 as a novel chiral host molecule: The first enantioselective reconstitution. *Chem. Eur. J.*, **4**, 1148–1152.

Itagaki, E. & Hagar, L. (1966). Studies on cytochrome *b*-562 of *Escherichia coli*. i. purification and crystallization of cytochrome *b*-562. *J. Biol. Chem.*, **241**, 3687–3695.

Ivancich, A., Artz, K., Williams, J., Allen, J. & Mattioli, T. (1998). Effects of hydrogen bonds on the redox potential and electronic structure of the bacterial primary electron donor. *Biochemistry*, **37**, 11812–11820.

Iverson, T., Luna-Chavez, C., Cecchini, G. & Rees, D. (1999). Structure of the *Escherichia coli* fumarate reductase respiratory complex. *Science.*, **284**, 1961–1966.

Jameson, D. & Seifried, S. (1999). Quantification of protein-protein interactions using fluorescence polarization. *Methods,* , **19**, 222–233.

John, D. & Weeks, K. (2000). van't hoff enthalpies without baselines. *Protein Sci.*, **9**, 1416–1419.

Johnson, E. & Parson, W. (2002). Electrostatic interactions in an integral membrane protein. *Biochemistry* , **41**, 6483–6494.

Jordan, P., Fromme, P., Witt, H.-T., Klukas, O., Saenger, W. & Krauß, N. (2001). Three-dimensional structure of cyanobacterial photosystem I at 2.5 Å resolution. *Nature.*, **411**, 909–917.

Kalman, L., LoButto, R., Allen, J. & Williams, J. (1999). Modified reaction centres oxidize tyrosine in reactions that mirror photosystem II. *Nature.*, **402**, 696–699.

Kalman, L., LoRBrutton, R., Allen, J. & Williams, J. (2003). Manganese oxidation by modified reaction centers from *Rhodobacter sphaeroides*. *Biochemistry*, **42**, 11016–11022.

Kamiya, N., Okimoto, Y., Ding, Z., Ohtomo, H., Shimizu, M., Kitayama, A., Morii, H. & Nagamune, T. (2001). How does axial ligand deletion affect the structure and the function of cytochrome *b*562? *Prot. Eng.*, **14**, 415–419.

Kamiya, N. & Shen, J. (2003). Crystal structure of oxygen-evolving photosystem II from *Thermosynechococcus vulcanus* at 3.7-Å resolution. *Proc. Natl. Acad. Sci. USA.*, **100**, 98–103.

Kamtekar, S., Schiffer, J., Xiong, H., Babik, J. & Hecht, M. (1993). Protein design by binary patterning of polar and nonpolar amino acids. *Science.*, **262** (5140), 1680–1685.

Kaneko, Y., Tamura, M. & Yamakazi, I. (1980). Formation of porphyrin π cation radical in zinc-substituted horseradish peroxidase. *Biochemistry*, **19**, 5795–5799.

Kaplan, J. & DeGrado, W. (2004). *De novo* design of catalytic proteins. *Proc. Natl. Acad. Sci. USA.*, **101**, 11566–11570.

Kashiwada, A., Nishino, N., Wanf, Z.-Y., Nozawa, T., Kobayashi, M. & Nango, M. (1999). Molecular assembly of bacteriochlorophyll *a* and its analogues by synthetic 4α-helix peptides. *Chem. Lett.*, **28**, 1301–1302.

Kehoe, J., Meadows, K., Parkes-Loach, P. & Loach, P. (1998). Reconstitution of core light-harvesting complexes of photosynthetic bacteria using chemically synthesized polypeptides. 2. Determination of structural features that stabilize complex formation and their implications for the structure of the subunit complex. *Biochemistry* , **37**, 3418–3428.

Kennedy, M., Silchenko, S., Houndonougbo, N., Gibney, B., Dutton, P., Rodgers, K. & Benson, D. (2001). Model hemoprotein reduction potentials: The effects of histidine-to-iron coordination equilibrium. *J. Am. Chem. Soc.*, **123**, 4635–4636.

Krabben, L., Schlodder, E., Jordan, R., Carbonera, D., Giacometti, G., Lee, H., Webber, A. & Lubitz, W. (2000). Influence of the axial ligands on the spectral properties of P700 of photosystem I: A study of site-directed mutants. *Biochemistry*, **39**, 13012–13025.

Kuhlman, B., Dantas, G., Ireton, G., Varani, G., Stoddard, B. & Baker, D. (2003). Design of a novel globular protein fold with atomic-level accuracy. *Science.*, **302**, 1364–1368.

Kurreck, H. & Huber, M. (1995). Model reactions for photosynthesis-photoinduced charge and energy transfer between covalently linked porphyrin and quinone units. *Angew. Chem., Int. Ed. Engl.*, **34**, 849–866.

Ladokhin, A. (2000). Fluorescence spectroscopy in peptide and protein analysis. *in Encyclopedia of analytical chemistry,* , , 5762–5779.

Larsson, S. (1998). Electron transfer in proteins. *Biochim. Biophys. Acta,* , **1365**, 294–300.

Lear, J., Gratkowski, H. & DeGrado, W. (2001). *De novo* design, synthesis and characterization of membrane-active peptides. *Biochem. Soc. Trans.*, **29**, 559–564.

Leitch, F., Brown, K. & Pettigrew, G. (1985). Complexity in the redox titration of the dihaem cytochrome *c*4. *Biochim. Biophys. Acta,* , **808**, 213–218.

Lemma, E., Unden, G. & Kroger, A. (1990). Menaquinone is an obligatory component of the chain catalyzing succinate respiration in *Bacillus subtilis*. *Arch. Microbiol.*, **155**, 62–67.

Lin, X., Murchison, H., Nagarajan, V., Parson, W. & Allen, J.P. Williams, J. (1994). Specific alteration of the oxidation potential of the electron donor in reaction centers from *Rhodobacter sphaeroides*. *Proc. Natl. Acad. Sci. USA.*, **91**, 10265–10269.

Lombardi, A., Nastri, F. & Pavone, V. (2001). Peptide-based heme-protein models. *Chem. Rev.*, **101**, 3165–3189.

Low, D., Hill, M., Carrasco, M., Kent, S. & Botti, P. (2001). Total synthesis of cytochrome *b*562 by native chemical ligation using a removable auxiliary. *Proc. Natl. Acad. Sci. USA.*, **98**, 6554–6559.

Magner, E. & McLendon, G. (1989). Ground-state and excited-state electron-transfer reactions of zinc cytochrome *c*. *J. Phys. Chem.*, **93**, 7130–7134.

Marcus, R. (1956). On the theory of oxidation-reduction reactions involving electron transfer: I. *J. Chem. Phys.*, **24**, 966–978.

Marcus, R. & Sutin, N. (1985). Electron transfers in chemistry and biology. *Biochim. Biophys. Acta,* , **811**, 265–322.

Margalit, R., Shaklai, N. & Cohen, S. (1983). Fluorimetric studies on the dimerization equilibrium of protoporphyrin ix and its haemato derivative. *Biochem. J.*, **209**, 547–552.

Mattioli, T., Lin, X., Allen, J. & Williams, J. (1995). Correlation between multiple hydrogen bonding and alteration of the oxidation potential of the bacteriochlorophyll

dimer of reaction centers from *Rhodobacter sphaeroides*. *Biochemistry*, **34**, 6142–6152.

Mayo, S., Ellis Jr., W., Crutchley, R. & Gray, H. (1986). Long-range electron transfer in heme proteins. *Science.*, **233**, 948–952.

McConnell, H. (1961). Intramolecular charge transfer in aromatic free radicals. *J. Phys. Chem.*, **35**, 508–515.

McGourty, J., Blough, N. & Hoffman, B. (1983). Electron transfer at crystallographically known long distances (25 Å) in [Zn^{II}, Fe^{III}] hybrid hemoglobin. *J. Am. Chem. Soc.*, **105**, 4470–4472.

McGourty, J., Peterson-Kennedy, S, E., Ruo, W. & Hoffman, B. (1987). Characterization of long-range electron transfer in mixed-metal [zinc,iron] hybrid hemoglobins. *Biochemistry*, **26**, 8302–8312.

McLendon, G., Winkler, J., Nocera, D., Mauk, M., Mauk, A. & Gray, H. (1985). Quenching of zinc-substituted cytochrome *c* excited states by cytochrome *b*5. *J. Am. Chem. Soc.*, **107**, 739–740.

Meade, T., Gray, H. & Winkler, J. (1989). Driving-force effects on the rate of long-range electron transfer in ruthenium-modified cytochrome *c*. *J. Am. Chem. Soc.*, **111**, 4353–4356.

Meyer, T. & Kamen, M. (1982). New perspectives on *c*-type cytochromes. *Adv. Protein Chem.*, **35**, 105–212.

Miller, A.-F. & Brudvig, G. (1991). A guide to electron paramagnetic resonance spectroscopy of photosystem II membranes. *Biochim. Biophys. Acta,* , **1056**, 1–18.

Miller, G., Zhang, B., Hardman, J. & Timkovich, R. (2000). Converting a *c*-type to a *b*-type cytochrome: Met61 to His61 mutant of *Pseudomonas* cytochrome *c*551. *Biochemistry*, **39**, 9010–9017.

Miller, J., Di Bilio, A., Wehbi, W., Green, M., Museth, A., Richards, J., Winkler, J. & HB., G. (2004). Electron tunneling in rhenium-modified *Pseudomonas aeruginosa* azurins. *Biochim. Biophys. Acta,* , **1665**, 59–63.

Mines, G., Pascher, T., Lee, S., Winkler, J. & Gray, H. (1996). Cytochrome *c* folding triggered by electron transfer. *Chem. Biol.*, **3**, 491–497.

Moore, G. & Pettigrew, G., eds (1990). *Cytochromes c. Evolutionary, structural, and physicochemical aspects*. Springer-Verlag, Berlin.

Moore, G., Williams, R., Peterson, J., Thomson, A. & Mathews, F. (1985). A spectroscopic investigationof the structure and redox properties of *Escherichia coli* cytochrome *b*-562. *Biochim. Biophys. Acta,* **829**, 83–96.

Moore, J. & Arnold, F. (1996). Directed evolution of a para-nitrobenzyl esterase for aqueous-organic solvents. *Nature. Biotech.* **14**, 458–467.

Moser, C. & Dutton, P. (1992). Engineering protein structure for electron transfer function in photosynthetic reaction centers. *Biochim. Biophys. Acta,* **1101**, 171–176.

Moser, C., Page, C., Cogdell, R., Barber, J., Wraight, C. & Dutton, P.L. (2003). Length, time, and energy scales of photosystems. *Adv. Protein Chem.* **63**, 71–109.

Moser, C., Page, C., Farid, R. & Dutton, P. (1995). Biological electron transfer. *J. Bioenerg. Biomembr.* **27**, 263–274.

Moser, C. C. & Dutton, P. L. (1996). *Protein Electron Transfer* chapter 1, pp. 1–21. BIOS Scientific Publisher Ltd, Oxford.

Nappa, M. & Valentine, J. (1978). The influence of axial ligands on metalloporphyrin visible absorption spectra. complexes of tetraphenylporphinatozinc. *J. Am. Chem. Soc.*, **100**, 5075–5080.

Nesset, M., Shokhirev, N., Enemark, P., Jacobson, S. & Walker, F. (1996). Models of the cytochromes. Redox properties and thermodynamic stabilities of complexes

of hindered iron(III) and iron(II) tetraphenylporphyrinates with substituted pyridines and imidazoles. *Inorg. Chem.*, **35**, 5188–5200.

Nocera, D., Winkler, J., Yocom, K., Bordignon, E. & Gray, H. (1984). Kinetics of intermolecular and intramolecular electron transfer from ruthenium(II) complexes to ferricytochrome *c*. *J. Am. Chem. Soc.*, **106**, 5145–5150.

Okamura, M., Paddick, M., Graige, M. & Feher, G. (2000). Proton and electron transfer in bacterial reaction centers. *Biochim. Biophys. Acta,* , **1458**, 148–163.

Onuchic, J. N., Beratan, D. N., Winkler, J. R. & Gray, H. B. (1992). Electron-tunneling pathways in proteins. *Science.*, **258**, 1740–1741.

Ort, D. & Yocum, C. eds. (1996). *Oxygenic photosynthesis: The light reactions*. Kluwer Academic Publishers, Dordrecht.

Othman, S. & Desbois, A. (1998). Resonance raman investigation of lysine and n-acetylmethionine complexes of ferric and ferrous microperoxidase. *Eur. Biophys. J,* **28**, 12–25.

Othman, S., Le Lirzin, A. & Desbois, A. (1994). Resonance raman investigation of imidazole and imidazolate complexes of microperoxidase: Characterization of the bis(histidine) axial ligation in *c*-type cytochromes. *Biochemistry* **33**, 15437–15448.

Pace, C. (1986). Determination and analysis of urea and guanidine hydrochloride denaturation curves. *Methods Enzymol.* **131**, 266–280.

Page, C., Moser, C., Chen, X. & Dutton, P. (1999). Natural engineering principles of electron tunnelling in biological oxidation-reduction. *Nature.* **402**, 47–52.

Parson, W. (1996). in *Protein Electron Transfer,* Bendall, D. S. ed., chapter 6, pp. 125–160. BIOS Scientific Publisher Ltd, Oxford.

Patai, S. & Rappoport, Z. (1988). *The chemistry of the quinonoid compounds*, vol. 2,. John Wiley and Sons.

Peisach, J., Blumberg, W. & Adler, A. (1973). Electron paramagnetic resonance studies of iron porphyrin and chlorin systems. *Ann. NY Acad. Sci.*, **206**, 310–327.

Peterson-Kennedy, S., McGourty, J. & Hoffman, B. (1984). Temperature dependence of long-range electron transfer in [Zn,feiii] hybrid hemoglobin. *J. Am. Chem. Soc.*, **106**, 5010–5012.

Prince, R., Dutton, P. & Bruce, J. (1983). Electrochemistry of ubiquinones: Menaquinones and plastoquinones in aprotic solvents. *FEBS Lett.*, **160**, 273–276.

Privett, H., Reedy, C., Kennedy, M. & Gibney, B. (2002). Nonnatural amino acid ligands in heme protein design. *J. Am. Chem. Soc.*, **124**, 6828–6829.

Qin, L. & Kostic, N. (1994). Photoinduced electron transfer from the triplet state of zinc cytochrome *c* to ferricytochrome *b*5 is gated by configurational fluctuations of the diprotein complex. *Biochemistry*, **22**, 12592–12599.

Rabanal, F., DeGrado, W. & Dutton, P. (1996). Toward the synthesis of a photosynthetic reaction center maquette: A cofacial porphyrin pair assembled between two subunits of a synthetic four-helix bundle. *J. Am. Chem. Soc.*, **118**, 473–474.

Rappaport, F., Guergova-Kuras, M., Nixon, P., Diner, B. & Lavergne, J. (2002). Kinetics and pathways of charge recombination in photosystem II. *Biochemistry*, **41**, 8518–8527.

Rau, H., DeJonge, N. & Haehnel, W. (1999). Modular synthesis of *de novo*-designed metalloproteins for light-induced electron transfer. *Proc. Natl. Acad. Sci. USA.*, **1998**, 11526–11531.

Rau, H., Snigula, H., Struck, A., Robert, B., Scheer, H. & Haehnel, W. (2001). Design, synthesis and properties of synthetic chlorophyll proteins. *Eur. J. Biochem.*, **268**, 3284–3295.

Razeghifard, M. & Wydrzynski, T. (2003). Binding of Zn-chlorin to a synthetic four-helix bundle peptide through histidine ligation. *Biochemistry*, **42**, 1024–1034.

Reddy, K., Angiolillo, P., Wright, W., Laberge, M. & Vanderkooi, J. (1996). Spectral splitting of the α ($q_{0,0}$) absorption band of ferrous cytochrome *c* and other heme proteins. *Biochemistry*, **35**, 12820–12830.

Redfearn, E. (1965). *Biochemisty of Quinones*, chapter 5, pp. 149–181. Academic Press, New York.

Reedy, C., Kennedy, M. & Gibney, B. (2003). Thermodynamic characterization of ferric and ferrous haem binding to a designed four-alpha-helix protein. *Chem. Comm.*, **7**, 570–571.

Rehm, D. & Weller, A. (1970). Kinetics of fluorescence quenching by electron and H-atom transfer. *Isr. J. Chem.*, **8**, 259–291.

Rich, P. (2005). The quinone chemistry of *bc* complexes. *Biochim. Biophys. Acta, in press.*

Rinyu, L., Martin, E., Takahashi, E., Maroti, P. & Wraight, C. (2004). Modulation of the free energy of the primary quinone acceptor (Qa) in reaction centers from *Rhodobacter sphaeroides*: Contributions from the protein and protein-lipid(cardiolipin) interactions. *Biochim. Biophys. Acta,* , **1655**, 93–101.

Robertson, D., Farid, R., Moser, C., Urbauer, J., Mulholland, S., Pidikiti, R., Lear, J., Wand, A., DeGrado, W. & Dutton, P. (1994). Design and synthesis of multi-haem proteins. *Nature.*, **368**, 425–432.

Robertson, D., Prince, R., Bowyer, J., Matsuura, K., Dutton, P. & Ohnishi, T. (1984). Thermodynamic properties of the semiquinone and its binding site in the ubiquinol-cytochrome *c* (c2) oxidoreductase of respiratory and photosynthetic systems. *J. Biol. Chem.*, **259**, 1758–1763.

Robinson, C., Liu, Y., O'Brien, R., Sligar, S. & Sturtevant, J. (1998). A differential scanning calorimetric study of the thermal unfolding of apo- and holo-cytochrome *b*562. *Protein Sci.*, **7**, 961–965.

Robinson, C., Liu, Y., Thomson, A., Sturtevant, J. & Sligar, S. (1997). Energetics of heme binding to native and denatured cytochrome *b*562. *Biochemistry*, **36**, 16141–16146.

Rojas, N., Kamtekar, S., Simons, C., McLean, J., Vogel, K., Spiro, T., Farid, R. & Hecht, M. (1997). *De novo* heme proteins from designed combinatorial libraries. *Protein Sci.*, **6**, 2512–2524.

Romberg, R. & Kassner, R. (1982). Effects of solvent on the absorption maxima of five-coordinate heme complexes and carbon monoxide-heme complexes as models for the differential spectral properties of hemoglobins and myoglobins. *Biochemistry*, **21**, 880–886.

Rotsaert, F., Hallberg, B., de Vries, S., Moenne-Loccoz, P., Divne, C., Renganathan, V. & Gold, M. (2003). Biophysical and structural analysis of a novel heme *b* iron ligation in the flavocytochrome cellobiose dehydrogenase. *J. Biol. Chem.*, **278**, 33224–33231.

Rupp, H., Rao, K. K., Hall, D. O. & Cammack, R. (1978). Electron spin relaxation of iron-sulphur proteins studied by microwave power saturation. *Biochim. Biophys. Acta,* , **537**, 255–269.

Saven, J. (2002). Combinatorial protein design. *Curr. Opin. Struct. Biol.*, **12**, 453–458.

Scheer, H., ed. (1991). *Chlorophylls*. CRC Press, Boca Raton, FL.

Sharp, K. (1998). Calculation of electron transfer reorganization energies using the finite difference poisson-boltzmann model. *Biophys. J.* **74**, 1241–1250.

Sharp, R., Diers, J., Bocain, D. & Dutton, P. (1998*a*). Differential binding of iron(III) and zinc(II) protoporhyrin(ix) to synthetic four-helix bundles. *J. Am. Chem. Soc.* **120**, 7103–7104.

Sharp, R., Moser, C., Rabanal, R. & Dutton, P. (1998*b*). Design, synthesis and characterization of a photoactivatable flavocytochrome molecular maquette. *Proc. Natl. Acad. Sci. USA.* **95**, 10465–10470.

Shifman, J., Gibney, B., Sharp, R. & Dutton, P. (2000). Heme redox potential control in *de novo* designed four-alpha-helix bundle proteins. *Biochemistry* **39**, 14813–14821.

Shifman, J., Moser, C., Kalsbeck, W., Bocian, D. & Dutton, P. (1998). Functionalized *de novo* designed proteins: Mechanism of proton coupling to oxidation/reduction in heme protein maquettes. *Biochemistry* **37**, 16815–16827.

Simolo, K., McLendon, G., Mauk, M. & Mauk, A. G. (1984). Photoinduced electron transfer within a protein-protein complex formed between physiological redox partners: Reduction of ferricytochrome *b*5 by the hemoglobin derivative $\alpha_2^{Zn}\beta_2^{Fe^{III}CN}$. *J. Am. Chem. Soc.* **106**, 5012–5013.

Sisido, M., Hoshino, S., Kusano, H., Kuragaki, M., Makino, M., Sasaki, H., Smith, T. & Ghiggino, K. P. (2001). Distance dependence of photoinduced electron transfer along α-helical polypeptides. *J. Phys. Chem. B,* **105**, 10407–10415.

Snell, J. & Weissberger, A. (1939). The reaction of thiol compounds with quinones. *J. Am. Chem. Soc.* **61**, 450–453.

Springs, S., Bass, S., Bowman, G., Nodelman, I., Schutt, C. & McLendon, G. (2002). A multigeneration analysis of cytochrome *b*562 redox variants: Evolutionary strategies for modulating redox potential revealed using a library approach. *Biochemistry* **41**, 4321–4328.

Springs, S., Bass, S. & McLendon, G. (2000). Cytochrome *b*562 variants: A library for examining redox potential evolution. *Biochemistry* **39**, 6075–6082.

Steinberg-Yfrach, G., Rigaud, J.-L., Durantini, E., Moore, A., Gust, D. & Moore, T. (1998). Light-driven production of ATP catalysed by F0F1-ATP synthase in an arificial photosynthetic membrane. *Nature.* **392**, 479–482.

Sudha, B., Dixit, N., Moy, V. & Vanderkooi, J. (1984). Reactions of excited-state cytochrome *c* derivatives: Delayed fluorescence and phosphorescence of zinc, tin, and metal-free cytochrome *c* at room temperature. *Biochemistry* **23**, 2103–2107.

Sutin, N. (1982). Nuclear, electronic and frequency factors in electron-transfer reactions. *Acc. Chem. Res.* **15**, 275–282.

Takahashi, E., Wells, T. & Wraight, C. (2001). Protein control of the redox potential of the primary quinone acceptor in reaction centers from *Rhodobacter sphaeroides*. *Biochemistry* **40**, 1020–1028.

Taylor, C. (1977). The EPR of low spin heme complexes. *Biochim. Biophys. Acta,* **491**, 137–149.

Tchaikovskaya, O. N., Sokolova, I., KuZnetsova, R., Swetlitchnyi, V., Kopylova, T. & Mayer, G. (2000). Fluorescence investigations of phenol phototransformation in aqueous solutions. *J. Fluoresc.* **10**, 403–408.

Teale, F. (1959). Cleavage of haem-protein link by acid methylethylketone. *Biochim. Biophys. Acta,* **35**, 543.

Todd, J., Parkes-Loach, P., Leykam, J. & Loach, P. (1998). In vitro reconstitution of the core and peripheral light-harvesting complexes of *rhodospirillum molischianum* from separately isolated components. *Biochemistry* **37**, 17458–17468.

Twitchett, M., Ferrer, J., Siddarth, P. & Mauk, A. (1997). Intramolecular electron transfer kinetics in a synthetic flavocytochrome *c*. *J. Am. Chem. Soc.* **119**, 435–436.

Ueda, T., Masumoto, K., Ishibashi, R., So, T. & Imoto, T. (2000). Remarkable thermal stability of doubly intramolecularly cross-linked hen lysozyme. *Protein Eng.* **13**, 193–196.

Uno, T., Yukinari, A., Moriyama, Y., Ishikawa, Y., Tomisugi, Y., Brannigan, J. & Wilkinson, A. (2001). Engineering a ligand binding pocket into a four-helix bundle protein cytochrome *b*562. *J. Am. Chem. Soc.* **123**, 512–513.

Upadhyay, A., Petasis, D., Arciero, D., Hooper, A. & M.P., H. (2003). Spectroscopic characterization and assignment of reduction potentials in the tetraheme cytochrome *c*554 from *Nitrosomonas europaea*. *J. Am. Chem. Soc.* **125**, 1738–1747.

Walker, F., Huynh, B., Scheidt, W. & Osvath, S. (1986). Models for cytochromes *b*. effect of axial ligand plane orientation on the EPR and mössbauer spectra of low-spin ferrihemes. *J. Am. Chem. Soc.* **108**, 5288–5297.

Warncke, K. & Dutton, P. (1993). Influence of Qa site redox cofactor structure on the equilibrium binding, in situ electrochemistry, and electron-transfer performance in the photosynthetic reaction center protein. *Biochemistry* **32**, 4769–4779.

Warncke, K., Gunner, M., Braun, B., Gu, L., Yu, C.-A., Bruce, J. & Dutton, P. (1994). Influence of hydrocarbon tail structure on quinone binding and electron-transfer performance at the Qa and Qb sites of the photosynthetic reaction center protein. *Biochemistry* **33**, 7830–7841.

Wasielewski, M. (1992). Photoinduced electron transfer in supramolecular systems for artificial photosynthesis. *Chem. Rev.* **92**, 435–461.

Watanabe, T. & Kobayashi, M. (1991). in *Chlorophylls,* Scheer, H. ed., chapter 1.11, pp. 288–315. CRC Press, Boca Raton, FL.

Willis, K., Szabo, A., Zuker, M., Ridgeway, J. & Alpert, B. (1990). Fluorescence decay kinetics of the tryptophyl residues of myoglobin: Effect of heme ligation and evidence for discrete lifetime component. *Biochemistry*, **29**, 5270–5275.

Winkler, J., Di Bilio, A., Farrow, N., Richards, J. & Gray, H. (1999). Electron tunneling in biological molecules. *Pure Appl. Chem.*, **71**, 1753–1764.

Winkler, J. & Gray, H. (1992). Electron transfer in rhuthenium-modified proteins. *Chem. Rev.*, **92**, 369–379.

Winkler, J., Nocera, D., Yocom, K., Bordignon, E. & Gray, H. (1982). Electron-transfer kinetics of pentaammineruthenium(iii)(histidine-33)-ferricytochrome *c*. measurement of the rate of intramolecular electron transfer between redox centers separated by 15 Å in a protein. *J. Am. Chem. Soc.*, **104**, 5798–5800.

Wittung-Stafshede, P., Gray, H. & Winkler, J. (1997). Rapid formation of a four-helix-bundle. cytochrome *b*562 folding triggered by electron transfer. *J. Am. Chem. Soc.*, **119**, 9562–9563.

Wraight, C. (1998). in *Photosynthesis: Mechanisms and effects,* Garab, G. ed., vol. 2, pp. 693–689. Kluwer Academic Publishers, Dordrecht, The Netherlands.

Wright, K. & Boxer, S. (1981). Solution properties of synthetic chlorophyllide-and bacteriochlorophyllide-apomyoglobin complexes. *Biochemistry*, **20**, 7546–7556.

Yocom, K., Shelton, J., Shelton, J., Schroeder, W., Worosila, G., Isied, S., Bordignon, E. & Gray, H. (1982). Preparation and characterization of a pentaammineruthenium(III) derivative of horse heart ferricytochrome *c*. *Proc. Natl. Acad. Sci. USA.*, **79**, 7052–7055.

Zemel, H. & Hoffman, M. (1981). Long-range triplet-triplet energy transfer within metal-substituted hemoglobins. *J. Am. Chem. Soc.*, **103**, 1192–1201.

Zhou, N., Kay, C. & Hodges, R. (1992). Synthetic model proteins. positional effects of interchain hydrophobic interactions on stability of two-stranded alpha-helical coiled-coils. *J. Biol. Chem.*, **267**, 2664–2670.

Zouni, A., Witt, H.-T., Kern, J., Fromme, P., Krauß, N., Saenger, W. & Orth, P. (2001). Crystal structure of photosystem II from *Synechococcus elongatus* at 3.8 Å resolution. *Nature.*, **409**, 739–743.